Probing the Nucleus with d+Au Collisions at RHIC

A Dissertation Presented

by

Zvi Hirsh Citron

to

The Graduate School

in Partial Fulfillment of the

Requirements

for the Degree of

Doctor of Philosophy

in

Physics

Stony Brook University

May 2011

Stony Brook University

The Graduate School

Zvi Hirsh Citron

We, the dissertation committee for the above candidate for the **Doctor of Philosophy** degree, hereby recommend acceptance of this dissertation.

Professor Thomas K Hemmick, Thesis Advisor
Department of Physics and Astronomy

Professor Dmitri Kharzeev, Chairman of the defense committee
Department of Physics and Astronomy

Professor Alan Calder
Department of Physics and Astronomy

Professor Jiangyong Jia, Outside member
Department of Chemistry

This dissertation is accepted by the Graduate School.

Lawrence Martin
Dean of the Graduate School

Abstract of the Dissertation

Probing the Nucleus with d+Au Collisions at RHIC

by

Zvi Hirsh Citron

Doctor of Philosophy

in

Physics

Stony Brook University

2011

The Relativistic Heavy Ion Collider (RHIC) was built to produce and study Quark Gluon Plasma (QGP), the phase of matter thought to exist under conditions sufficiently hot and dense to create a medium in which the degrees of freedom are quarks and gluons rather than color neutral hadrons. Already in its early years of running, the data from RHIC provided tantalizing evidence of QGP signatures in Au+Au collisions at $\sqrt{s_{NN}} = 200$ GeV. A crucial part of understanding the putative QGP in Au+Au collisions is to have both a well understood reference as well as a robust control experiment. Proton-proton collisions at the same $\sqrt{s_{NN}}$ serve as the baseline for heavy ion collisions at RHIC, and play an invaluable role in setting our frame of reference in interactions that do *not* create any nuclear medium. For the control experiment, RHIC's ability to collide asymmetric beams is utilized and d+Au collisions are used. Unlike p+p collisions, in the d+Au system there is a nuclear medium present - the heavy Au nucleus - and so we may study this system to distinguish initial state cold

nuclear matter effects from final state effects that occur in the hot dense medium of Au+Au collisions.

Beyond its use as a control experiment, the d+Au collision system presents the opportunity for important study of nuclear and nucleonic structure, it is after all necessary for our colored parton theory to operate in the nucleus as well as in a QGP. Deuteron - gold collisions at RHIC are a powerful tool for shedding light on cold nuclear matter effects.

This thesis describes two analyses of d+Au collisions measured by the PHENIX experiment at RHIC. The first is a measurement of the midrapidity yield of unidentified charged hadrons in the 2003 RHIC run. This is used a key baseline for understanding particle production in Au+Au collisions as well as a detailed look at the Cronin effect. The second analysis measures rapidity separated two-particle production where one of the particles is at either forward or backward rapidity and the other at midrapidity. These measurements probe different x regions of the Au nucleus and there investigate shadowing, anti-shadowing and other cold nuclear matter effects.

Contents

List of Figures

List of Tables

Acknowledgements

I would like to thank my advisor, Tom Hemmick. Tom introduced me to the field when I was an undergraduate summer intern, and was the catalyst for my coming to Stony Brook and joining PHENIX as a graduate student. Over the years he has continued to help, teach, and encourage me.

I would also like to acknowledge all the members of the Relativistic Heavy Ion Group at Stony Brook with whom I've had the privilege of working and learning from these last several years. In particular, I thank Vlad Pantuev, who worked closely with me when I was first getting acquainted with PHENIX and heavy ion physics. I've also been fortunate to work with many other PHENIX collaborators, amongst them Beau Meredith who helped me with analyzing MPC data.

Beginning with the first college physics class I took and continuing through this thesis work, Jason Kamin has been a true friend to me as well as providing me with invaluable problem solving help. I extend my heartfelt gratitude to him for helping me navigate these waters.

Lastly, I thank my family who have been with me through it all.

Part I

Introduction

Chapter 1

Physics Introduction and Motivation

One of the major goals in the study of the physical sciences is and has been an understanding of matter in its most fundamental forms. The history of science traces our discovery of the concentrically microscopic nature we inhabit. We live in and of molecules, that are made of atoms, that are made of nuclei (surrounded by electrons), that are made of protons and neutrons, that are made of quarks and gluons; this, in an ocean of a vacuum suffused with energy often willing to recast itself as more particles. Our best understanding is that the quarks and gluons are truly fundamental particles - they have no constituent parts - they form the innermost ring of the physical comedy.

In the modern era of collider physics we are able to generate the energy scales needed for the study of these most fundamental particles and the strong force that dictates their interactions. In many cases it is informative to observe this matter under extreme conditions. What happens to the gluon distribution in an ultra-relativistic nucleus? Is it possible to reach the effects of asymptotic freedom and achieve deconfinement in a hot dense matter of quarks and gluons?

The chief aim of the Relativistic Heavy Ion Collider (RHIC) is to produce and study Quark Gluon Plasma (QGP) the phase of matter thought to exist under conditions sufficiently hot and dense to create a medium in which the degrees of freedom are quarks and gluons rather than color neutral hadrons [1]. Already in its early years of running the data from RHIC provided tantalizing evidence of QGP signatures in Au+Au collisions at $\sqrt{s_{NN}} = 200$ GeV [2, 3, 4, 5]. A crucial part of understanding the putative QGP in Au+Au collisions is to have both a well understood reference as well as a robust control experiment. Proton-proton collisions at the same $\sqrt{s_{NN}}$ serve as the baseline for heavy ion collisions at RHIC, and play an invaluable role in setting our frame of reference in interactions that do *not* create any nuclear medium. For the control experiment, RHIC's ability to collide asymmetric beams is utilized and d+Au collisions are used. Unlike p+p collisions, in the d+Au system there is a nuclear medium present - the heavy Au nucleus - and so we may study this system to distinguish initial state cold nuclear matter effects from final state effects that occur in the hot dense medium of Au+Au collisions.

Beyond its use as a control experiment, the d+Au collision system presents the opportunity for important study of nuclear and nucleonic structure, it is after all necessary for our colored parton theory to operate in the nucleus as well as in a QGP. Deuteron - gold collisions at RHIC are able to shed light on cold nuclear matter effects as discussed in the following sections.

1.1 Probing Quantum Chromodynamics

1.1.1 Quantum Chromodynamics

Quantum Chromodynamics (QCD) is the field theory that describes strong force interactions. Similar to the form of the Quantum Electrodynamics (QED) Lagrangian, its Lagrangian is:

$$\mathcal{L}_{QCD} = \bar{\psi}_i \left(i\gamma^\mu \partial_\mu - m_i \right) \psi_i - gG^\alpha_\mu \bar{\psi}_i \gamma^\mu T^\alpha_{ij} \psi_j - \frac{1}{4} G^\alpha_{\mu\nu} G^{\mu\nu}_\alpha \tag{1.1}$$

Just as in the QED case the field ψ is a spin 1/2 fermion, which in the QCD case is a quark (of *flavor* i - see below). G is the massless spin 1 boson field which is a gluon in QCD. The coupling strength of G to the quark field is denoted by g. The gluonic field tensor written in terms of the vector potential, A, is

$$F^\alpha_{\mu\nu} = \partial_\mu A^\alpha_\nu - \partial^\alpha_\mu A^\alpha_\nu + C^\alpha_{\beta\gamma} A^\beta_\mu A^\gamma_\nu \tag{1.2}$$

The final term in equation 1.2 is particularly note worthy; it represents *self* interactions of the gluon field and has no analogue in QED. Thus in addition to a quark emitting or absorbing a gluon just as an electron may emit or absorb a photon in QED, QCD allows wholly bosonic gluon emission and absorption of another gluon as well as direct two gluon interactions. This property arises from gluons themselves having a non-zero charge equivalent. Whereas in QED fermions have a quantum number slot that allows them to be positively or negatively charged, in QCD not only is the ‘charge’ available to the bosons it is also different in that it may take three values referred to as color. The color labels of red green and blue (R,G,B) are a convenient metaphor drawn from the visible spectrum in that color neutrality, ‘whiteness’, can be achieved either via a color - anticolor pair or a triplet of all three colors. These traits are described by the SU(3) group. In this vocabulary the group has generators,

T^{α}_{ij} that are eight 3x3 matrices, complemented by the constants that satisfy their commutation relations, $C^{\alpha}_{\beta\gamma}$.

In addition to the color quantum number which follows an exact gauge symmetry there is also a quantum number described by an SU(3) group corresponding to an approximate symmetry denoting the flavor of the quark. This symmetry holds for the three lightest quarks, u,d and s due to their similar mass but is broken by the heavy quark flavors c, b, and t. Nevertheless, the approximate symmetry was key in developing the map of bound hadronic states, known as the Eight-Fold Way [6], which led to the development of the parton (and subsequently quark) model.

1.1.2 Asymptotic Freedom and Deconfinement

Just as in QED, the strength of the coupling constant in the QCD Lagrangian is not constant but is a function of the momentum exchange in the interaction. This dependence is characterized by the Beta function of α_s (=$\mathrm{g}^2/4\pi$) which at lowest order for an SU(N) group theory is:

$$\beta(\alpha_s) = \frac{\alpha_s^2}{2\pi}\left(\frac{2n_f}{3} - \frac{11N}{6}\right) \tag{1.3}$$

where n_f is the number of quark flavors. So for the three colors of SU(3) as long as $n_f < 33/2$, β is negative; this follows from the non-Abelian nature of the group description of the gluons (i.e. the self interaction term of the Lagrangian) [7, 8]. Or cast as a function of the momentum transfer, Q:

$$\alpha_s(Q^2) = \left(\beta_0 \ln(\mathrm{Q}^2/\Lambda^2)\right)^{-1} \tag{1.4}$$

where perturbation theory requires that q be somewhat larger than the cutoff scale Λ (experimentally found to be $\approx$ 0.2 GeV and requiring that Q^2 be greater than $\approx$ 1 GeV [9]). Figure 1.1 summarizes results for the "running" coupling [10]. It is worth noting that besides having opposite sign the coupling strength varies much faster than that of QED.

The negative value of β has hugely important implications for the behavior of QCD interactions. Although it is quite unintuitive (at least to this author) this means that at lower momentum transfer or *longer* distances the strong force field's energy grows *larger*. This leads to the phenomena of confinement - free color charges are never observed for as the separation between quarks grows the energy gets so large that other quarks are created from the vacuum and they bind the attempted escapee into a hadronic state. This concept explains the failure to observe free quarks attempted experimentally shortly

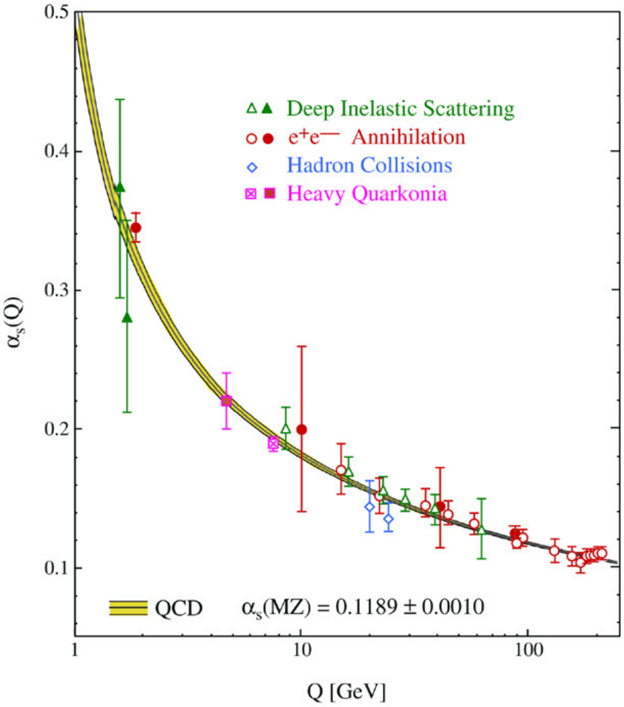

Figure 1.1: A summary of α_s(Q) measurements. Open symbols indicate (resummed) NLO, and filled symbols NNLO QCD calculations used in the respective analysis. Taken from [10].

after the quark model was developed. The long range effects of the strong force that are needed to describe the bound hadronic states, fall too close (or under) Λ and so can not be calculated perturbatively. Lattice QCD, in which large scales become calculable by using a discrete lattice rather than calculating in continuous space [11], has to some extent filled this breach.

On the other hand, at very large momentum transfer or very small distances quarks approach "asymptotic freedom". This has the happy result that at the appropriate energy scales perturbative calculations are again useful, but taken to its extreme has deeper implications. At sufficiently high density and temperature, the long range interactions ought to be screened by the local gluon color charge [12] similar to Debye screening in an electromagnetic plasma. Continuing the analogy we may consider a Quark Gluon Plasma in which the degrees of freedom are the quarks and gluons rather than the bound hadronic states [1].

To investigate this further we turn to the lattice QCD framework, which allows calculations at high temperature and large coupling strength. In particular, in the search for a phase transition from hadronic matter into a QGP, lattice QCD can calculate as a proxy for the degrees of freedom the energy density ϵ divided by the temperature to the fourth power T^4. As shown in Figure 1.2 the quantity ϵ/T^4 rises drastically at a certain temperature, T_C (calculated to be ≈ 170 MeV), and then remains flat as a function of temperature [13]. This behavior indicates a phase transition from a system of hadrons to a system with partonic degrees of freedom, i.e. a QGP. The figure also shows the Stephan-Boltzmann limit corresponding to an ideal gas of partons, which significantly surpasses the level of the apparent plateau of the calculated energy density. The failure of the number of degrees of freedom to reach this limit suggests that even following the phase transition the QGP phase is still strongly coupled (at least at the temperatures shown in the figure).

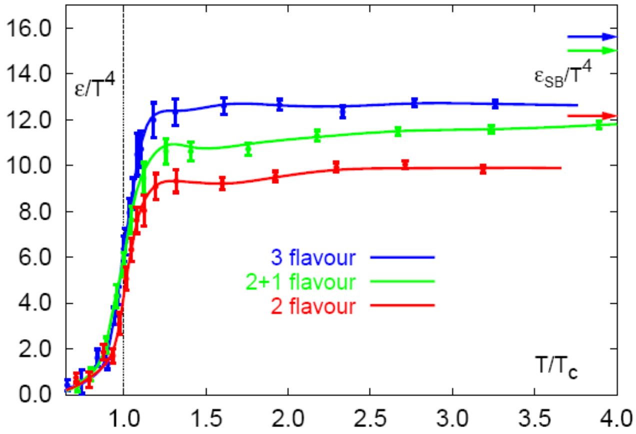

Figure 1.2: Lattice predictions for ϵ/T^4 ($\propto N_{DOF}$) as a function of temperature. The temperature scale is normalized to $T_C \sim 170$ MeV. The arrows on the right indicate the level of the Stephan-Boltzmann limit. From [13].

Therefore, we have good reason to expect that at the proper energy density hadronic matter should undergo a phase transition into strongly coupled partonic matter. This energy density presumably existed shortly after the Big Bang as the universe began its cooling expansion, it may also exist in neutron stars, but can we create it under laboratory conditions?

1.1.3 Ultra-Relativistic Heavy Ion Collisions

To produce an extremely hot and dense medium in controlled conditions the field has turned to highly energetic nucleus-nucleus collisions. Even in a high energy p+p collision we often must turn to a partonic level description of the proton to explain observed phenomena, *e.g.* jets, although it is difficult to say there is a state of matter being studied in this case. The innovation in heavy ion reactions is that the “fireball” created by the energy deposition of the nuclei at their collision is a discrete state of matter. In this case a partonic description should be appropriate even at low momentum scales and large distances.

Several colliders have pursued the goal of generating high energy density systems through heavy ion collisions beginning with the Bevalac at LBNL, through the AGS at BNL and the SPS at CERN. The advent of $\sqrt{s_{NN}} = 200$ GeV Au+Au collisions at RHIC seems to have decidedly broken the barrier into a new state of matter. Even given the production of the required energy density the matter produced is inherently elusive. Following the collision there is a rapid thermalization in no more than a few fm/c, after which there is expansion of the thermalized medium before a final hadronic state “freeze out” at greater than $\sim$ 15 fm/c. The key to identifying and studying the produced medium is measuring the various effects of the early stages of the system’s evolution through measured final state particles as well as the leptonic and bosonic channels that are not swayed by strong force interactions in the medium. There is very broad range of these measurements many of which are discussed in [5].

Particularly notable among the effects measured in Au+Au collisions at RHIC is the suppression of high transverse momentum collisions. The nuclear modification factor, R_{AA}, compares the number of produced particles in an AA collision to the production in a p+p collision scaled up by the appropriate mean number of binary collisions (see equation 3.13 in section 3.3.5). The measurement of this quantity in Au+Au collisions revealed a strong suppression of midrapidity charged hadrons and π^0s and was one of the earliest RHIC measurements that clearly showed a new regime of physics [14]. As seen in Figure 1.3, in the most central collisions the suppression reaches a factor of almost 5, and in more peripheral collisions the suppression all but vanishes. This is understood to demonstrate that in the more central collisions in which a QGP medium is created, the hard parton undergoes energy loss to the medium it is traversing.

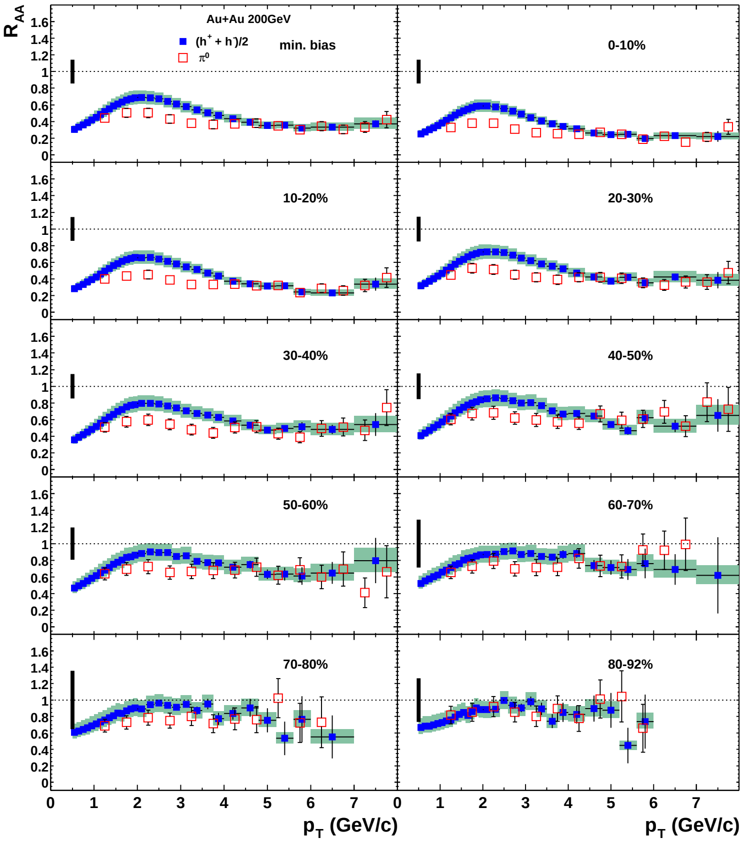

Figure 1.3: R_{AA} from Au+Au at $\sqrt{s_{NN}} = 200$ GeV in centrality bins.[14].

1.1.4 p+p and d+Au Collisions

The R_{AA} of the previous section illustrates the important role that a robust baseline measurement plays in understanding heavy ion physics. To normalize the particle yield from the raw p_{T} spectra to a quantity in which one may sensibly detect suppression we need to have the analogous spectra measured in p+p collisions at the same energy. This concept is a recurring one in heavy ion physics, for most measurements of novel physics processes found in the QGP medium it is necessary to have a baseline measurement of the same quantity in p+p.

Deuteron-gold collisions are also of great utility for understanding Au+Au collisions and QGP physics but their role is somewhat different. They are not a reference for Au+Au collisions in the way that p+p collisions are because they involve a nuclear medium - the Au nucleus itself. In the semi-heavy ion collision there is no hot dense medium formed, but any effects not found in p+p which are due to the 'cold' nuclear medium of the relativistic Au nucleus can be studied. To appreciate what of the measured physics in Au+Au collisions is actually due to the QGP we must be able to disentangle the initial state effects, which we can characterize in d+Au collsions. Returning to the R_{AA} example, we may define a nuclear modification factor also in d+Au collsions, R_{dAu}, and using d+Au as a control experiment compare this to the R_{AA} from Au+Au collisions. After all one could imagine that the strong suppression displayed in R_{AA} is due to initial state shadowing effects (see next section) and in this case we'd expect R_{dAu} to be similarly suppressed. This is the topic we are chiefly concerned with in Part II of this thesis.

We must be somewhat careful referring to d+Au as the control experiment, for it is one that is not fully controlled. There are many initial state conditions of the Au nucleus that are not yet fully understood. Understanding the relativistic Au nucleus is itself a fruitful probe of our knowledge of QCD and its implications. (The similar objection to using p+p only as a reference is also valid and p+p collisions too are a worthwhile topic of study.) In the next section we briefly review the underlying initial state nuclear matter properties both for their utility as a baseline for QGP studies as well as to enhance our understanding of the nucleus itself in the context of QCD.

1.2 Nuclear Structure in the Parton Model

1.2.1 Deep Inelastic Scattering

Deep inelastic scattering (DIS) is lepton-nucleon scattering at sufficiently high energy to resolve the partonic structure of the nucleon. Electron-proton DIS at SLAC in the late 1960's [15, 16] *was* the key evidence for the very existence of the parton model. Figure 1.4 shows the basic DIS interaction. We may write the differential cross section in terms of $Q^2(=-q^2)$ and Bjorken x (the fraction of the nucleon's momentum carried by the struck parton $x = Q^2/2\, P\cdot q = Q^2/2M\nu$, with the boson energy loss $\nu = E - E'$) as:

$$\frac{d^2\sigma}{dxdQ^2} = \frac{4\pi\alpha^2(E')^2}{xQ^4}\frac{E'}{E}\left(F_2 cos^2\frac{\theta}{2} + 2\frac{\nu}{M}F_1 sin^2\frac{\theta}{2}\right) \tag{1.5}$$

where α is the strong coupling constant and θ is the scattering angle. F_1 $(=MP)$ and $F_2(=\nu W)$ are known as the structure functions which encapsulate all information about the target's structure. An additional structure function term, F_3, arises from parity violation where relevant.

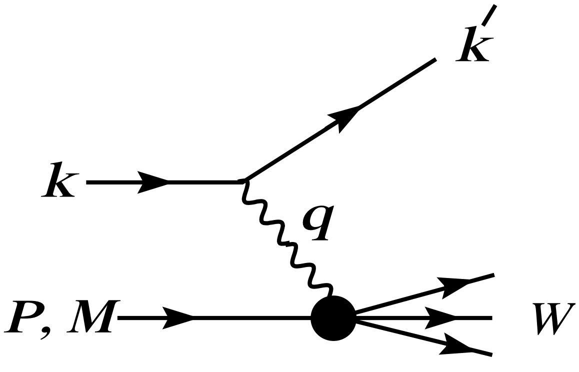

Figure 1.4: A diagram of a DIS interaction. With k and k′ the four momenta of the lepton incoming and outgoing, P the four momentum of the struck nucleon (with mass M), W the outgoing system, and q the four momentum transfered by the boson exchange. Taken from [17].

That the structure functions were largely independent of Q^2 and only a function of x, Bjorken scaling, at Q^2 greater than ~ 1 and $q \cdot P$ greater than ~ 3.5 GeV/c^2, indicates that the constituent partons are indeed point like, and therefore structure functions correspond to the *number* density of partons in the nucleon at a given x. As is intuitive, for a given Q^2 at lower x, i.e. in which the momentum fraction carried by quarks and gluons is smaller, the number density is greater. It is in this low x regime where gluons and sea quark-antiquark pairs dominate that we are concerned with in this work.

1.2.2 Shadowing, Anti-Shadowing, and the EMC Effect

Deep inelastic scattering experiments have demonstrated that the distribution of quarks inside a *nucleus* is significantly altered compared to the distribution within a nucleon. This is readily seen by comparing the cross sections or structure functions of deuterons to those of heavier nuclei. (Note that the ratios of the cross sections and structure functions are identical if the ratio of longitudinal to transverse cross sections is independent of A.) In 1983 the European Muon Collaboration published the ratio of the iron to deuteron cross sections from muon DIS as a function of Bjorken x, as shown in the inset of Figure 1.5 [18]. Further experiments have measured the effect in other heavy nuclei (for a summary see [19] and references therein); a sample of results are shown in Figure 1.5. More recently similar results have been observed in lighter nuclei [20]. As seen in Figure 1.5 the cross section ratios display three distinct regions of interest: at the lowest x the ratio is less than unity and is referred to as shadowing, at approximately 0.1< x < 0.3 it is enhanced and referred to as anti-shadowing, and the steady decline for 0.3< x <0.7 named for the discovering collaboration is known as the EMC effect (it is not easily seen in the figure but we may also count a fourth region at high x in which the ratio rises above unity due to Fermi motion). The EMC effect is an open topic of active interest (see [21] for an intriguing recent work) and ideally we'd like an understanding of the relevant physics in the nucleus over the full range of x, but in this work we are focusing on physics at x lower than the occurrence of the EMC effect.

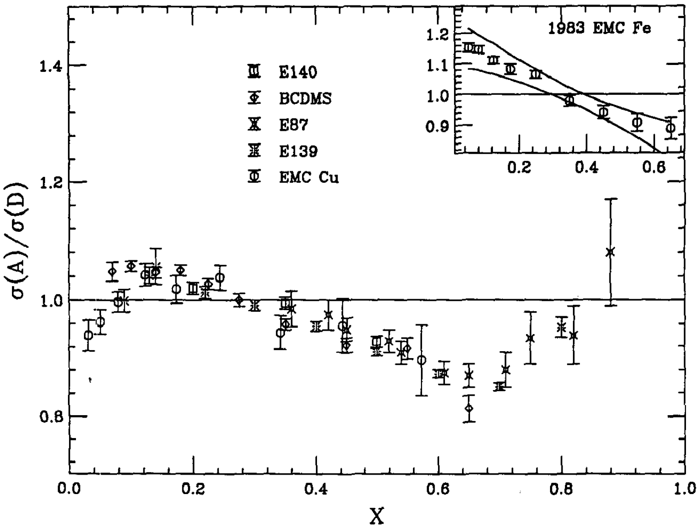

Figure 1.5: Ratios of the DIS cross sections of iron and copper targets to deuterons. The inset shows the original EMC effect observation. Figure is taken from [19].

Just as the origins of the EMC effect have yet to be definitively determined, the physics behind shadowing and anti-shadowing is also still somewhat murky, see [22] for a review of the topic. (Note that the term 'shadowing' is sometimes used to refer to the observation of suppression in the structure function or cross section ratios and sometimes to particular model descriptions of this phenomena, for clarity we will use shadowing to refer to the observations and try to describe models as such.) We may bracket consideration of shadowing in x, by defining two scales: x_{onset} the value of x below which shadowing occurs, and $x_{saturation}$ the value at which the ratio reaches its nadir [19]. The generally common basis for descriptions of shadowing is multiple scattering or coherence effects across the different nucleons in the nucleus. Assuming this position $1/x_{onset}$ should correspond to the point at which the nucleon-nucleon separation becomes comparable to the longitudinal size of the gluons. To estimate $x_{saturation}$ we consider the limit at which the virtual photon of the interaction "sees" the entire nucleus. We can estimate its lifetime as [22]

$$\tau \sim \frac{1}{Q} \times \frac{E_{lab}}{Q} \simeq \frac{(q+P)^2}{2M_{Nucleon}Q^2} \simeq \frac{1}{2M_{Nucleon}x} \tag{1.6}$$

where Q^2 is small compared to $(q+P)^2$. To achieve a maximally coherent interaction the lifetime must be greater than the nuclear radius R_A and so x roughly less than $1/2\mathrm{R}_A\mathrm{M}_{Nucleon}$.

We use from [22] a demonstration of how across different models coherence/multiple scattering effects result in shadowing phenomena (the reference and its references provides a more detailed working of the calculations than what is presented here). Figure 1.6 shows double and single scattering diagrams. We consider forward, i.e. elastic collisions with q = 0, with the optical theorem and have $it(q=0) = it_{forward} = -\sigma$ for the nucleon case. For the nucleus case we have multiple scattering, n, and $i\mathcal{T}_n(q=0) = -\sigma_A^n$. Performing the integrals for the single scattering case we have that $\sigma_A^1 = A\sigma$; as expected it appears just as a superposition of A single scatterings. The double scattering case results in an extra term $e^{-i(x_{2+}-x_{1+})/l_c}$ where $l_c = 2p_+/k_T^2$ and

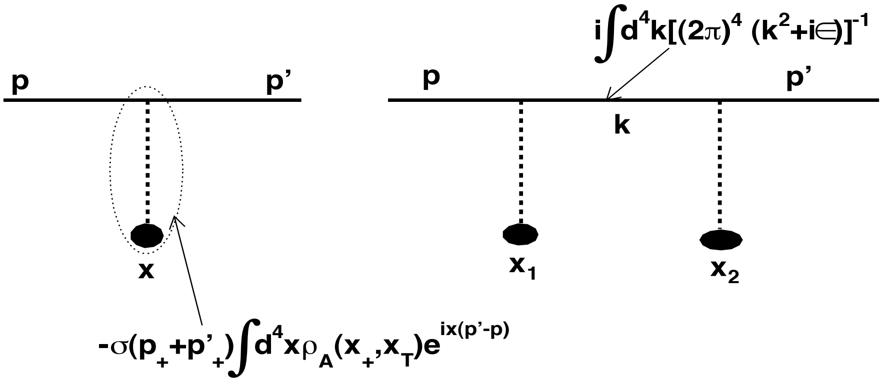

Figure 1.6: On the left a single scattering diagram and on the right double scattering, with q = p′ - p. The relevant Feynman rules are also displayed. Taken from [22].

may be taken as the coherence length. If we consider the limiting low energy case in which $p_+ \rightarrow 0$ then $i\mathcal{T}_2 \rightarrow 0$. In this case we see that all rescattering effects vanish and we return to the single scatter case in which the nucleus interaction cross section is just a superposition of nucleon cross sections. Thus, as we'd expect, in the *incoherent* limit shadowing is *not* present. However, if we consider the other limit in which $p_+ \rightarrow \infty$ then $e^{-i(x_{2+}-x_{1+})/l_c} \rightarrow 1$ and so we have

$$i\mathcal{T}_2(q) = \frac{A(A-1)}{2}(it_{forward})^2 \int d^2x_T e^{-ix_T(p'_T-p_T)} T_A^2(x_T) \tag{1.7}$$

where x_T is the impact parameter and $T_A(x_T)$ is the nuclear thickness (see equation 3.4). Taken at q = 0 we have

$$\sigma_A^2 = -\frac{A(A-1)}{2} \int d^2x_T [T_A(x_T)\sigma]^2 \tag{1.8}$$

and so we see that nucleus cross section in the double scattering case taken at the coherent limit is corrected *down* from the single case which was equivalent to a superposition of nucleon scatterings. Thus multiple scattering/coherence is a useful description of shadowing phenomena. Equation 1.8 also demonstrates naturally the increase of suppression with σ (which goes with energy), A, and smaller impact parameter.

The above discussion demonstrates how shadowing is naturally a low x coherence phenomenon, the anti-shadowing region may be described in a similar language as the product of constructive rather than destructive interference. If we look from the perspective in which in which we may consider the gluons as having spatial extent comparable to the nucleon-nucleon separation and think of them as 'fusing' with one another, it follows that the depletion of the lower momentum partons must be compensated by some increase of higher momentum ones.

The A dependence of anti-shadowing phenomena in the invariant hadron production cross section of a given particle species, I_i, has been parameterized as,

$$I_i(p_{\mathrm{T}}, A) = I_i(p_{\mathrm{T}}, 1)A^{\alpha_i(p_{\mathrm{T}})} \tag{1.9}$$

by Cronin following his discovery of the phenomenon [23]. The enhancement displayed at moderate x values corresponds to $\alpha > 1$ and is known as the "Cronin Effect". In this terminology the enhancement of hadron production at moderate p_{T} is generally considered to be due to multiple rescatterings of the parton (which may be thought of as a p_{T} broadening of the nuclear structure function). This is discussed in more detail in section 4.2.

In this section we have given only a very general overview of the mechanisms of modification in going from nucleons to a nucleus, there are many more detailed models in the field (see [24, 25, 26] for some examples as well as a fuller list of references in [22]).

1.2.3 Evolution Equations

There are two formalisms that are helpful to navigate QCD evolution for discussion of parton distributions. These are known as the Dokshitzer-Gribov-Lipatov-Altarelli-Parisis (DGLAP) equations [27, 28, 29] and the Balitsky-Fadin-Kuraev-Lipatov (BFKL) equations [30, 31] (we follow the presentation of DGLAP as in [32] and [9] and of BFKL as in [32] and [33]).

The DGLAP equations describes how the quark and gluon distribution change with the momentum scale; they are analogous to the β function that describes the running of the coupling strength. For a given momentum scale at which we may treat the partons as massless, Q, we have for the quark distribution, f_q:

$$\frac{d}{d\,\ln\mathrm{Q}} f_q(x,Q) = \frac{\alpha_s(Q^2)}{\pi}\int_x^1 \frac{d\xi}{\xi}\left\{P_{q\leftarrow q}(\xi) f_q(x/\xi,Q) + P_{q\leftarrow g}(z) f_g(x/\xi,Q)\right\} \tag{1.10}$$

and for the gluon distribution, f_g:

$$\frac{d}{d\,\ln\mathrm{Q}} f_g(x,Q) = \frac{\alpha_s(Q^2)}{\pi}\int_x^1 \frac{d\xi}{\xi} \left\{ P_{g\leftarrow q}(\xi)\sum_i \left[f_{q^i}(x/\xi,Q) + f_{\bar{q}^i}(x/\xi,Q)\right] + P_{g\leftarrow g}(\xi) f_g(x/\xi,Q)\right\} \tag{1.11}$$

to first order in α_s. The $P_{a\leftarrow b}(\xi)$ terms are known as the splitting functions and represent b going to a as shown for lowest order in Figure 1.7.

To use the DGLAP equations we assume the n emitted gluons have strongly ordered transverse momentum, i.e. $Q^2 \gg k_{n\mathrm{T}}^2 \gg ... \gg k_{1\mathrm{T}}^2$. However, in the case of of very small x but not such large Q^2 to the extent that $\ln Q^2 \gg \ln(1/x)$, DGLAP evolution neglects terms even in the leading power of $\ln(1/x)$ which do not also have $\ln Q^2$ terms. For an evolution scheme that includes resummation of all terms with $\alpha_s \ln(1/x)$ while keeping the entire Q^2 dependence we turn to the BFKL equation. The BFKL describes the parton density evolution in rapidity, y = $\ln(1/x)$, and is valid in the collinear DGLAP limit of Q^2 very large, the "anti-DGLAP" limit where Q^2 is very small, and when it is of the same order as k_T^2. Where DGLAP relied on ordering in momentum, BFKL

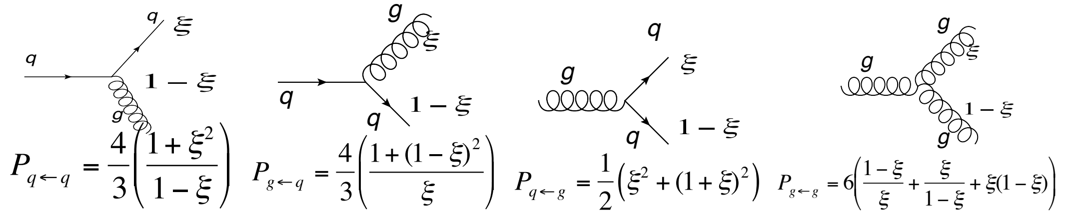

Figure 1.7: The splitting functions at lowest order. Note that to fix the singularity $P_{q\leftarrow q}$ has an additional term of $2\delta(1-\xi)$ and $P_{g\leftarrow g}$ has an additional $6(\frac{11}{12}-\frac{n_q}{18})\delta(1-\xi)$ term.

relies on x ordering. To think about BFKL evolution we consider parton evolution happening through bremsstrahlung gluon emission. This process is dominated by collinear production (and when the emitter is a spin 1 particle, i.e. a gluon, lower x production). The produced gluons themselves may radiate softer gluons, and so there is recursively multiplying gluon production although each emission is suppressed by α_s. However if the value of x is sufficiently small, roughly speaking $\alpha_s \ln(1/x)$ greater than unity, the younger generations of production remain significant and it is natural that their summation be exponential in y so we have for the gluon count:

$$x\frac{dN_g}{dx dk_{\mathrm{T}}^2}\sim\frac{\alpha_s C_R}{\pi}\frac{1}{k_{\mathrm{T}}^2}e^{\omega\alpha_s y} \tag{1.12}$$

where C_R is N_c for a gluon emitter and $(N_c^2-1)/2N_c$ for a quark, and ω is a normalization constant. The BFKL equation describes the number of gluons of a color per unit rapidity and transverse phase space (k_{T} and b_{T} the transverse impact parameter)- the occupation number:

$$n(y,k_{\mathrm{T}},b_{\mathrm{T}})=\frac{(2\pi)^3}{2(N_c^2-1)}\frac{dN_g}{dy\ d^2k_{\mathrm{T}}\ d^2b_{\mathrm{T}}} \tag{1.13}$$

The DGLAP and BFKL formalisms are not naturally compatible, however, there have been efforts made to describe large and small x together notably the Catani-Ciafaloni-Fiorani-Marchesini (CCFM) approach which uses emission angle ordering [34, 35, 36] which is comparable to both[37].

1.2.4 Saturation and the Color Glass Condensate

As alluded to in the previous section, the gluon density increases as we look in lower x. This has been measured by HERA [38] as shown in Figure 1.8.

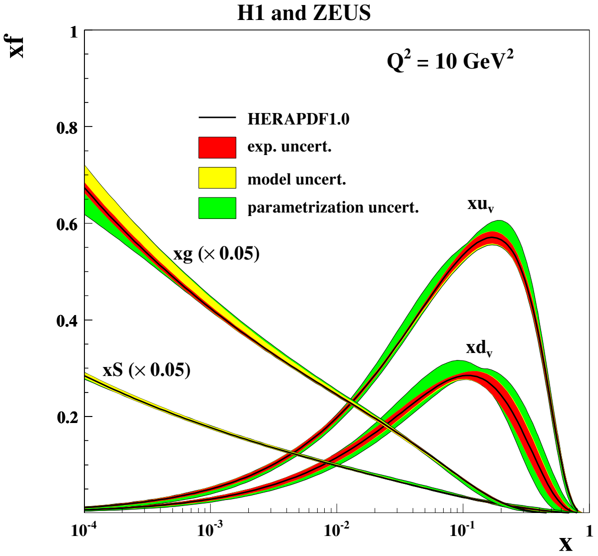

Figure 1.8: The x evolution of the parton distributions as measured by HERA. Taken from [38].

Following BFKL evolution as in equation 1.13 we can demarcate certain regions of gluon density: when $n \ll 1$ the gluon density is low enough that gluon-gluon interactions are insignificant, when it is of order 1 the gluons do overlap but those interactions are suppressed at the level of α_s ($\ll 1$), however when n is of order $1/\alpha_s$ the interaction strength is of order 1. In the region where the gluon density is so high that overlapping gluon interactions become significant, non-linear effects must be taken into account and for this Color Glass Condensate (CGC) was developed. The name refers to the gluons being colored, glass in that the associated fields evolve very slowly and are disordered just as glass is a disordered liquid only on very long time scales, and a condensate because the gluon density saturates at the point when its interactions prevent any further gluon occupation. Figure 1.9 shows a cartoon of QCD evolution and saturation's place in it. As shown in the figure it is useful to define a saturation scale, $Q_s(x)$ the boundary beyond which gluons have maximal occupation. Besides the obvious x dependence of Q_s there is also an A dependence following the relativistic contraction of the parton density in the nucleus observed from the probe's frame, so that the larger the nucleus the higher in x saturation is relevant. The literature on this topic is quite large and we here provide a brief summary chiefly following reviews [33] and [39].

CGC describes the nucleus, and even a single proton at the appropriate

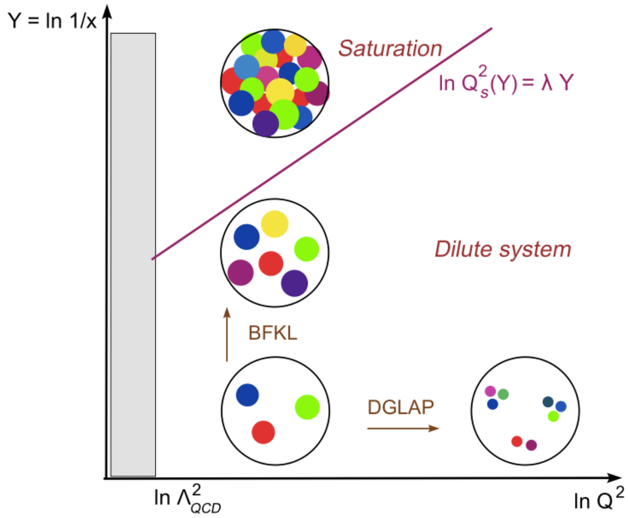

Figure 1.9: A cartoon of QCD evolution. Taken from [33].

scale, as a dense many body gluonic system expressed as an effective field theory. It is built on two types of degrees of freedom: fast gluons that are 'frozen' by time dilation as point sources, and slower gluons that make up the dynamical fields. The fast sources for the fields are specified by a color current $J_a^\mu = \delta^\mu \rho^a$ (where ρ^a is the color density). They may be thought of as generating the slower gluons fields - A^μ [40, 41, 42]. The two are separated by a cutoff scale in momentum. This is illustrated in Figure 1.10. To ensure gauge invariance the Jalilian-Marian - Iancu - McLerran - Weigert - Leonidov - Kovner (JIMWLK) renormalization group is used [43, 44, 45, 46, 47, 47].

For the CGC picture to be complete it is necessary to have a model for the gluon distribution as the initial conditions of the JIMWLK evolution. The McLerran-Venugopalan model for the gluon distribution in a large nucleus [40, 41, 42] describes a gluonic system beyond the saturation scale but in which the radiation (i.e. evolutionary) effects are still small. With these assumptions a probe would still be sensitive to the large coherent color charge of the nucleus. In this model the gluon density is:

$$\frac{dN_g^A}{dy d^2b d^2k_\mathrm{T}} = \frac{d(xg_A)}{d^2b d^2k_\mathrm{T}} \propto \frac{1}{\alpha_s} \int \frac{d^2x_\mathrm{T}}{x_\mathrm{T}^2} e^{-ix_\mathrm{T}k_\mathrm{T}} \left(1 - e^{-x_\mathrm{T}^2 Q_s^2/4}\right) \tag{1.14}$$

and the saturation scale, Q_s^2, is proportional to $AT_A(b)g_{nucleon}$. The McLerran-Venugopalan model is useful not only as the initial condition for JIMWLK evolution but is also relevant for collisions where the x region probed is (still

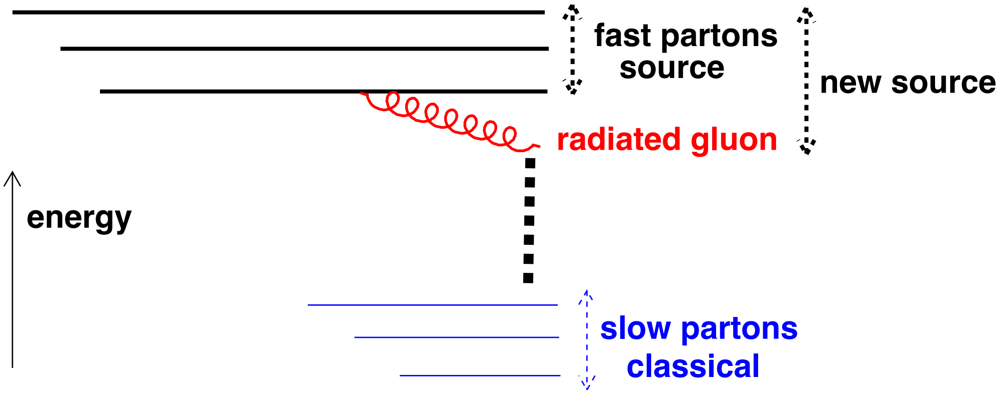

Figure 1.10: A cartoon showing the separation between the classical slow gluons and the fast source charges in the CGC model. Taken from [22].

small but) large enough that it does not require evolution.

1.3 Observables

As mentioned above in the R_{AA}, R_{dAu} example the measurement of hadronic single particle p_{T} spectra is a powerful way to look at the medium be it hot or cold in heavy (and semi-heavy) ion collisions. The measurement of the hadronic R_{dAu} at midrapidity serves as the essential control experiment to frame the suppression seen in R_{AA}. Further, to the extent that shadowing and anti-shadowing are relevant, we expect there to be a rapidity dependence in the single hadron yield. The trend of the nuclear modification factor in rapidity has been measured in d+Au collisions at RHIC by PHENIX[48], BRAHMS[49], and STAR[50] as shown in Figure 1.11.

Besides the single particle spectra, we may also consider two particle measurements. As proposed in [51], two particle correlations from forward to midrapidity are a sensitive tool to probe the underlying nuclear medium. The decorrelation of back to back particle production may be an important signature of saturation or other shadowing effects in the Au nucleus. In a CGC model a jet even with substantial p_{T} can be balanced by the production of multiple gluons with $p_{\mathrm{T}} \sim Q_s$. A similar effect is predicted without assuming CGC saturation, just based on coherent scattering off of multiple partons from different nucleons [52]. This is discussed in greater detail in 5.1 and in 7.

Following this and the proceeding chapter which introduces the PHENIX

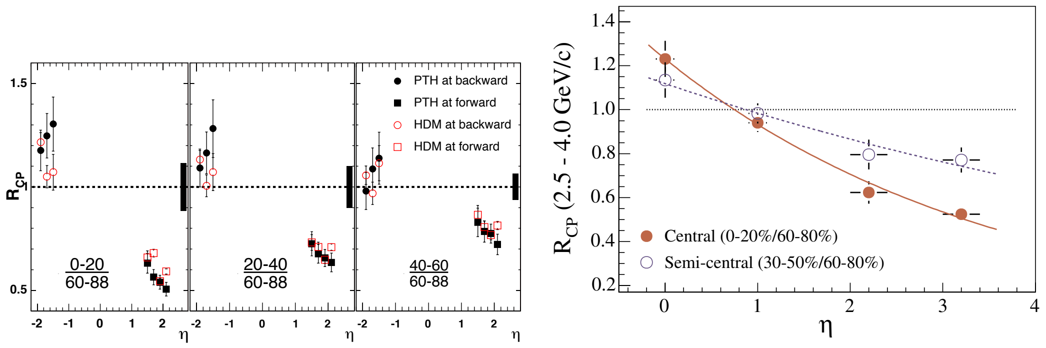

Figure 1.11: Nuclear modification factor as function of psuedo-rapidity, η. From left to right: PHENIX [48], and BRAHMS[49]. Note that the results are expressed as R_{CP} rather than R_{dAu}, meaning that rather than quantifying the modification compared to p+p the more central data is compared to the most peripheral data. The PHENIX data is for 1.5<p_{T}<4 GeV/c, and BRAHMS for 2.5<p_{T}<4 GeV/c.

experiment, this thesis is composed of two distinct analyses in the d+Au system in RHIC. Both analyses are, in their essence, investigations of the 'cold' Au nucleus through scattering with the deuteron. The first (Part II) is the study of unidentified charged hadrons produces at midrapidity from the 2003 RHIC physics run; the second (Part III) is an investigation of rapidity separated particle production in the 2008 RHIC physics run.

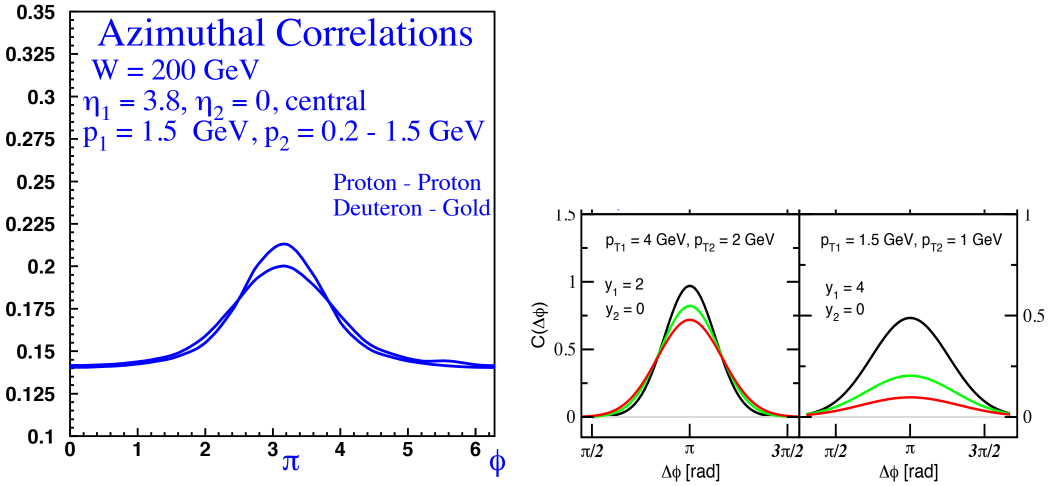

Figure 1.12: Predictions for rapidity separated two particle correlations in a CGC picture [51] on the left and from coherent multiple parton scattering [52] on the right (black is p+p , green is minimum bias d+Au, and red is central d+Au.

Chapter 2

The PHENIX Experiment

This chapter describes the Pioneering High Energy Nuclear Interaction eXperiment (PHENIX), with which the data for this thesis was measured.

2.1 The Relativistic Heavy Ion Collider

The Relativistic Heavy Ion Collider (RHIC) at Brookhaven National Laboratory produces heavy ion collisions of several different species and at different energies. RHIC has produced collisions of p+p, d+Au, Cu+Cu, and Au+Au with energies ranging from $\sqrt{s_{NN}}$ of 9 GeV up to 200 GeV (and up to 500 GeV in p+p collisions). The first RHIC run was in 2000 and it is embarking on its tenth run at the time of this writing. It is a versatile machine with the capability to produce asymmetric d+Au collisions, polarized proton beam collisions to probe the proton spin structure, and in the future will be able to collide uranium on uranium.

At RHIC, ions are accelerated in two counter circulating beams with six interaction intersections, four of which are used for experiments. An aerial view of RHIC is shown in Figure 2.1. The PHOBOS experiment was in operation until 2005, and measured charged particle multiplicity in a large aperture covering almost the whole solid angle as well as identified particles in a smaller aperture. The BRAHMS experiment took data until 2006, measuring charged hadrons over a broad range of p_{T} and rapidity. The STAR and PHENIX experiments are still active in data taking. The major results of all four experiments from the early years of RHIC running are summarized in [2, 3, 4, 5].

The analysis and results presented herein are based on data taken at PHENIX in the 2003 and 2008 d+Au and p+p runs.

Figure 2.1: The RHIC facility as seen from the air. The circumference of the main RHIC ring is 2.4 miles.

2.2 PHENIX Overview

PHENIX is a sophisticated experiment that consists of several independent detector subsystems. In PHENIX, we define the coordinate system to have the z-axis in the beam direction pointing north, the x-axis pointing west, and the y-axis perpendicular to them. The tracking system measures electrons and charged hadrons at midrapidity with two central arm spectrometers and muons at forward rapidity with two more spectrometer arms. The central arms are located at psuedorapidity $|\eta|$ <0.35, and each arm covers $\pi/2$ in the azimuthal angle. The central arm spectrometry takes place in two detector subsystems: the inner Drift Chamber (DC) and the outer Pad Chambers (PC1, PC2, and PC3). Between the inner tracking of the the DC and PC1 and the outer tracking of the PC3 there are several particle identification detectors: two time of flight detectors,TOF and Aerogel, a Time Expansion Chamber (TEC), and a Ring Imaging Cherenkov detector (RICH). There is also electromagnetic calorimetry coverage for photon measurements in the central arms. The electromagnetic calorimeter in the central arms is composed of two types: most of the coverage is lead scintillator (PbSc) and a smaller section of lead glass (PbGl). Further forward than the muon spectrometer arms with the Muon (Arm Magnet) Piston Calorimeters (MPCs). The MPCs are located at $3.1<\eta<3.9$ in the north direction, and $-3.1>\eta>3.7$ in the south direction. In addition there are global detectors that provide the event trigger as well as event level information such as collision time and vertex position. This information is obtained primarily with Beam Beam Counters (BBCs). Supplementary event level information is provided by a Zero Degree Calorimeter (ZDC) and Forward Calorimeter (FCAL). Figure 2.2 shows a schematic of the PHENIX detectors as they were in Run 8 (2008). In the following sections the detector systems used in the present analyses are discussed.

2.3 PHENIX Global Detectors

2.3.1 Beam Beam Counters

The BBCs [53] are two arrays of 64 Photo Multiplier Tubes (PMTs) mounted on quartz Cherenkov radiators. These measure fast charged Cherenkov radiating particles, with a dynamic range spanning 1 to 30 minimally ionizing particles. This broad sensitivity allows the BBC to operate in the full range of RHIC collisions. They are located 144 cm away from the interaction point corresponding to $3.1 < |\eta| < 3.9$. Each BBC has an outer radius of 30 cm and inner radius of 10 cm. Figure 2.3 shows a photograph of the BBC elements.

The BBCs are used to measure several important pieces of information for each collision as well as acting as a "minimum bias" trigger for PHENIX. By measuring the charged particles in each BBC and finding the average arrival times t_{BBCN} in the north and t_{BBCS} in the south we may determine the collision time, t_0:

$$t_0 = \frac{t_{BBCS} + t_{BBCN}}{2} \tag{2.1}$$

, and the z-position of the collision vertex, z_{vertex}:

$$z_{vertex} = \frac{c(t_{BBCS} - t_{BBCN})}{2} \tag{2.2}$$

If the measured vertex position is found to be within 30 cm of the nominal interaction point, the BBC sends the minimum bias trigger signal. Further, the BBC is used for centrality determination of an event as discussed in section 3.2.2.

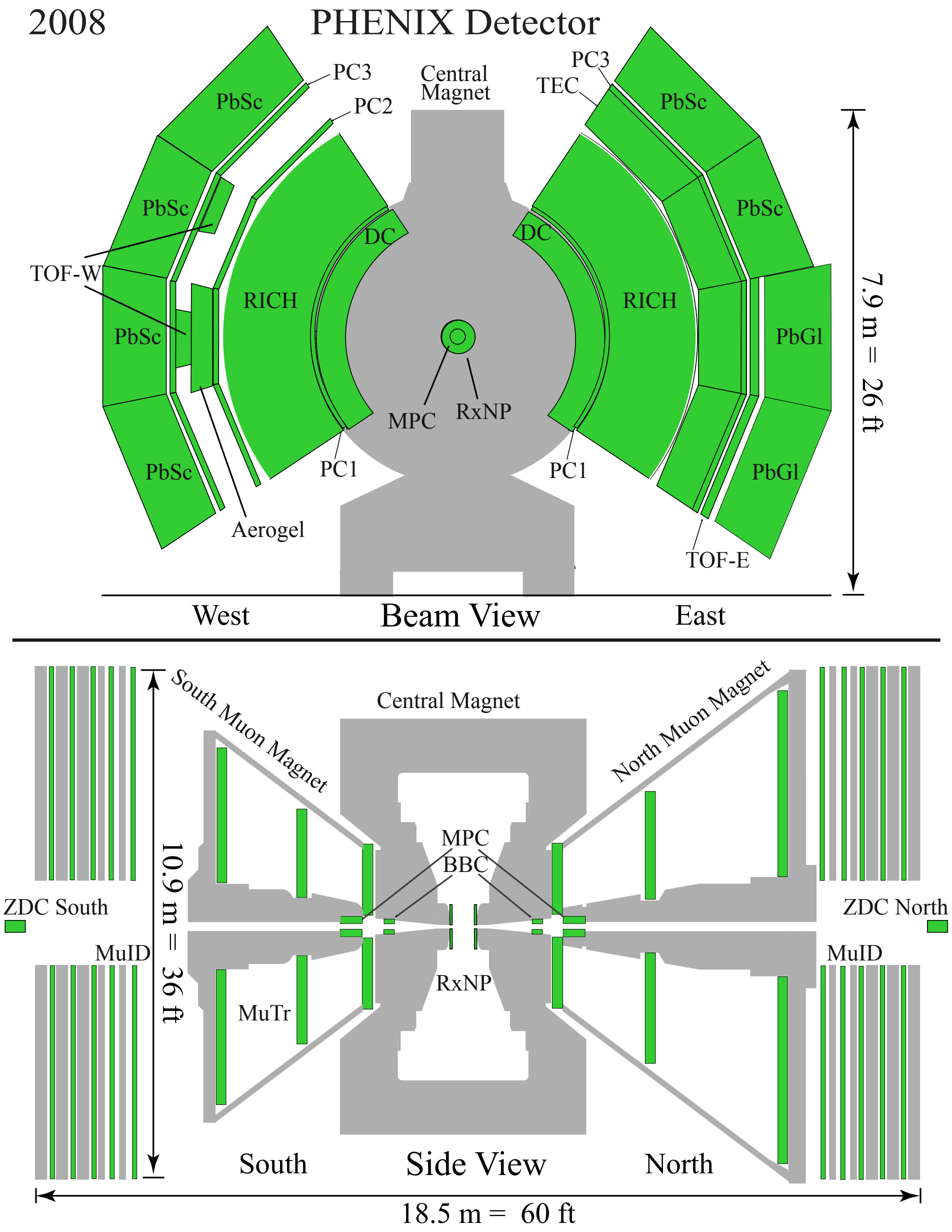

Figure 2.2: A schematic view of PHENIX in Run 8 (2008). On top it is viewed looking on the beam axis, and on the bottom viewed across the beam pipe.

Figure 2.3: On the left a photograph of the BBC array, and on the right a single PMT and radiator element.

2.3.2 Zero Degree Calorimeters and Forward Calorimeters

Zero Degree Calorimeter

The ZDCs [54] are hadronic calorimeters installed 18 m up and downstream from the interaction point. Each ZDC is made up of three tungsten alloy plate modules, read out by a PMT. The depth of the plates corresponds to two hadronic interaction lengths. Figure 2.4 shows a schematic view of the PHENIX global detectors. The ZDCs are a common feature of all four RHIC experiments.

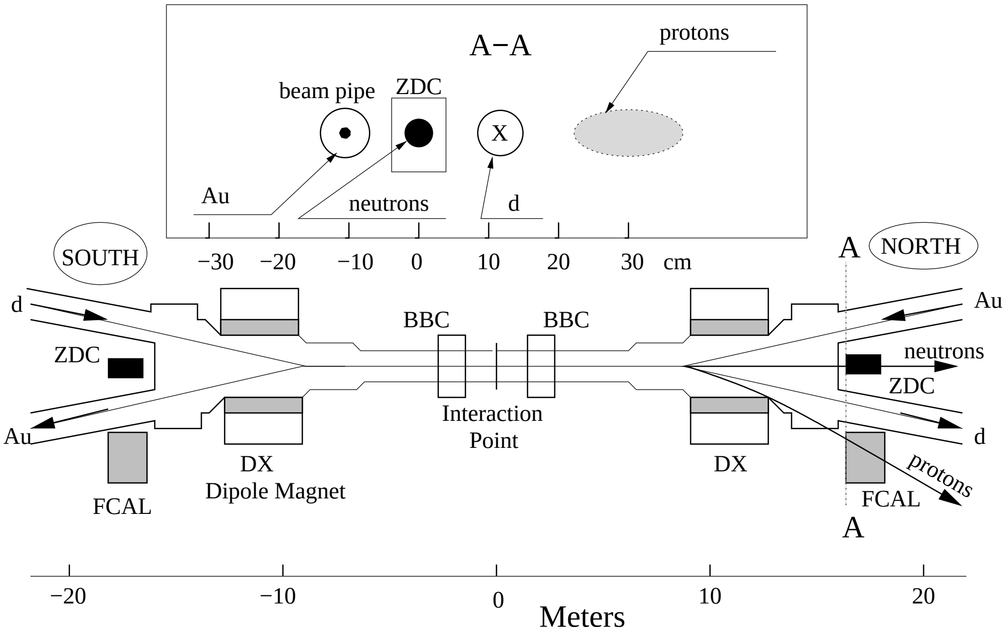

Figure 2.4: FCAL, ZDC and BBC positions relative to the vertex. The vertical scale in the figure is arbitrary. The insert at the top shows the position of primary beam, spectator neutron and proton spots at the FCAL and ZDC locations; deuteron beam, spectator neutrons and protons go into the plane, and the Au beam is coming out of the plane.

The purpose of the ZDC is to measure spectator neutrons. At 100 GeV per nucleon, neutrons evaporated from the spectator remnants of the collision are emitted within one mrad from the colliding beam direction. Charged fragments and the non-interacted primary beam are bent by deflecting magnets (DX) to much larger angles and away from the ZDC. The ZDC measures the total neutron energy within a small cone and with this provides the number of spectator neutrons from the interacting nucleus. In Au+Au running the ZDCs are used along with the BBC for centrality determination, however they are not used for this purpose in *d*+Au collisions. In *d*+Au, the d-going side (north) ZDC is used to tag events in which only the proton from the deuteron interacted with the Au nucleus (see section 3.2.3). The ZDC on the North side measured 100 GeV neutrons from deuteron fragmentation with resolution σ =28 GeV.

Forward Calorimeter

The FCAL [55] is a hadron calorimeter consisting of lead scintillating fiber modules originally used in Brookhaven AGS experiment E864 rearranged into two 9 by 10 arrays. The only difference from the E864 experiment is the readout electronics, which are identical to PHENIX central arm electromagnetic calorimeter electronics. The size of each module is 10 cm × 10 cm × 117cm, the average tower density is 9.6 g/cm3, the total length corresponds to 60 nuclear interaction lengths. The two arrays are located 18m from the interaction point along the beam pipes downstream of the first beam-line deflecting magnet (DX) (see Figure 2.4).

The d-going side (north) FCAL is used in *d*+Au collisions as the complement of the ZDC, by measuring spectator protons from the deuteron. The DX magnets which deflected charged particles away from the ZDC, work as sweeping magnets for bending spectator protons *into* the FCAL aperture. The FCAL measured the energy of spectator protons with a resolution of σ =40 GeV for a 100 GeV proton from the deuteron fragmentation (see section 3.2.3).

2.4 PHENIX Central Arm Detectors

The two PHENIX central arms are slightly azimuthally asymmetric: the west arm covers $-\frac{3}{16}\pi < \phi < \frac{5}{16}\pi$ and the east arm $\frac{11}{16}\pi < \phi < \frac{19}{16}\pi$. The detectors used in the present analyses and discussed below are symmetrically instrumented in the two arms.

A stable magnetic field is crucial for robust tracking in the central arm. The central magnet is composed of inner and outer Helmholtz coils inside a steel yoke. With current, these generate an axially symmetric magnetic field around the beam pipe inside PHENIX. Figure 2.5 shows the magnetic field lines when both coils are energized with current in the same direction. As can be seen in Figure 2.5 where the detector instrumentation starts at about 2 m from the beam pipe, the magnetic field is almost canceled. This allows the tracking model to make the assumption of straight tracks, once the particle has reached the detectors. In this configuration a charged particle ‘feels’ a field integral of $\int \mathbf{B} \cdot d\mathbf{l} = 1.15$ T·m.

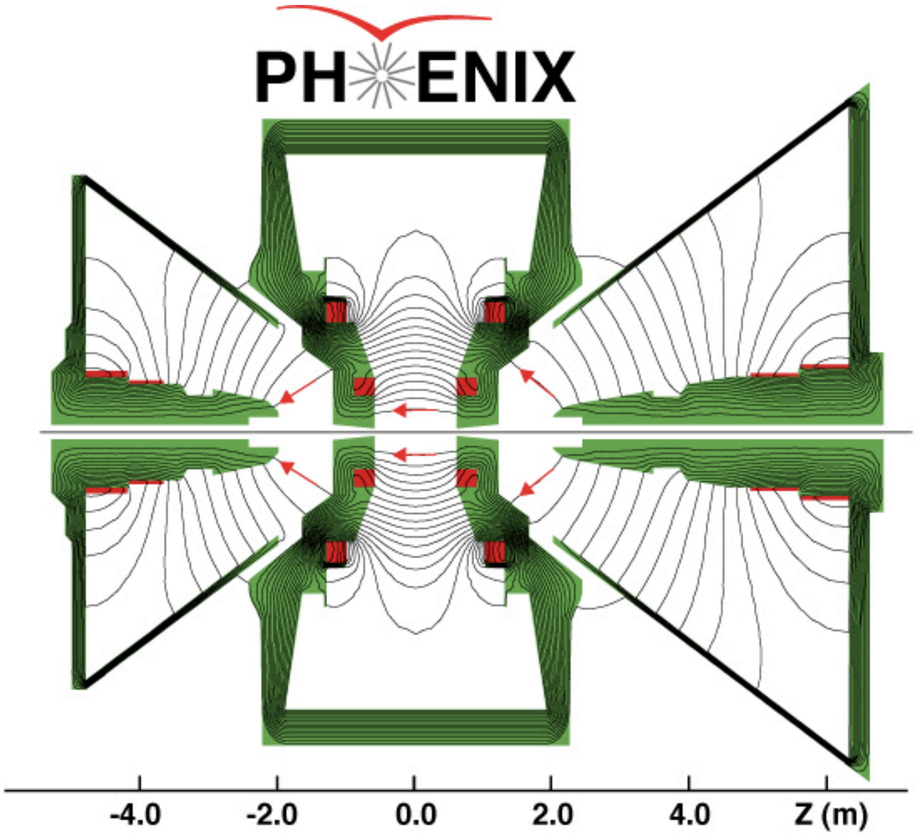

Figure 2.5: Magnetic field lines created by the PHENIX central arm and muon arm magnets.

2.4.1 Drift Chambers

The heart of PHENIX tracking is the Drift Chamber system (DC) [56]. Each chamber is a multiwire gas chamber located between 202 cm and 246 cm from the beam pipe. They sit in cylindrical titanium frames with mylar windows. Figure 2.6 shows the DC schematic.

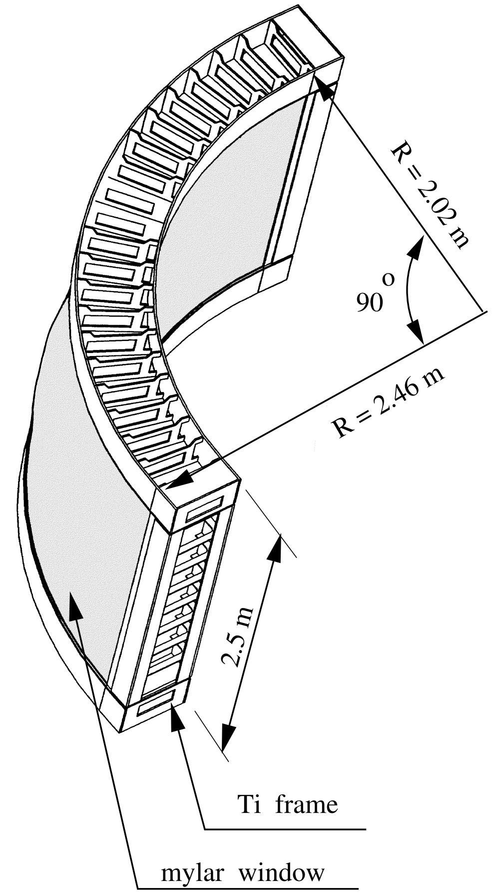

Figure 2.6: A schematic view of a DC arm.

Inside the DC a charged particle will randomly ionize the gas through which it is traversing. The gas used is 50% argon and 50% ethane; this combination gives stable drift velocity, high gain, and a low diffusion coefficient. The ionization electrons will drift towards an anode wire in a time that, because of the stable drift velocity, will be proportional to their starting distance from the wire. There are a total of 6500 anode wires crossing the chamber organized in twenty "keystones" (sectors), each covering 4.5° in the azimuthal angle. Two layers of anodes, X1 and X2, lie on the beam axis, and four stereo wires, U1,V1,U2, and V2, are rotated by 6° with respect to them. The X wires provide the $r - \phi$ plane information and the U and V wires the $\hat{z}$ information. The keystone and wire orientations are shown in Figure 2.7. Each wire is split

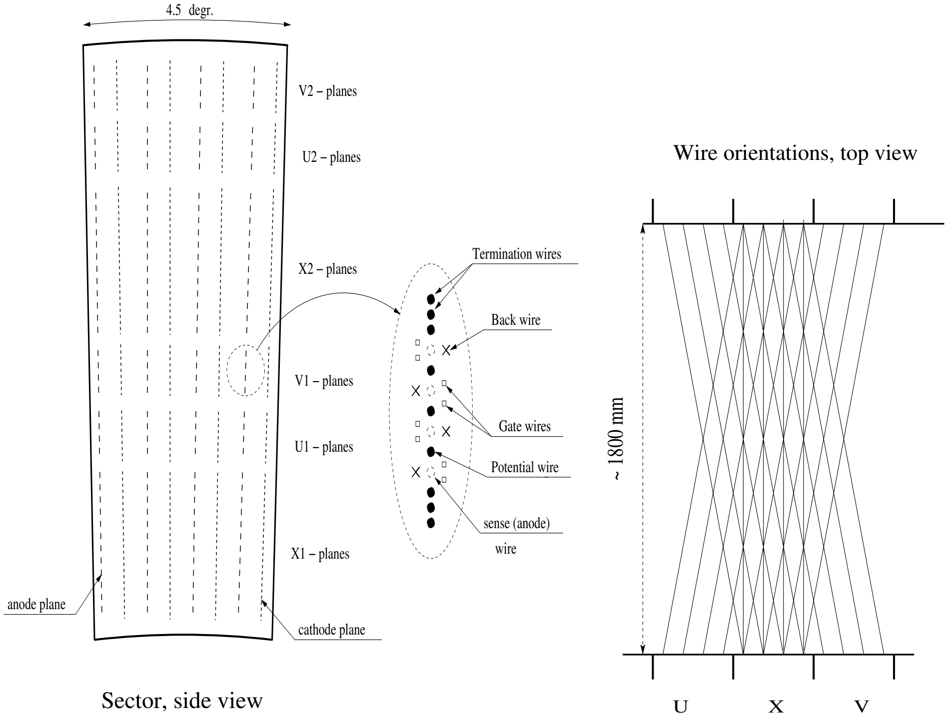

Figure 2.7: A side view of a single keystone on the left, and a top view of the wire orientations on the right.

in two by a piece of non-conductive kapton defining two discrete sides of every wire, doubling the available bits for pattern recognition in the tracking, thus enabling effective tracking even in a high multiplicity environment.

In addition to the anodes there are several other wires necessary, as seen in the inset of the left side of Figure 2.7. The potential wires keep a voltage to make the electric field that terminates at the cathode. The gate wires create the charge collection regions to constrain the track drift length. The back wires are at a low potential and thus block tracks from one side of the anode wire. This allows unambiguous determination of which side of the anode the ionized electrons of a track had drifted from.

An ideal track would leave 6 hits in the X layers of the DC. However, although the individual wire efficiency is very good varying between 90% and 95%, it is not perfect and so we require only 4 hits to form a track. With this requirement the single track efficiency is greater than 99%.

The information collected from the DC is reconstructed into a track via a combinatorial Hough transformation [57] (which assumes a zero magnetic field - straight line trajectory inside the detector). The Hough transformation outputs the angles ϕ and α as demonstrated in Figure 2.8.

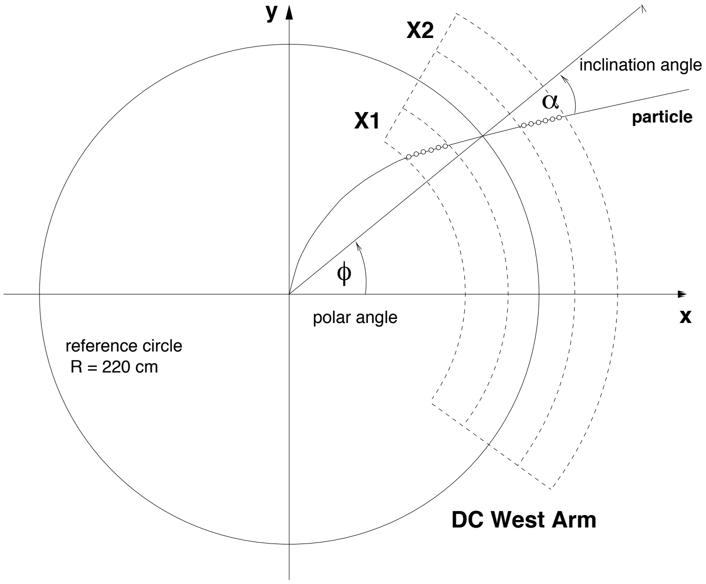

Figure 2.8: Definition of the ϕ and α coordinates outputted by the Hough transformation of the DC wire hit information.

Background tracks are removed by evaluating each hit of a putative track in a two step process. First each is given a weight based on its closeness to a straight line track, with a weight of zero for far away hits. Then each hit is associated to only one track, the closest one, and removed from all other tracks. Tracks must have at least 8 total hits to be further considered. The next stage of the tracking occurs based on information from the first layer of the pad chambers (PC1).

2.4.2 Pad Chambers

Beyond the DC described above, there are three layers of multi-wire pad chambers [56] installed in the central arms - PC1, PC2, and PC3 - as seen in the upper panel of Figure 2.2. Each chamber is composed of a wire layer bookended by two cathodes as seen in Figure 2.9. One of the cathodes is segmented into an array of pixels. A cell is defined of three pixels, and to avoid false positives a signal is required in all three pixels of a cell for a hit.

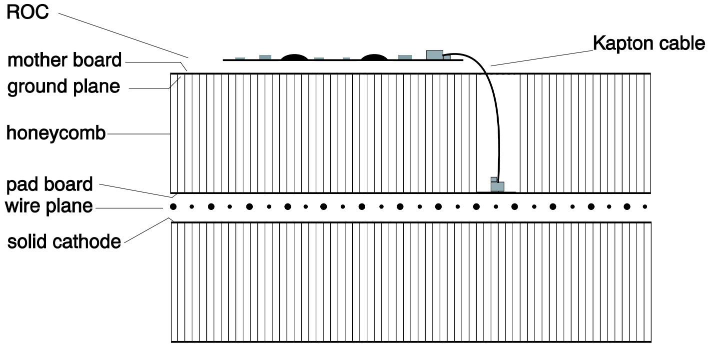

Figure 2.9: A vertical cut through a chamber view of the PC.

The PC is the only non-projective detector of the tracking system, and is thus a crucial element of the pattern recognition. The PC1 just beyond the DC fixes the third dimension of the track's position by providing the $\hat{z}$ coordinate at the DC exit. On the other hand the PC3 is far enough away that it is used for rejection of background composed of low momentum particles that will undergo multiple scattering between the DC exit and the PC3. We may use the displacement of the track projection from the DC to the nearest hit in the PC3, in both ϕ and z directions, as a valuable background discriminant.

Taken together the DC and PC1 (and using the vertex determined by the BBC) provide central arm tracking efficiency of approximately 98% independent of p_{T}. There is negligible centrality dependence at d+Au occupancy levels. The particle momenta are measured with a resolution $\delta\, p/p \;=\; 0.007 \oplus 0.011p$, where p is in GeV/c.

2.4.3 Ring Imaging Cherenkov Detectors

The RICH detectors are used to distinguish electrons from hadrons in PHENIX. The RICH [58] detectors are located outside the DC and PC1 in both PHENIX arms as seen in Figure 2.2. Each detector has an 8.9 m^2 entrance window, a 21.6 m^2 exit window, and a volume of 40 m^3. Inside the detector are 48 mirror panels composing a 20 m^2 reflecting area in two intersecting spherical surfaces. A schematic of the detector is in Figure 2.10.

The RICH uses CO$_2$ as the radiator gas, which has a refractive index of n-1 = 410×10^{-6}. A charged particle will emit Cherenkov radiation at angle θ_C if its velocity is greater than the speed of light in the medium, $c_n = c/n$,

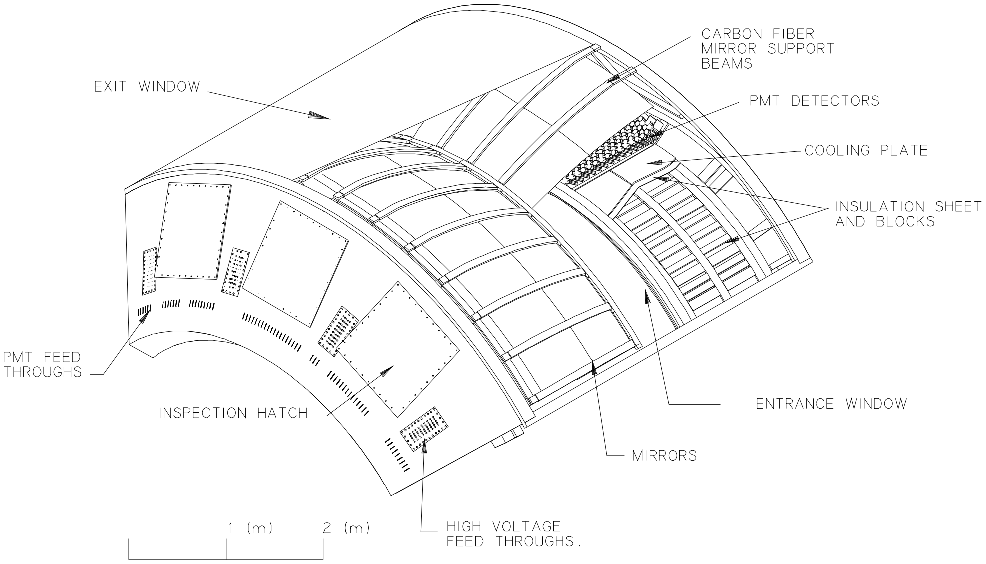

Figure 2.10: A cutaway view of a RICH chamber.

where $\cos(\theta_C) = 1/(n\beta)$. In CO_2 this comes out to a threshold of velocity of $\beta_t = 1/n = 0.99590168$, and consequently a momentum threshold of $p_t = m\gamma_t\beta_t = 0.018$ GeV/c for electrons and 4.87 GeV/c for charged pions. This allows for a RICH signal below the pion threshold to provide a hadron rejection rate of 10^4 to 1. Cherenkov radiation produced in the detector is focused onto an array of PMTs located on either side of the entrance window. Assuming a velocity of $\beta \approx 1$, a radiating charged particle produces an average of 10 photons which are focused into a ring with asymptotic radius of approximately 11.8 cm.

2.5 PHENIX Forward Detectors - MPC

Preceding the 2007 RHIC physics run, the north Muon Piston Calorimeter was installed in PHENIX and preceding the 2008 run the south MPC was installed (an earlier model south MPC was installed for the 2006 run but was subsequently removed). Prior to the installation of the MPCs PHENIX forward and backward tracking were limited to the muon arms located at $1.4 < |\eta| < 2.0$ (it is worth noting that the muon arms are capable of detecting "punch-through" hadrons in addition to muons [48, 59].) The north and south

MPCs, so named because of their location in the space of the muon arm magnet piston (see Figure 2.11), added electromagnetic calorimetry at 3.1< η <3.9 and -3.1> η >-3.7, respectively. The detectors each have full 2π coverage in the azimuthal direction.

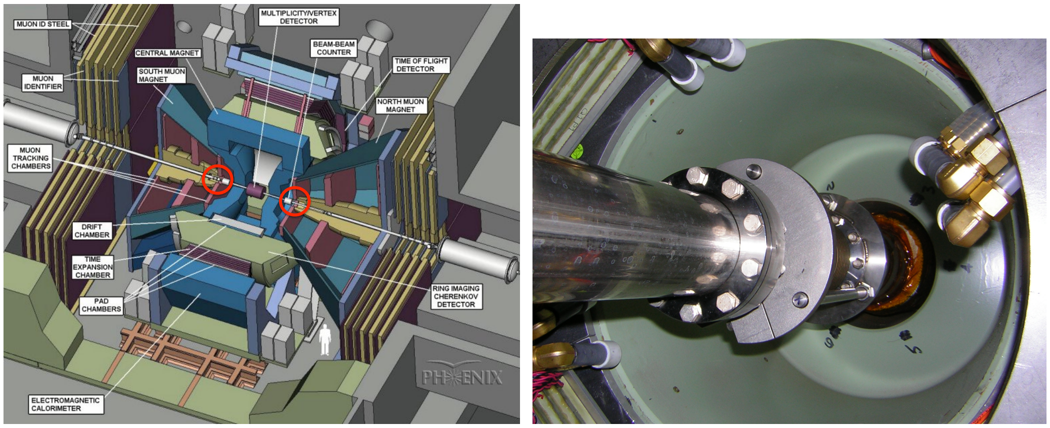

Figure 2.11: On the left a cutaway schematic of PHENIX with the muon magnet piston holes highlighted, and on the right a photograph of the hole in the muon arm magnet piston before installation of the MPC.

The basic element of the MPC is a tower composed of a lead tungstate crystal coupled to an avalanche photodiode. Each tower is 2.2 × 2.2 cm^2 laterally and 18 cm deep. Each has a radiation length of $20X_0$ and a Molière radius of 2.0 cm. The crystals were originally made for use in the ALICE Photon Spectrometer [60]. Figure 2.12 shows a crystal. The north MPC is made up of 220 towers, and the south is slightly smaller lacking the innermost ring of instrumented towers and containing only 196 towers. Figure 2.12 shows the detector tower arrangement (for the north MPC).

The clustering algorithm follows that of the central arm electromagnetic calorimeter [61] customized for the MPC [62]. A cluster is defined by a group of neighboring towers each with energy above 10 MeV. However, a cluster is not allowed to grow to the point at which it has more than one local maximum defined as the highest energy within a 3×3 grid centered around the tower in question. The center of gravity of the cluster is calculated by weighting each tower's position by the log of the energy fraction that tower has. The calculation of the cluster energy is restricted to towers that have greater than 2% of the total energy.

We can usefully quantify the shower shape with two variables: dispersion

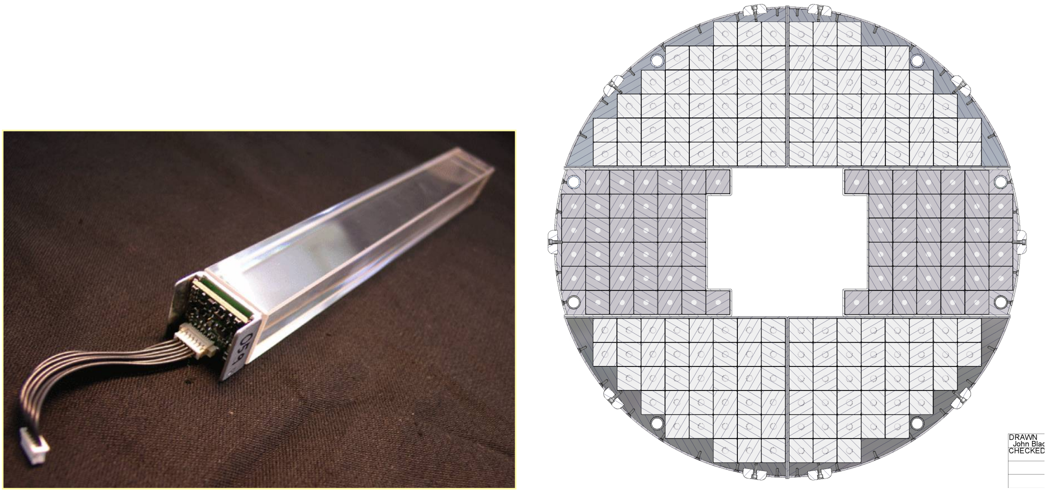

Figure 2.12: A photograph of one of the $PbWO_4$ crystal on the left and a schematic of the tower arrangement (North MPC) on the right.

and χ^2. The dispersion is independent of any predicted shower shape and is defined (for x but similarly for y) as:

$$disp_x = \frac{\sum_i E_i (x_i - \bar{x})^2}{\sum_i E_i} \tag{2.3}$$

The χ^2 variable is based on comparing the measured shower shape with an expected shape, it is defined as:

$$\chi^2 = \sum_i \frac{(E_i^{predicted} - E_i^{measured})^2}{\sigma_i^2} \tag{2.4}$$

where i is an index over the towers within the shower. The χ^2 thus takes into account both the predicted shower shape, $E_i^{predicted}$, and fluctuations, σ. The predicted shower shape and fluctuations are based on a log weighted center of gravity and parameterized as a function of the cluster energy.

Part II

Run 3

Chapter 3

Run 3 Data Analysis

This chapter describes the unidentified charged hadron analysis in the Run 3 d+Au data. The data was recorded by PHENIX in the 2003 RHIC run. The work described in this and the following chapter is published in [63].

3.1 Overview

In the early Au+Au runs at RHIC we observed many intriguing hints of formation of a QGP. Amongst them was the exciting observation of strong suppression of the yield of hadrons with p_T above ~ 2 GeV/c in mid-central and central Au+Au collisions relative to the corresponding yield in p+p collisions scaled by the sum of independent nucleon-nucleon collisions in Au+Au interactions [64, 65, 14]. The hadron spectrum in Au+Au is sensitive to final state effects including jet quenching, parton recombination, and scattering of produced particles thus providing a suitable tool to investigate the QGP and its formation. However, it is also sensitive to initial state effects such as the Cronin effect, nuclear shadowing and gluon saturation (see section 1.2.2). To disentangle the initial from the final state effects as well as to study them on their own merit, in its third run RHIC collided deuteron and gold nuclei.

As there is no dense medium created in them, d+Au collisions are an effective control experiment to observe the effect of the initial state on the hadron spectrum. In this analysis we study the charged hadron spectrum to high p_T and in different centrality selections.

The deuteron is a large system with a mean proton–neutron distance of about 3 fm, and a significant probability to be larger; we use a Hulthén form

[66] to describe the deuteron wave function[1]:

$$\phi_d(r_{pn}) = \left(\frac{\alpha\beta(\alpha+\beta)}{2\pi(\alpha-\beta)^2}\right)^{\frac{1}{2}} \frac{e^{-\alpha r_{pn}} - e^{-\beta r_{pn}}}{r_{pn}} \tag{3.1}$$

where r_{pn} is the proton–neutron distance and with $\alpha = 0.228$ fm^{-1} and $\beta = 1.18$ fm^{-1}.

The square of equation 3.1 represents the probability distribution for the proton–neutron distance in the deuteron and is shown in Figure 3.1. Because the separation is so large there can be d+Au collisions in which only one of the two nucleons interacts with the Au nucleus. These quasi N+Au events can be classified by measuring the uninteracted spectator nucleon in PHENIX's far forward detectors, the ZDC and FCAL. The N+Au "tagged" subset of d+Au collisions allows us further insight into the collision geometry and nuclear effects.

3.2 Event Selection and Centrality Definitions

The present analysis is based on minimum bias events, defined by a coincidence of at least one photomultiplier each in the north and south BBCs. The data were taken for events with vertex position within $|z| < 30\,\mathrm{cm}$ along the beam axis. A total of 6.2×10^7 events were analyzed, which corresponds to 1.6 nb^{-1} of total integrated luminosity. At this vertex cut the minimum bias trigger cross section measured by BBC is 1.99 b ± 5.2% [67] . Thus at the trigger efficiency of 88.5% ±4% (see below) we get the total inelastic d+Au cross section of 2.26 ± 0.1 b.

3.2.1 PHENIX Glauber Model in d+Au

The PHENIX Glauber model of d+Au collisions is a geometric description of the collision used to calculate global parameters of the event. The deuteron is described using the Hulth$\acute{e}$n wave function as shown in equation 3.1 above. The Au nucleus is made of 79 protons and 118 neutrons; their distribution is represented by a Woods-Saxon density function:

$$\rho(r) = \frac{\rho_0}{1+e^{\frac{r-R}{a}}} \tag{3.2}$$

---

[1] Note that subsequent to this analysis a more modern description of the deuteron was used in calculations and found to agree well with the Hulth$\acute{e}$n description, see section 5.2.1.

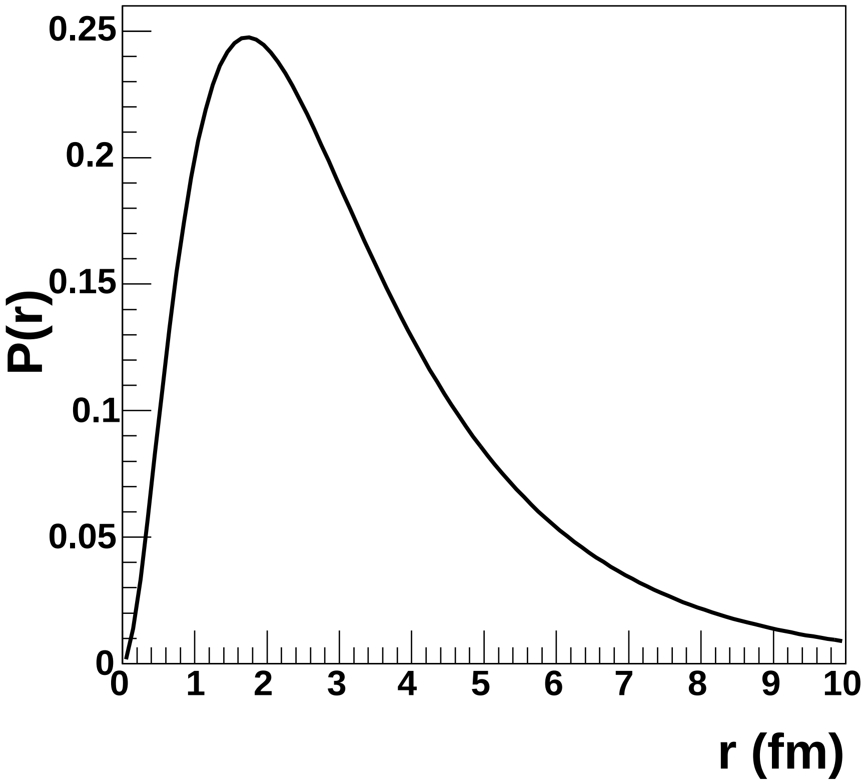

Figure 3.1: Probability distribution for the proton − neutron distance in the deuteron given by the square of the Hulth$\acute{e}$n wave function.

with the radius R = 6.38 fm, and the diffuseness a = 0.54 fm. To extract the relevant event parameters a Monte Carlo method is used in which the two nuclei are given position by sampling the respective density distributions and then an impact parameter, b, for the collision is chosen randomly.

From this procedure we calculate the mean number of participating nucleons <N$_{part}$ >, mean number of binary collisions $\langle N_{coll} \rangle$, the nuclear overlap function T_{AB}, and the mean number of collisions per deuteron participating nucleon, ν. The nuclear overlap function T_{AB} is defined as:

$$T_{AB}(b) = \int d^2\,\vec{s}\,T_A(\vec{s})\,T_B(|\vec{b} - \vec{s}|), \tag{3.3}$$

where the integration is performed over the element of overlapping area $d^2\,\vec{s}$, ($\vec{s} = (x,\, y)$ is a vector in the transverse plane of interacting nuclei at the impact parameter $\vec{b}$ between the centers of the nuclei). For nucleus A the nuclear thickness function $T_A(b)$ is defined as:

$$T_A(b) = \int dz\, \rho_A(b, z). \tag{3.4}$$

Normalization of $T_{AB}(b)$ is done by integration over all impact parameters:

$$\int d^2\, b\, T_{AB}(b) = A\, B. \tag{3.5}$$

The average number of binary inelastic nucleon–nucleon collisions at impact parameter b can be calculated from $T_{AB}(b)$ as:

$$\langle N_{coll} \rangle = \sigma_{NN}\, T_{AB}(b), \tag{3.6}$$

where σ_{NN} is the inelastic nucleon–nucleon cross section.

3.2.2 Centrality Definitions in d+Au

Centrality classes are defined by the charged particle multiplicity in the Au going (South) side BBC. This is based on the premise that the number of charged particles firing the BBC South is linearly proportional to the mean number of participants from the Au nucleus involved in the collision. To demonstrate this proportionality the BBC South response was simulated as a superposition of independent N_{targ} nucleon-nucleon type reactions, where N_{targ} is the number of participating nucleons in the struck gold nucleus. N_{targ} was calculated using a Glauber model. To connect the BBC hit distribution to the Glauber model the distribution is assumed to follow a negative binomial distribution (NBD):

$$P(n, \mu, k) = \frac{\Gamma(n+k)}{\Gamma(k)n!} \frac{(\mu/k)^n}{(1+\mu/k)^{n+k}} \tag{3.7}$$

In a Glauber event $\mathrm{N}_{\mathrm{part}}^{Au}$ and $\mathrm{N}_{\mathrm{coll}}$ are calculated for a given impact parameter. A simulated BBC hit distribution is then created by taking the Glauber $\mathrm{N}_{\mathrm{part}}^{Au}$ value and creating an NBD with parameters $\mu \times \mathrm{N}_{\mathrm{part}}^{Au}$ and $k \times \mathrm{N}_{\mathrm{part}}^{Au}$. The values for μ and k are determined by fitting the simulated NBD to the real data. The resulting distribution for minimum bias events is plotted in Figure 3.2 together with the experimental data. The overall trigger efficiency

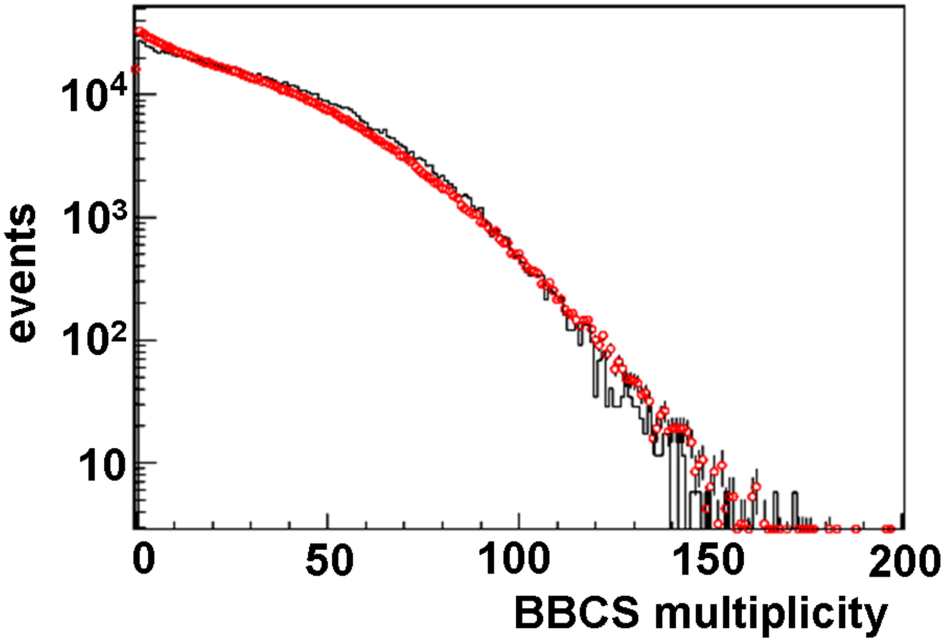

Figure 3.2: Comparison between the experimental data hit distribution in BBC South in d+Au collisions (open circles) and the calculated BBCS hit distribution (solid line).

is calculated by comparing the data to the simulated BBC hits distribution, and is found to be 88.5% ±4%.

Considering this overall efficiency the BBC hit distribution is divided into 88 bins such that each bin spans a different range in the number of BBC hits but contains the same number of events, thereby allowing us to assign a centrality percentage to each event bin. The bins are put together to create four larger centrality bins A, B, C and D. These regions were selected to define in d+Au collisions four centrality classes 0–20%, 20–40%, 40–60%, and 60–88%, respectively (see Figure 3.3).

3.2.3 Identifying and Classifying N+Au Collisions

A p+Au collision event is tagged by detection of a spectator neutron in the ZDC on the deuteron going (North) side (ZDCN). Similarly, we use the FCAL

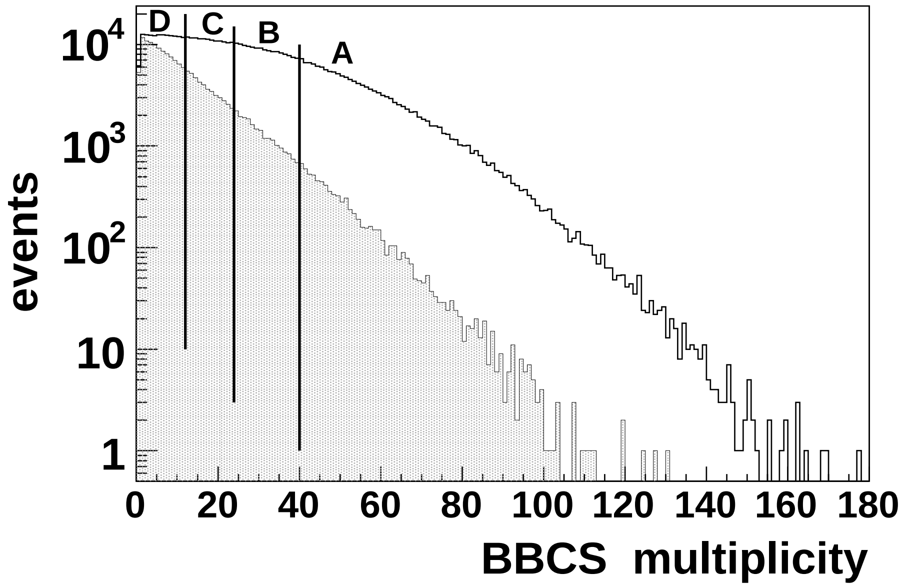

Figure 3.3: The multiplicity distribution in BBC South, located on the gold nucleus fragmentation side. Four centrality classes for d+Au collisions are defined by slicing the BBCS distribution, shown with vertical lines. The same multiplicity cuts were used for the tagged sample of p+Au and n+Au events, the summed distribution of which is shown in the lower shaded histogram.

on the deuteron going side (FCALN) to detect a spectator proton and thereby tag n+Au collision events. The scatter plot in Fig. 3.4 shows the ZDCN and FCALN signals, and has three distinct regions. Region 1 is defined as small or no signal in both the ZDCN and FCALN, which corresponds to the case when both nucleons from deuteron interact with the Au nucleus. Region 2 has a small signal in the ZDCN and about 100 GeV amplitude signal in the FCALN. This corresponds to tagged n+Au collisions. Region 3 has a small signal in the FCALN and about 100 GeV energy release in the ZDCN. Events in this region are tagged p+Au events. With the tagged N+Au sample thus defined, we subdivide it into four centrality categories following the definitions of the d+Au centrality classifications, i.e. although the tagged N+Au sample has a different BBC multiplicity distribution than the d+Au supersample the centrality categorization criteria is the same as shown in Figure 3.3. In the left side of Figure 3.5, we present the calculated impact parameter, b, distributions

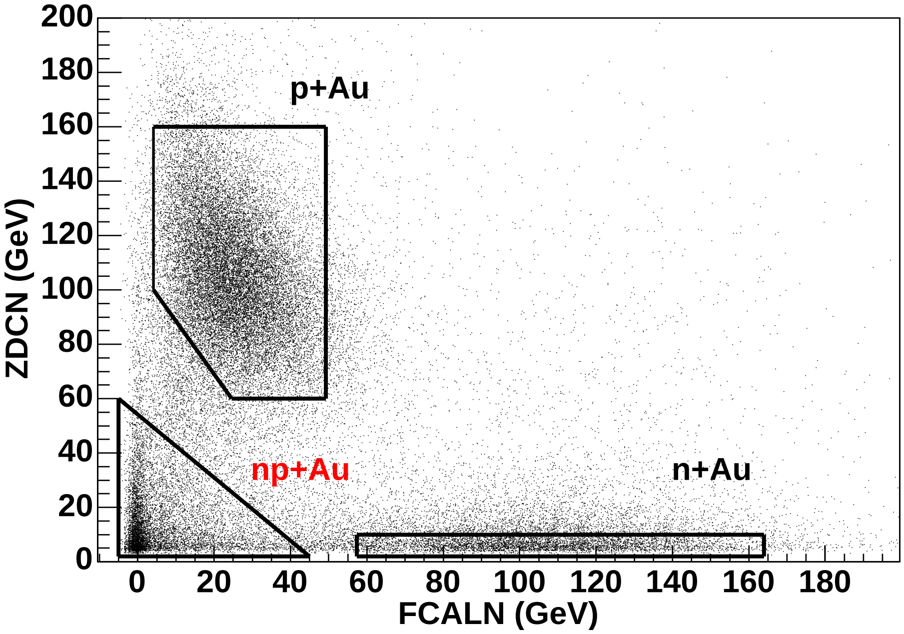

Figure 3.4: Scatter plot of ZDC North (vertical axis) and FCAL North (horizontal axis) signals on the deuteron going side. Solid lines show cuts which define the p+Au and n+Au collisions.

of d+Au collisions and the tagged N+Au sample. The impact parameter is defined as the distance between the centers of the colliding nuclei, Au and d. In the right side of Figure 3.5 the corresponding distributions of the number of collisions per participant nucleon from the interacting deuteron, ν, are plotted. The parameter ν is comparable to the number of collisions suffered by the proton in p+A experiments. Figure 3.5 shows that the tagged sample distribution probes dominantly the outer region of the gold nucleus corresponding to interactions with few subsequent binary collisions.

In Region 3, there is a small (anti) correlation between the ZDCN and FCALN. The reason for this is the close proximity of the FCALN to the ZDCN, and so the ZDCN effectively acts as a secondary target for 100 GeV spectator neutrons, and there is some contamination of secondary particles produced in the ZDCN into the large volume FCALN. To assess the impact of the contamination on the particle spectra, we first quantify the purity of the tagged sample.

Figure 3.6 shows the ZDCN energy spectrum for most central events (cen-

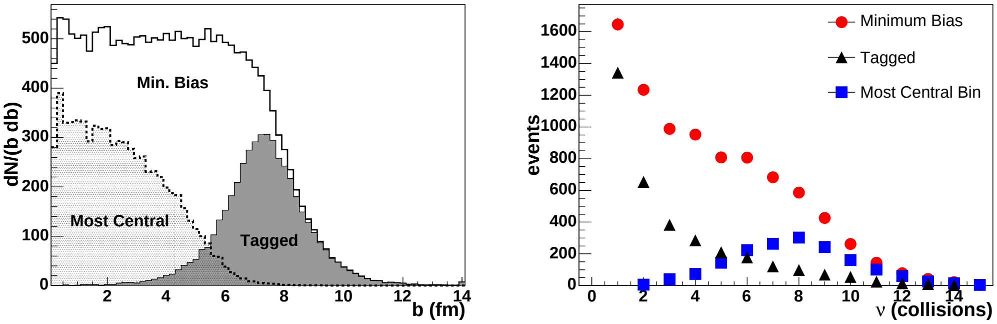

Figure 3.5: On the left, impact parameter distribution for the minimum bias d+Au collisions, for the most central events (centrality bin A) and for the tagged sample. For tagged events the impact parameter was defined from the center of the deuteron. On the right, the corresponding distribution of the number of collisions per participant nucleon from deuteron, ν.

trality A as defined above). To estimate the background contamination we fit the spectrum to a falling exponential for the background and a gaussian for the spectator nucleon signal; their sum well describes the observed spectrum as shown in the figure. The background is thus taken to be the contribution of the exponential beyond the tagging cut threshold, and is 2.8% for most central events and less for more peripheral events.

The left side of Figure 3.7 shows the FCALN energy spectrum for most central events with the same conventions as Figure 3.6. Using the same methods as described above for the ZDCN tagging contamination the contamination of the n+Au in the most central events results in a background estimated at 0.4%. However, the decomposition of the spectrum into an exponential and gaussian fails as we look in more peripheral events, as shown in the FCALN energy spectrum for most peripheral events on the right side of Figure 3.7 where the sum of the two functional forms overshoots the data significantly indicating that the exponential fit overestimates the background. To sidestep this problem we consider the effect of contamination in tagging on the observable of interest - the charged particle spectra. To do so, we define for a given FCALN energy the stability of the spectrum, S, as the ratio of the number of charged particles per event with p_{T}>0.5 GeV/c in the FCALN energy bin to the number of charged particles per event in a reference FCALN energy bin with the best signal to background ratio. We take for the reference bin 80<$\mathrm{E}_{\mathrm{FCALN}}$<120 GeV/$c$. Figure 3.8 shows this quantity for different FCALN

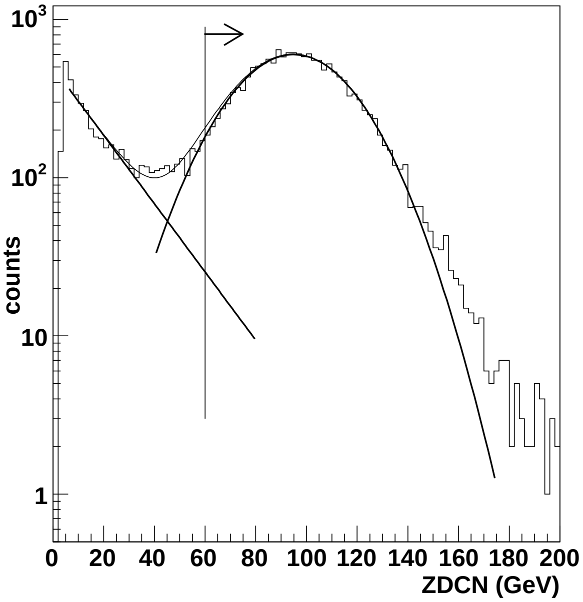

Figure 3.6: The ZDCN energy spectrum. The spectator nucleon is fit to a gaussian and the background to an exponential, their sum is shown in the thin line, and the tagging cut threshold is marked with the vertical line and arrow.

energy selections, and shows that the variation even in the lower energy bins where the background contamination grows is small. We estimate that the effect on the spectra of the background contamination is at worst sub 2% for the FCALN tagged n+Au sample. To further confirm the stability of the two tagged samples, n+Au and p+Au, we directly compare their charged particle spectra. Figures 3.9 and 3.10 show the ratio of n+Au and p+Au spectra (see section 3.3 for description of the measurement of the spectra). In Figure 3.9 we examine central collisions from earlier and later in the run separately because of the concern that as the beam intensity increased over the course of the run contamination may have increased with it. Figure 3.10 shows the ratio over the whole run from most central and most peripheral collsions. As expected the ratio is unity in all cases and gives us confidence to combine the two samples into a single tagged N+Au sample.

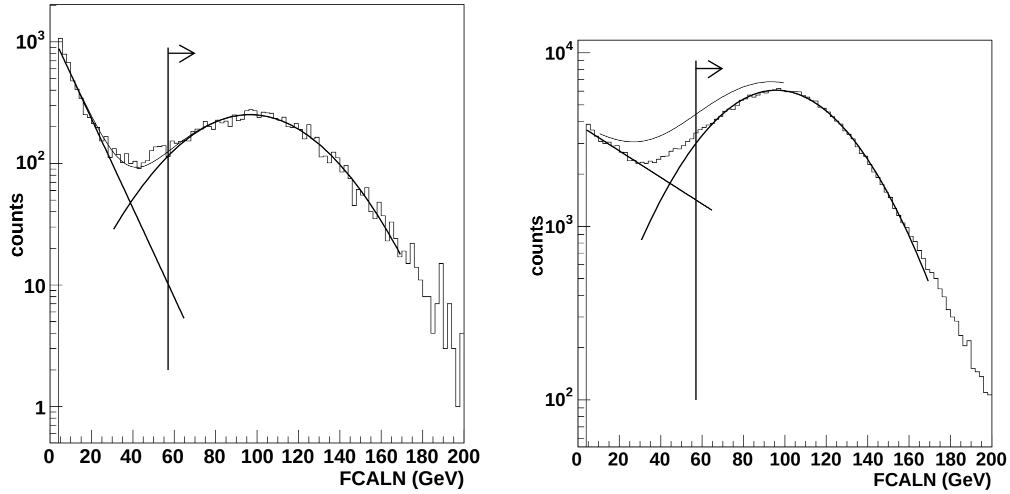

Figure 3.7: The FCALN energy spectrum of most central events on the left, and most peripheral events on the right. The plotting conventions are the same as in figure 3.6.

3.2.4 BBC Correction

A correction factor must be applied to the charged particle spectra reflecting biases in the BBC response and consequent distortions in the centrality classifications. Due to natural statistical fluctuations in the number of particles produced in collisions even for the same impact parameter, the BBC centrality selections necessarily have some finite resolution. Considering the fairly steeply falling BBC multiplicity spectrum, especially in the tagged sample, as shown in Figure 3.3, more peripheral events will be mischaracterized as more central events across the thresholds we set to define the centrality bins. This leads the actual <$\mathrm{N}_{\mathrm{coll}}$>, and with it the number of produced charged particles within a given centrality bin, to be effectively lower than the ideal calculated case.

A competing effect which produces a distortion in the opposite direction arises from the requirement of a BBC coincidence for (even) the minimally biased trigger. For the inelastic nucleon-nucleon cross section we use σ_{NN} = 42 mb, but this is a sum of three distinct processes with non-identical probabilities to fire the BBC trigger: 28 mb for non-diffractive collisions, 10 mb for single diffractive collsions, and 4mb for double diffractive collsions. These different processes have BBC trigger efficiencies of 72 ± 1%, 7 ± 1%, and 32 ±

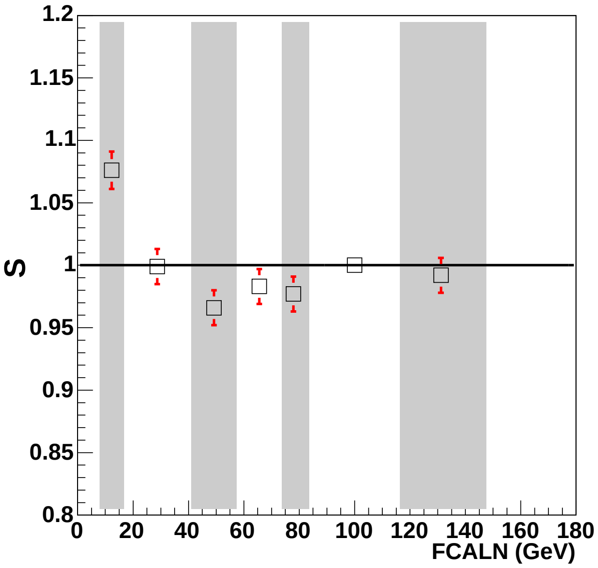

Figure 3.8: The stability quantity, S, for different FCALN energy bins.

1% respectively [68]. Diffractive collisions, both single and double, have lower efficiency because they produce particles predominantly near the beam rapidity and therefore have a small probability for particle production in the BBC acceptance of 3.0< $|\eta| < 3.9$, and an even smaller probability at mid-rapidity. Consequently, the BBC requirement biases the minimum bias trigger towards non-diffractive collisions with larger mid-rapidity particle production, and this leads to a centrality bias because as the number of nucleon-nucleon collisions increases the probability that at least one was non-diffractive approaches unity. So in the more central events, in which $<N_{\text{coll}}>$, is higher the bias becomes negligible whereas it is present in more peripheral events.

The correction factors are calculated by a Monte Carlo procedure, in which the BBC's response to a d+Au collision is modeled as described above. Events generated in the PHENIX Glauber Monte Carlo are taken on an event by event basis and for the particular event the BBC response as a trigger is probabilistically sampled. For the tagged N+Au sample, the Glauber input is restricted to events in which only one of the deuteron's nucleons interacted with the Au nucleus.

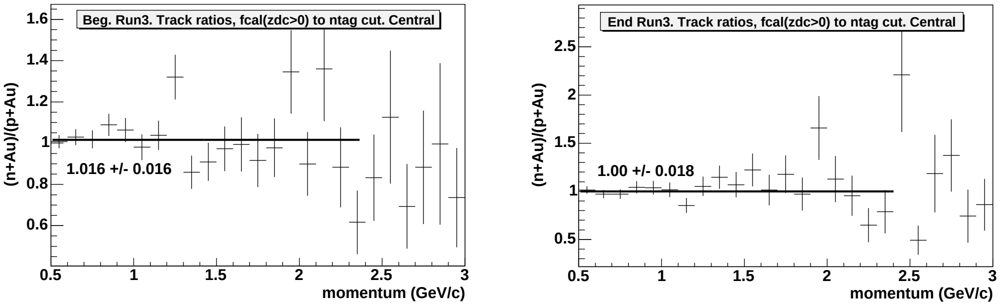

Figure 3.9: On the left the ratio of the n+Au to p+Au charged particle spectra in most central events for collisions from the start of the run, and on the right the same quantity from the end of the run. A flat line fit to the ratio is shown as well.

3.2.5 Summary

The relevant centrality parameters are listed in Table 3.1.

Cent. bin	$\langle N_{part}\rangle$	$\langle N_{coll}\rangle$	$\langle T_{AB}\rangle$, mb^{-1}	ν	C_{BBC}
A	15.6±0.9	15.37±1.0	0.357±0.0238	7.5±0.5	0.95±0.029
B	11.1±0.6	10.63±0.7	0.248±0.0095	5.6±0.4	0.99±0.007
C	7.7±0.4	6.95±0.6	0.164±0.0143	4.0±0.3	1.03±0.009
D	4.2±0.3	3.07±0.3	0.0762±0.0071	2.2±0.2	1.04±0.027
tag A	10.6±0.7	9.6±0.7	0.229±0.0167	9.6±0.7	0.93±0.029
tag B	8.0±0.6	7.0±0.6	0.167±0.0143	7.0±0.6	0.95±0.019
tag C	5.6±0.3	4.6 ±0.3	0.109±0.0071	4.6±0.3	0.95±0.015
tag D	3.1±0.2	2.1±0.2	0.05±0.0048	2.1±0.2	0.97±0.035

Table 3.1: Total number of participants N_{part}, number of collisions N_{coll}, nuclear overlap function T_{AB}, see equation 3.3, average number of collisions per participant nucleon from deuteron ν, and the BBC bin correction factor for different centrality classes.

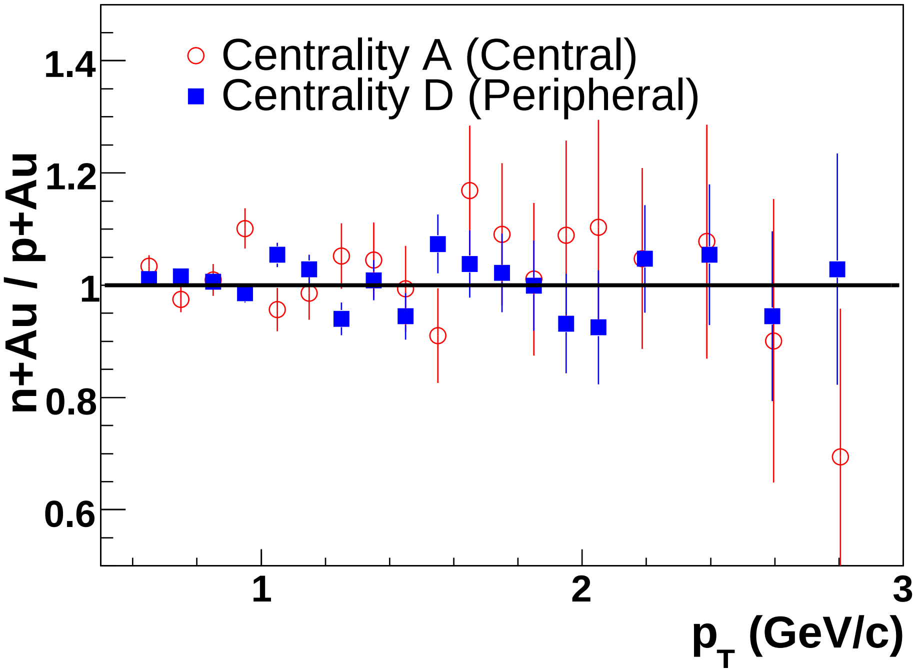

Figure 3.10: The ratio of the n+Au to p+Au charged particle spectra in most central and most peripheral events.

3.3 Charged Hadron Analysis

Following the global analysis decisions described in the previous section we measure the invariant hadron yield in each event class. To do so we must carefully identify and rid the analysis of multiple background sources.

We define a charged particle track as one in which both X1 and X2 sections were used with a unique U and V wire hit in the DC, as well as at least a favored PC1 hit (see section 2.4 above for details). Further we make a fiducial cut at 40 cm in the z direction.

The majority of background tracks are particles with low momenta, which in traveling from DC to PC3 undergo multiple scattering and are additionally deflected in the residual magnetic field behind the DC. To minimize this background we employ a track matching cut in the PC3 that rejects tracks whose displacement in the ϕ or z direction, D_ϕ and D_z respectively, is greater than 2.5 standard deviations. In addition we exclude events in which the z vertex determined by the BBC is outside of 30 cm from the nominal interaction point.

Despite these veto cuts, there is still significant background contamination for p_T above 4 GeV/c which must be subtracted. The main sources of the remaining background are e^+e^- pairs from photon conversions in the material between the collision vertex and the drift chamber, and secondary particles produced by hadron decays. To distinguish these backgrounds we use the RICH detector to divide all tracks into two subsets: tracks with an associated RICH signal, N_R, and tracks with no signal in the RICH, N_{NR}. Tracks with at least one hit in the RICH contain high p_T pions and conversion electrons. For reconstructed electrons with momentum above 150 MeV/c, the average number of photomultiplier tube (PMT) hits in the RICH associated with the track is $\langle N_{PMT}\rangle \approx 4.5$.

3.3.1 Conversion Electron Background

The RICH detects more than 99% of all conversion electrons for $N_{PMT} \geq 1$. At this threshold the RICH also detects pions with $p_\mathrm{T} \geq$ 4.8 GeV/c, but the number of associated PMTs for pions reaches its asymptotic value well above 10 GeV/c; for a 10 GeV/c pion $\langle N_{PMT}\rangle = 3.6$. Therefore we label tracks with $N_{PMT} \geq 5$ as electron tracks, N_e, which compose some fraction, R_e, of conversion electrons. To calculate this fraction we take advantage of the deflection of conversion electrons in the magnetic field between the DC and PC3. This deflection leads to poor track matching in PC3 which distinguishes electrons from true high p_T pions. We define poor PC3 track matching as a displacement of more than four standard deviations in the ϕ direction. Thus

Centrality	All	A	B	C	D
R_e	0.41 ± 0.01	0.42 ± 0.02	0.40 ± 0.02	0.41 ± 0.02	0.38 ± 0.02
R_e (tagged)	0.36 ± 0.03	0.37 ± 0.08	0.33 ± 0.05	0.40 ± 0.05	0.35 ± 0.04

Table 3.2: The measured values of R_e.

we measure the value of R_e as the fraction of N_R with $4\sigma < |D_\phi| < 10\sigma$. The values of R_e for in the general d+Au and tagged samples are shown in Table 3.2.

The real pion signal, S_R, in the N_R sample, is calculated for each p_T bin as:

$$S_R = N_R - \frac{N_e}{R_e} \tag{3.8}$$

The PC3 distribution for the conversion subtraction is shown on the left side of Fig. 3.11. The conversion subtraction is performed independently in each centrality bin. The definition of N_e (tracks with $N_{PMT} \geq 5$) does not perfectly select electron tracks, as some fraction of pions satisfies the cut. This leads to a fraction of authentic pions, which have $N_{PMT} \geq 5$, being subtracted along with the conversion electrons. This fraction is small below 7 GeV/c, but increases rapidly for higher p_T. We calculate a correction factor to address this over-subtraction, using a Monte Carlo simulation of the detector. The uncertainty associated with this correction, $\delta_{\pi loss}$, is shown in Table 3.5.

3.3.2 Hadron Decay Background

The hadron decay background is of two types: "decay" and "feed down". The decay background is produced by π and K decays far from the source and thus with reconstructed momenta different from their true momenta, whereas the feed-down background is produced by weak decays of short lived particles, mostly K_s^0 and Λ particles near the event vertex with apparent momenta close to their true momenta.

Decay

From tracks with no RICH signal, the N_{NR} sample, we define a sub-sample by selecting tracks with p_T >10.5 GeV/c, a p_T region which is almost exclusively background. We expect that its shape in D_ϕ will be the same as the background in the lower p_T region. Within this sub-sample we calculate the ratio, R_{decay}, of tracks which pass the PC3 cut ($|D_\phi| < 2.5\sigma$) to those with a poor match ($4\sigma < |D_\phi| < 10\sigma$). The values of R_{decay} for in the general

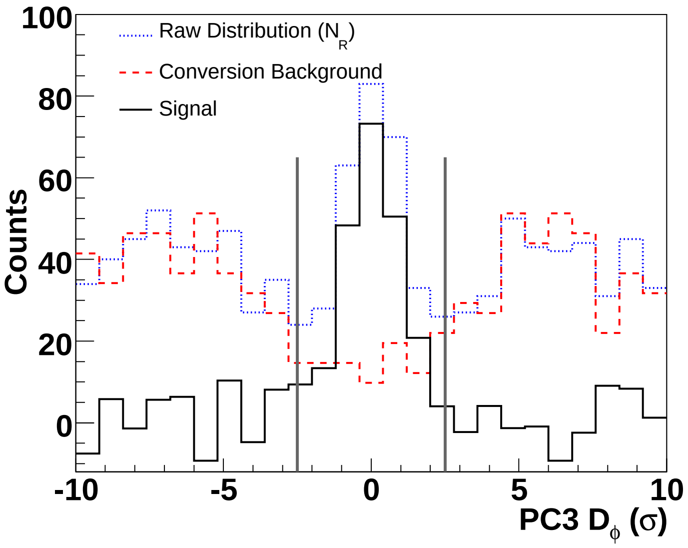

Figure 3.11: The PC3 D_ϕ distributions for the conversion subtraction shown for minimum bias with $6 < p_T < 7$ GeV/c. The raw distribution, N_R is shown with the dotted line. The estimated conversion background shown with a dashed line is N_e/R_e. The signal is the raw minus the estimated background distribution. The vertical bars show the track matching cuts at ± 2.5 D_ϕ.

Centrality	All	A	B	C	D
R_{decay}	0.55 ± 0.03	0.57 ± 0.04	0.57 ± 0.06	0.57 ± 0.07	0.42 ± 0.06
R_{decay} (tagged)	0.51 ± 0.07	0.57 ± 0.04	0.57 ± 0.06	0.57 ± 0.07	0.42 ± 0.06

Table 3.3: The measured values of R_{decay}.

d+Au and tagged samples are shown in Table 3.3. For each momentum bin, the total decay background is then obtained by multiplying the N_{NR} tracks with poor PC3 matching ($4\sigma < |D_\phi| < 10\sigma$) by R_{decay}. The PC3 distribution for the decay subtraction is shown on the right side of Fig. 3.12. The decay background as a function of p_{T} is measured and subtracted independently in each centrality bin.

Feed Down

The feed-down subtraction addresses the detected π and p particles that were produced in the decays of K_s^0 and Λ particles, so we define the total

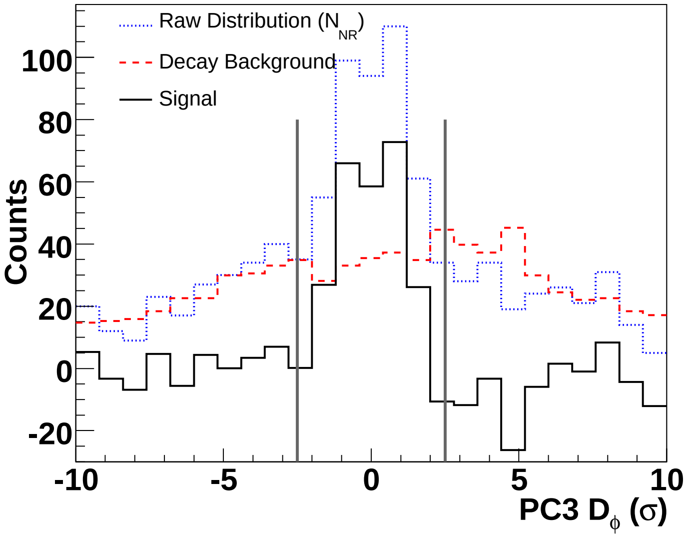

Figure 3.12: The PC3 D_ϕ distributions for the decay subtraction shown for minimum bias with $6 < p_T < 7$ GeV/c. The raw distribution, N_{NR} for the decay is shown with the dotted line. The estimated decay background, shown with a dashed line, was obtained by scaling the PC3 distribution of N_{NR} tracks with $p_T > 10.5$ GeV/c based on the $(4\sigma < |D_\phi| < 10\sigma)$ region. The signal is the raw minus the estimated background distributions. The vertical bars show the track matching cuts at ± 2.5 D_ϕ.

feed-down contamination as:

$$C_{feed} = \frac{(p+\pi)^{feed}}{h^{detected}} \tag{3.9}$$

averaging over charged particle and anti-particle yields. For feed down estimation we have no statistical recourse and must resort to simulation to find the contamination. We assume that the spectral shapes of the K_s^0 and Λ follow the shapes of the charged kaon and proton spectra, respectively. There is good agreement of Monte Carlo simulations in d+Au [69] and minimum bias Au+Au [14] for proton feed down as shown in Figure 3.13. We therefore use the Au+Au Monte Carlo simulation, which also includes K_s^0 to pion processes, to obtain the ratio $(p+\pi)^{feed}/(p+K)^{detected} = 0.2$, after the decay background subtraction as shown in Figure 3.14.

To make use of this ratio we rewrite the contamination as:

$$C_{feed} = \frac{(p+\pi)^{feed}}{(p+K)^{detected}} \times \frac{(p+K)^{detected}}{h^{detected}} \tag{3.10}$$

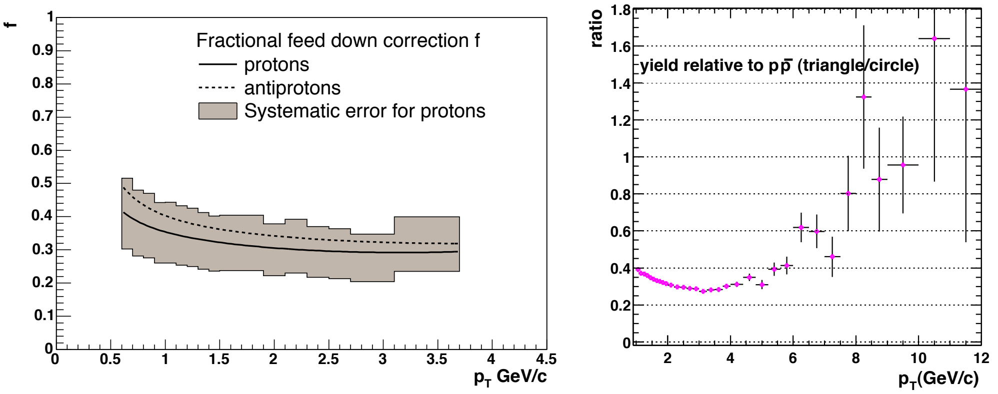

Figure 3.13: Both plots show the ratio $\mathrm{p}^{feed}/\mathrm{p}^{detected}$ from simulation. On the left is the result in d+Au from [69] figure 3 and on the right minimum bias Au+Au from [70] Figure 4.35.

To find the contamination we use the fraction of $p+K$ particles in our measured hadron sample. To do so, for p_T less than 2.5 GeV/c we use the PHENIX published data on identified hadron production in d+Au [69]. We explicitly calculate the $(p+K)^{detected}/h^{detected}$ ratio from that data. At higher p_{T}, assuming π^0 has the same yield as $\pi^{\pm}$, we subdivide this ratio as:

$$\frac{p+K}{h} = \frac{p+K}{\pi} \times \frac{\pi}{h} = \left(\frac{p}{\pi} + \frac{K}{\pi^0}\right) \times \frac{\pi^0}{h} \tag{3.11}$$

so that the right-hand side consists of all measured quantities. The p/π ratio is taken from STAR measurements [72] scaled to match the PHENIX data [69] in their common p_{T} region, as shown in Figure 3.15. The discrepancy between STAR and PHENIX is at least partially explained by the feed down contribution to the STAR protons. The K/π^0 ratio is calculated from [73] and [74], shown together in Figure 3.16. The ratio of π^0s to hadrons is calculated from the charged hadron measurement of this analysis and π^0 measurements in [73] (this ratio is shown in the following chapter, Figure 4.5). From both the low and high p_{T} regions C_{feed} is calculated to be 9.6%. To this factor we assign a 50% systematic uncertainty based on uncertainty of the various particle ratios and the Monte Carlo simulation. C_{feed} is shown in Fig. 3.17. We correct for the effects of feed-down decay by multiplying the spectra remaining after the conversion and decay subtraction by $1 - C_{feed}$.

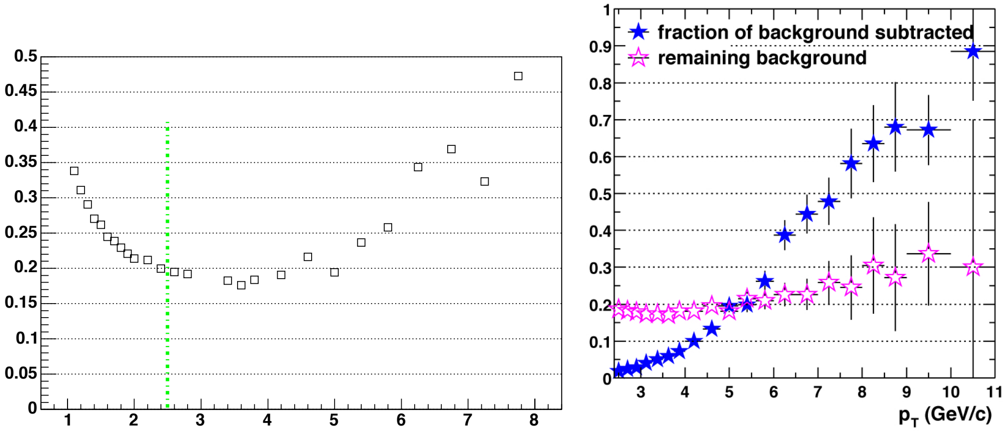

Figure 3.14: The ratio (p+π)^{fromfeed}/(p+k) from simulation. On the left the ratio used for p_{T} <2.5 GeV/c from [71] Figure 62 and on the right shown in pink the ratio used for p_{T} <2.5 GeV/c from [70] Figure 4.43. The ratio on the right stays flat at 0.2 rather than rising like that shown on the left because it takes into account the particles already subtracted in the decay subtraction. The blue points on the right show this decay subtraction as a fraction of the conversion subtracted yield.

3.3.3 Spectra Normalization

Following the background subtraction, we have constructed a single, p_{T} dependent correction function to correct the hadron spectra for acceptance, decay in flight, reconstruction efficiency, and momentum resolution. The correction is determined by using a Monte Carlo simulation of the PHENIX detector. The correction function is necessarily particle species dependent to take into account multiple scattering and decays, therefore we calculate separate correction functions for π^+, π^-, K^+, K^-, p^+, and p^-. The individual functions are weighted by the particle p_{T} spectra measured in peripheral Au+Au collisions [75] to form a single correction factor, $C_{MC}(p_T)$, subject to a systematic uncertainty, $\delta_{MCweight}$, stemming from uncertainty on the particle mixture [73]. For absolute normalization of the spectra we match the geometrical acceptance of the Monte Carlo simulation with the actual acceptance of the data. To obtain the charged hadron yield we multiply the background subtracted spectra by the correction function.

We normalize each centrality bin by dividing by the number of events, and each momentum bin by dividing by its bin width. Each data point is corrected so its value corresponds to the bin center. This is done based on

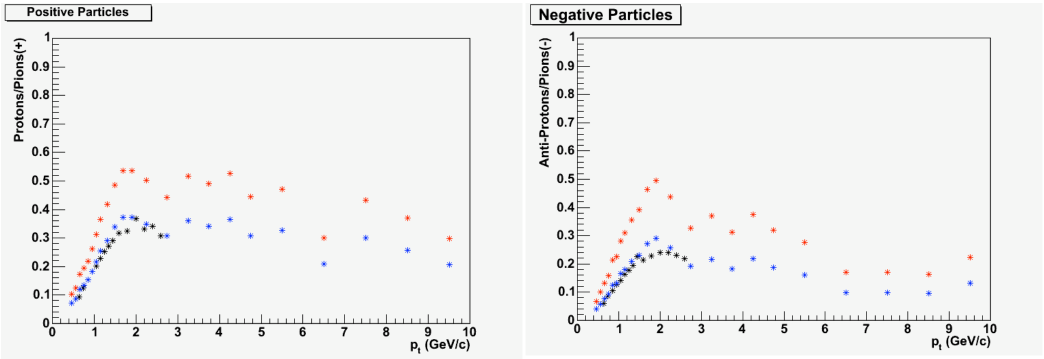

Figure 3.15: The p^+/π^+ ratio on the right and the p^-/π^- ratio on the left. The black points are the PHENIX data from [69] which are used for p_{T} <3 GeV/c. In red are the STAR points from [72], and in blue they are scaled down to match the PHENIX data points.

the local spectral shape: we fit the spectra to a modified power law, and then scale the yield appropriately to reflect the correct yield at the bin center.

The invariant hadron yield is then defined as:

$$\begin{aligned} \frac{1}{N_{evt}} \frac{d^2N}{2\pi p_T dp_T d\eta} &= \left(\frac{d^2N}{2\pi p_T dp_T d\eta}\right)^{bkg-subtracted} \\ &\times \frac{1}{N_{evt}} \times (1 - C_{feed}) \times C_{MC}(p_T) \times C_{BBC} \end{aligned} \tag{3.12}$$

All of the preceding steps are applied to the tagged N+Au (nucleon + gold) sample as well as to the general d+Au sample.

3.3.4 Systematic Uncertainties Summary

We estimate systematic uncertainties on the methods and assumptions of our analysis as displayed in Tables 3.4 and 3.5. Table 3.4 shows uncertainties on the spectra that do not vary with p_{T}, and Table 3.5 shows uncertainties that vary with p_T.

3.3.5 Nuclear Modification Factor and p+p Data

To further examine the d+Au and N+Au charged hadron spectra we may compare them to the similar quantity from p+p collisions. To do so we use the nuclear modification factor R_{AB}. For any collision of nuclei $A+B$, R_{AB} is

Source	Uncertainty(%)
Geometric Acceptance Correction	2.9
Track Matching	2.2
Run By Run Variation	5
Feed-Down Correction	4.8
$\delta_{MCweight}$	3.7
Total	8.7

Table 3.4: Systematic uncertainties that are constant for all p_{T}.

p_T GeV/c	Momentum Resolution (%)	Momentum Scale (%)	Background Subtraction (%)	$\delta_{\pi loss}$ (%)	Total(%)
<4.5	<0.5	<3.2	<0.1	<0.3	<3.3
4.5-5.5	<0.6	3.3	0.5	0.5	3.4
5.5-6.5	0.8	3.5	1.4	1.1	4.0
6.5-7.5	1.0	3.6	2.0	3.6	5.6
7.5-8.5	1.4	3.7	4.9	6.9	9.3
8.5-9.5	1.8	3.8	11.9	13.9	18.8

Table 3.5: Systematic uncertainties that vary with p_{T}. Background subtraction uncertainties refer to the 0–88% d+Au spectra; the uncertainties are greater in the more peripheral d+Au and more central N+Au spectra.

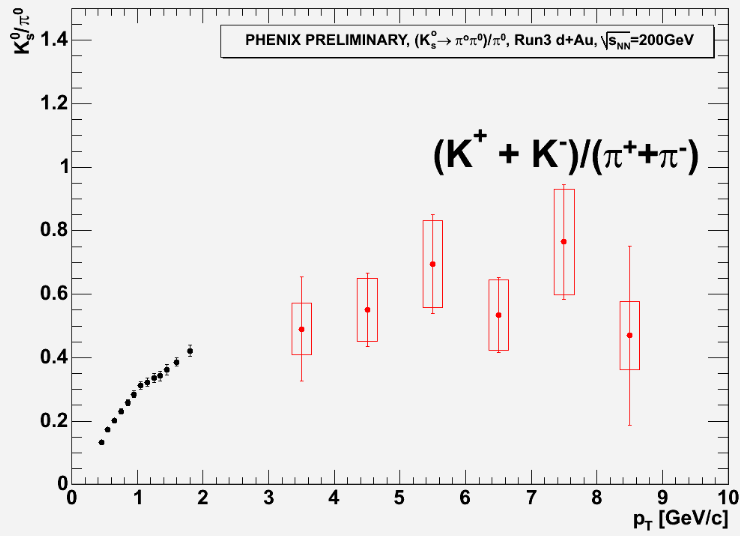

Figure 3.16: The K/π^0 ratio at high p_{T} and at low p_{T} the $K^{\pm}/\pi^{\pm}$ ratio from [74], Figure 5.2.3.

calculated for each centrality class as the ratio of the yield in $A+B$ collision to the cross section in $p+p$ collisions scaled by the nuclear overlap function $\langle T_{AB} \rangle$:

$$R_{AB}(p_T) = \frac{(1/N_{evt})\ d^2N^{A+B}/dp_T d\eta}{\langle T_{AB} \rangle\ d^2\sigma^{p+p}/dp_T d\eta}. \tag{3.13}$$

$\langle T_{AB} \rangle$ is determined by the density distribution in the nuclei A and B and is averaged over the impact parameter range within a particular centrality class. In our case, nucleus A refers to the deuteron (or the single nucleon in tagged events), and nucleus B refers to the gold nucleus. Using the PHENIX $p+p$ cross section from [76], shown in Figure 3.18, we calculate R_{dAu} and R_{NAu}. The $p+p$ reference spectrum contributes an uncertainty that ranges from 10.7% in the low p_{T} bins to 11.3% at p_{T} >2 GeV/c in R_{dAu} and R_{NAu}.

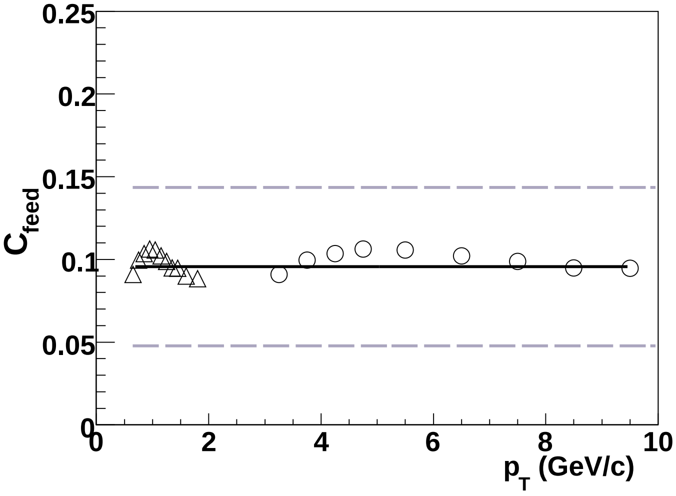

Figure 3.17: Feed-down contamination as the ratio of protons and charged pions from feed-down decays to total detected charged hadrons. The low p_{T} points shown with triangles are calculated using the fraction of $p+K$ particles to hadrons measured in [69]. The higher p_{T} points are calculated using the various ratios of equation 3.11. The solid line is a fit to both sets of points and is used as C_{feed}. It is bracketed by dashed lines showing the assigned 50% systematic uncertainty.

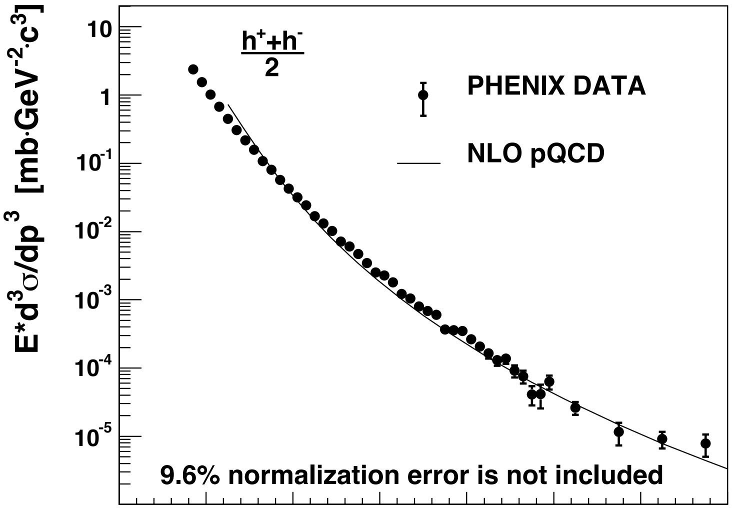

Figure 3.18: The h$^{\pm}$ cross section in p+p collisions from [76].

Chapter 4

Run 3 Results and Discussion

This chapter presents the results of the Run 3 d+Au unidentified charged hadron analysis described in the previous chapter.

4.1 Particle Spectra

The fully corrected p_{T} distributions of $(h^{+} + h^{-})/2$ for d+Au and N+Au collisions for minimum bias and four centrality classes are shown in Figure 4.1. As described above the N+Au spectra are averaged from the p+Au and n+Au spectra, based on the good agreement between the yields of the two tagged samples, as shown in Figure 3.10.

4.2 Nuclear Modification Factors

In Figure 4.2 we present R_{dAu} and R_{NAu}. As expected in the most peripheral bins ($\langle N_{coll} \rangle$ = 2.1, 3.2 for N+Au and d+Au, respectively) the nuclear modification factors are consistent with unity, indicating that peripheral d+Au and N+Au collisions are well described as similar to p+p collisions with a scaled up number of binary collisions. In all centrality bins R_{dAu} and R_{NAu} agree within our experimental uncertainty. This tells us that the physics of the tagged event collisions is similar to general d+Au collisions. In addition because the quantity R_{AB} depends on our Glauber model calculations (in the calculation of $\langle T_{AB} \rangle$, see equation 3.13) suggests that our description of the collision geometry is robust.

Unlike the Au+Au case in which there is significant suppression of the nuclear modification factor, there is enhancement of the nuclear modification factor in d+Au and N+Au. This strongly suggests that the suppression in Au+Au can not be explained as an initial state effect, as if this were the case

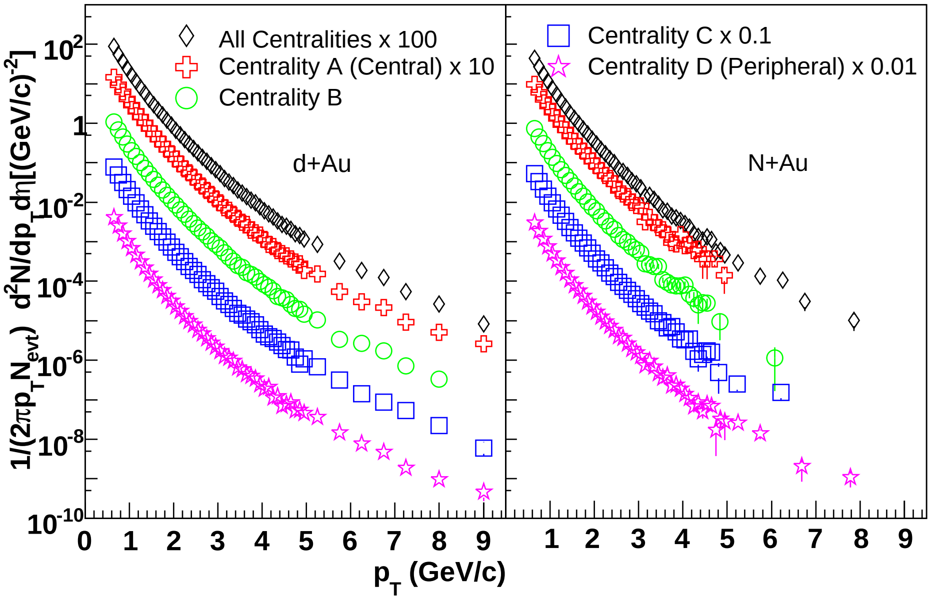

Figure 4.1: The charged hadron spectra for centrality selected d+Au collisions (left panel) and N+Au collisions (right panel). The error bars represent statistical uncertainties only, although they are generally smaller than the data point symbols. Points from different centrality bins are scaled sequentially by a factor of ten. (See Table 3.1 for centrality class definitions.)

we'd expect it to be present in d+Au as well, but rather is a final state effect. In Figure 4.3 the R_{AuAu} points from [14] are overlaid with the R_{dAu} for different centrality bins. Although in terms of the $\langle N_{coll}\rangle$ defined by a centrality bin peripheral Au+Au events are similar to central d+Au events the trends are clearly opposite in Au+Au and d+Au.

The observed enhancement of the hadron yield in d+Au relative to binary collision scaled p+p, is the Cronin effect and has been measured previously in lower energy p+A collisions [23, 77]. The measured R_{dAu} and R_{NAu} are systematically larger than unity in the momentum range between 1.5GeV/c and 5GeV/c reaching a maximum amplitude of around 1.3.

There are many theoretical models with very different assumptions about initial state effects, which describe the Cronin effect [78, 79, 80, 81]. The models generally agree that there is at least one additional scattering of the initial nucleon or parton while propagating though the target nucleus. This scattering increases the intrinsic transverse momentum of the colliding parton, and leads to a broadening of the parton p_{T} distribution. We can parameterize the effect of this broadening by writing the mean value of parton intrinsic momentum k_T as

$$\langle k_T^2 \rangle_{pA} = \langle k_T^2 \rangle_{pp} + \langle k_T^2 \rangle_A, \tag{4.1}$$

where $\langle k_T^2 \rangle_{pp}$ is the square of the initial parton transverse momentum in the proton, $\langle k_T^2 \rangle_A$ is an additional momentum squared after rescattering, and $\langle k_T^2 \rangle_{pA}$ is the final broadened width. Most of the models differ on the assumption they use to describe $\langle k_T^2 \rangle_A$: whether there is a single hard scattering or a sum of small sequential rescatterings which produce the additional k_T.

Common to the models is that $\langle k_T^2 \rangle_A$ is function of the number of sequential nucleon-nucleon collisions, ν. For impact parameter b, $\langle k_T^2 \rangle_A$ can be written as:

$$\langle k_T^2 \rangle_A(b) = H(\nu(b) - 1), \tag{4.2}$$

where H is the square of the average momentum acquired in ν-1 rescatterings. For a single hard scattering model $\langle k_T^2 \rangle_A$ should saturate at ν=2. We therefore investigate the shape of R_{dAu} as a function of ν to illuminate the underlying process. The centrality selection of our data and the tagged N+Au sample allow us to investigate precisely the effect of the collision geometry. We use $\nu = \langle N_{coll}/N_{part}^{deutron} \rangle$ (in N+Au collisions $\nu = \langle N_{coll} \rangle$) to look explicitly at the impact parameter dependence of the nuclear modification factor. The values of ν are presented in Table 3.1.

Three transverse momentum regions were selected to study the dependence of R_{AB} on ν: 2.8$\leq p_{\mathrm{T}} \leq$ 6.0 GeV/c, 1.5$\leq p_{\mathrm{T}} \leq$ 2.7 GeV/c, and 0.6$\leq p_{\mathrm{T}}$ $\leq$ 1.0 GeV/c. In the low p_{T} region we expect scaling with the number of participating nucleons rather than with the number of binary collisions and therefore R_{AB} is less than 1. In Figure 4.4 we plot R_{dAu} and R_{NAu} as a function of $(\nu - 1)$. The Cronin effect is observed in the 2.8$\leq p_{\mathrm{T}} \leq$ 6.0 GeV/c region, where within the limits of our uncertainties it is independent of the number of additional scatterings (ν-1). In the intermediate p_{T} region, the data show little to no Cronin enhancement confirming scaling with the number of binary collisions. Just as $R_{dAu}(p_{\mathrm{T}})$ and $R_{NAu}(p_{\mathrm{T}})$ matched very closely so do $R_{dAu}(\nu)$ and $R_{NAu}(\nu)$.

4.3 Particle Ratios

PHENIX measured identified charged particles at low momentum in [69], as discussed above, and found a larger Cronin enhancement for pions than protons. R_{dAu} for protons reaches about 1.8 at $p_{\mathrm{T}} \approx 3$ GeV/c, whereas pion R_{dAu} is measured to be about 1.1 for transverse momentum between 2 and 2.6 GeV/c. To check the extension of this trend at higher p_{T} we calculate the ratio of the charged hadrons measured in the present analysis to the π^0 spectra from [82], alongside the ratio of $(p^{\pm} + K^{\pm} + \pi^{\pm})/\pi^{\pm}$ from [69]. These ratios are presented in Fig. 4.5.

In the transverse momentum region common to the two presented ratios there is strong agreement between the analyses. The $(h^+ + h^-)/2\pi^0$ ratio is independent of p_{T} above $2\,\mathrm{GeV}/c$ where the identified particle data ends, implying that the R_{dAu} and particle ratio trends observed at low transverse momentum continue at higher transverse momentum. The average value of 1.58 ± 0.03 of the $(h^+ + h^-)/2\pi^0$ ratio for p_{T} above $2\,\mathrm{GeV}/c$ in the peripheral D centrality bin, agrees well with the value of 1.59 obtained from lower energy collisions in the CERN ISR [83]. As found in [64] for Au+Au collisions this value rises for more central events: we find average values of 1.78 ± 0.02, 1.77 ± 0.03, and 1.72 ± 0.03 for centrality bins A, B, and C, respectively. There is an additional 11% systematic uncertainty common to all four values. The centrality dependence implies some moderate modification effects in central $\sqrt{s_{NN}} = 200\,\mathrm{GeV}$ collisions, even in the d+Au system, that increase the production of protons and kaons relative to pions. The PHENIX measurement of particle species dependent R_{dAu} in [69] at lower p_{T} suggests that the increased particle production relative to pions is dominantly proton and not kaon production. This is in keeping with the expectation of larger Cronin enhancement for protons than pions.

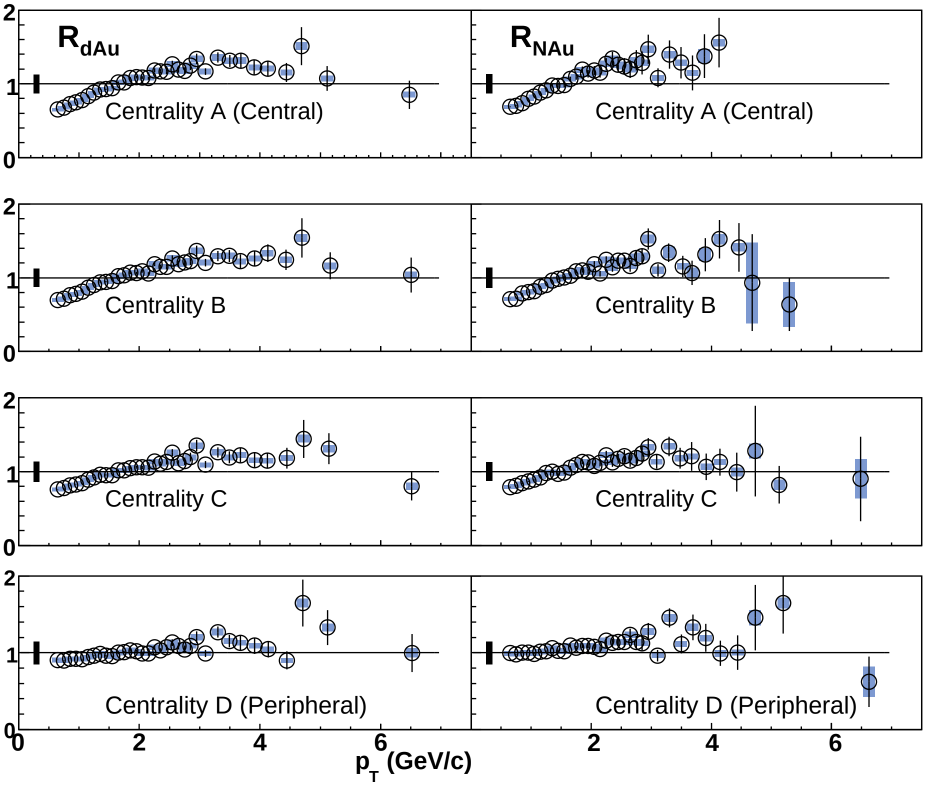

Figure 4.2: On the left R_{dAu}, and on the right R_{NAu} as functions of p_{T}. The bars represent statistical uncertainty (often smaller than the data point symbols), the shaded boxes on each point represent systematic uncertainties that change with p_{T}, and the shaded box on the left systematic uncertainties that do not change with p_{T}.

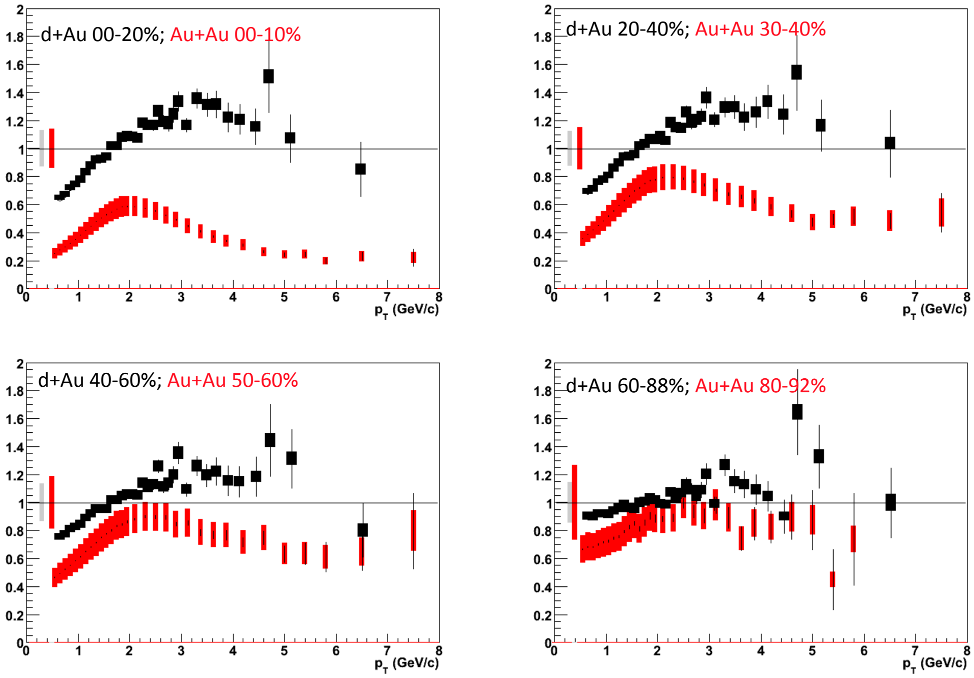

Figure 4.3: Comparison of R_{dAu} (black points) and R_{AuAu} [14] (red points) in several centrality bins. The centrality indicated is defined independently in the different systems.

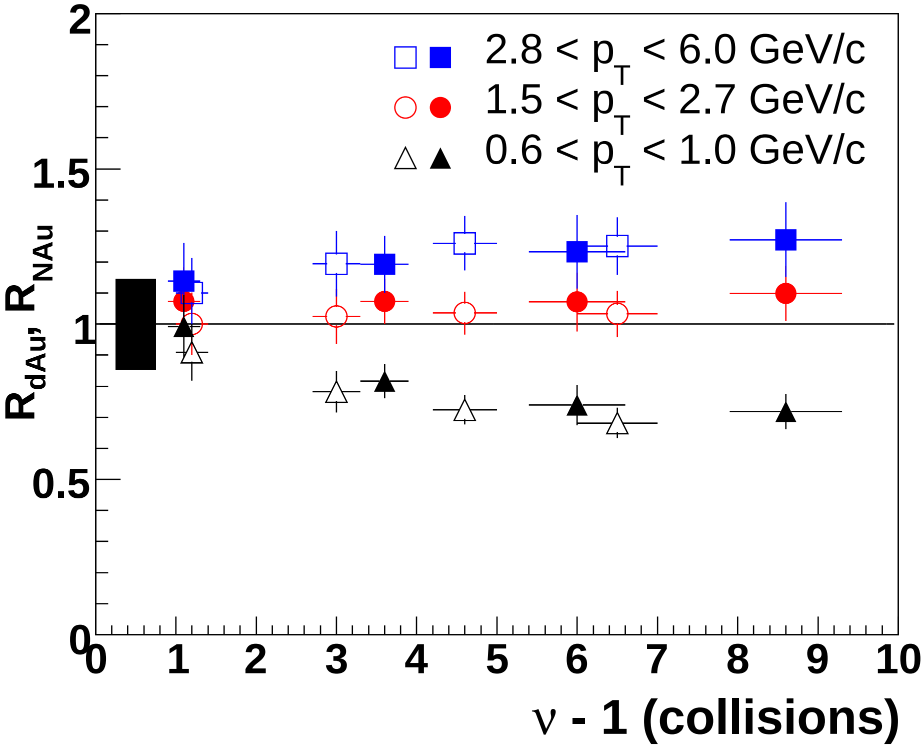

Figure 4.4: R_{dAu} and R_{NAu} values averaged in three momentum ranges as functions of $\nu - 1$. Open symbols represent R_{dAu}, closed symbols R_{NAu}. Circles correspond to the momentum range 2.8–6.0 GeV/c, squares for 1.5–2.7 GeV/c, and triangles for 0.6–1.0 GeV/c. Point by point uncertainty bars show the quadratic sum of the statistical uncertainty on R_{AB} and the systematic uncertainties that change with ν. The box on the far left represents the size of the systematic uncertainty that does not change with ν. Horizontal bars show the uncertainty on the value of ν for each centrality class.

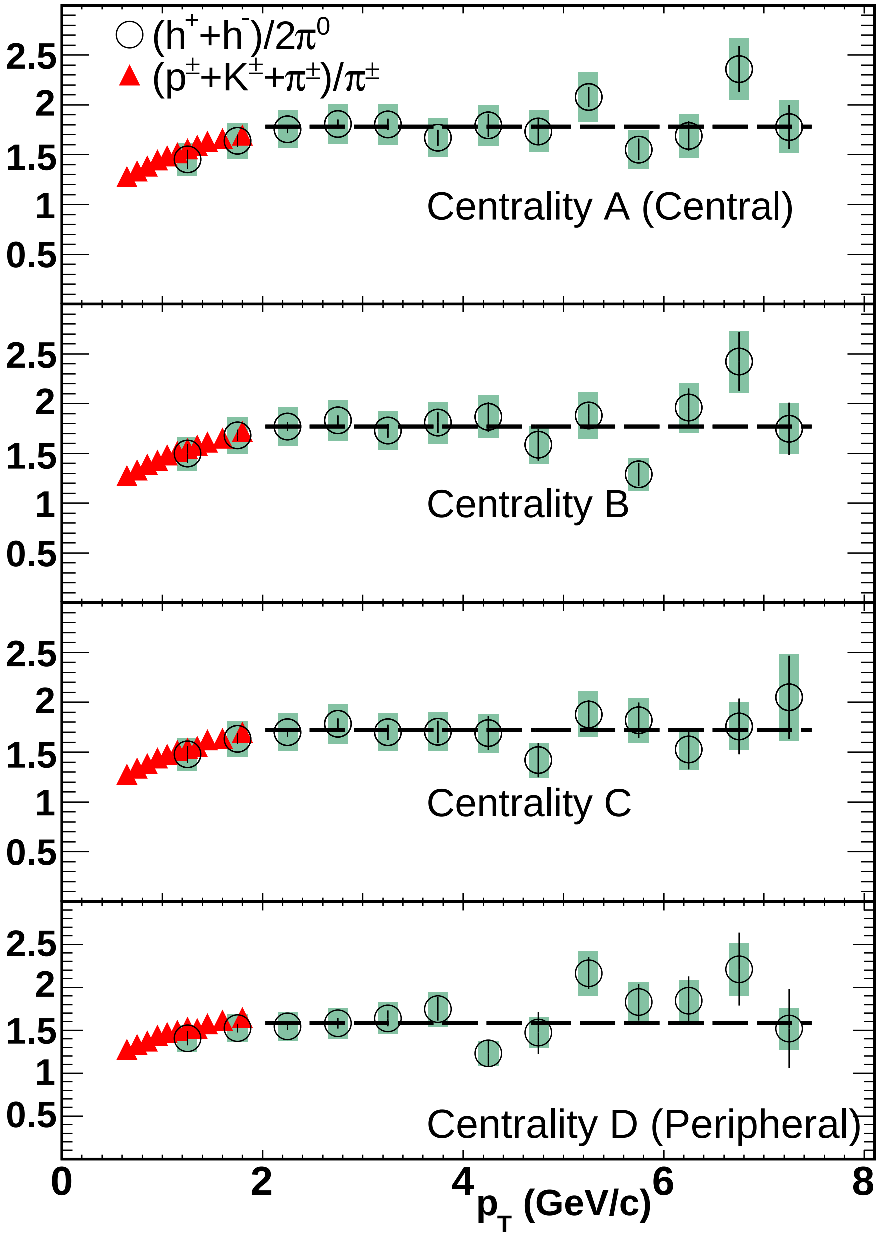

Figure 4.5: $(h^+ + h^-)/2\pi^0$ ratios as functions of transverse momentum from d+Au collisions in four centrality bins. Open cicles are the charged hadron spectra from the present analysisdivided by π^0 data from [82]. Bars indicate statistical uncertainties, and the shaded boxes systematic uncertainties. Triangles are the $(p^{\pm}+K^{\pm}+\pi^{\pm})/\pi^{\pm}$ ratios from [69], with statistical uncertainties roughly the size of the symbols.

Part III

Run 8

Chapter 5

Run 8 Data Analysis

This chapter describes the analysis of cross-rapidity correlations in Run 8 d+Au and p+p data. The data was recorded by PHENIX in the 2008 RHIC run.

5.1 Overview

In the previous chapters we described how the midrapidity inclusive charged hadron spectra measured in d+Au collisions are a useful tool for studying initial state effects and distinguishing them from final state effects. To better study these initial state effects we may attempt to probe different areas in the Bjorken x distribution of the Au nucleus. The d+Au system provides the opportunity to do so and better characterize the gluonic structure of the Au nucleus. As discussed in section 1.2 there is strong theoretical and experimental interest in the possibility of nuclear shadowing and gluon saturation influencing the parton distribution at low x in the nucleus. These coherent effects should be present even in the proton and be even more pronounced in the Au nucleus which we may investigate through d+Au collisions.

Assuming a co-linear kinematic framework the effective x of the Au is:

$$x_{g,Au} = \frac{p_{T^1} e^{-y_1} + p_{T^2} e^{-y_2}}{\sqrt{s}} \tag{5.1}$$

where we take the d going direction as positive rapidity. So to access lower x we look to forward rapidity (d going direction, positive y) which we can compare to higher x at backwards and midrapidity.

In this analysis we measure two particle yields where one particle is a π^0 reconstructed via the $\gamma\gamma$ channel in the forward or backward MPC ($3.1< |\eta| <3.7$) and the other is a midrapidity unidentified charged hadron in the central arms ($|\eta| < 0.35$). In the symmetric p+p collision system we expect that correlations triggered in the North MPC (forward direction, positive η) will be the same as those triggered in the South MPC (backward direction, negative η). However in the d+Au collisions system where the the North is the d going direction and the South is the Au going direction, we expect the correlations to be different to the extent that the different x regions accessed lead to different physics processes.

In the analysis discussed below we form azimuthal angle correlation functions between the forward (backward) π^0 and midrapidity charged hadron, which we decompose into correlated and uncorrelated components. We extract from these the yields and widths of the correlated part as well as examining the underlying event via the uncorrelated production in p+p and d+Au. Figure 5.1 shows a cartoon of the measurement.

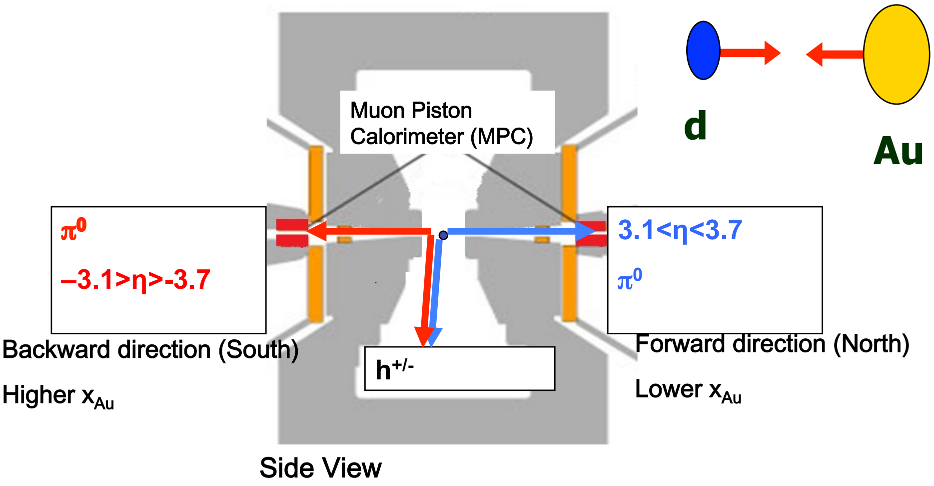

Figure 5.1: A cartoon of the two particle cross rapidity measurement undertaken in this analysis.

5.2 Global Analysis

5.2.1 *d*+Au

The analysis of the Run 8 d+Au event level parameters largely follows that described in section 3.2. In place of the Hulthén description of the deuteron as in equation 3.1, we use a description from [84] based on a dispersion potential-less inverse scattering approach. The S state wave function (the D state probability is only 6.2%) is:

$$u(r_{pn}) = \sum_{j=1}^{16} C_j e^{-m_j r_{pn}}, \;\; m_j = \alpha + m_0(j-1) \qquad (5.2)$$[1]

Figure 5.2 shows the comparison of the probability distribution for the proton - neutron distance calculated from the Hulthén wave function compared with that in equation 5.2 taken from [85]. The use of the more modern description in the Glauber Monte Carlo calculations has little effect on the extracted collision parameters.

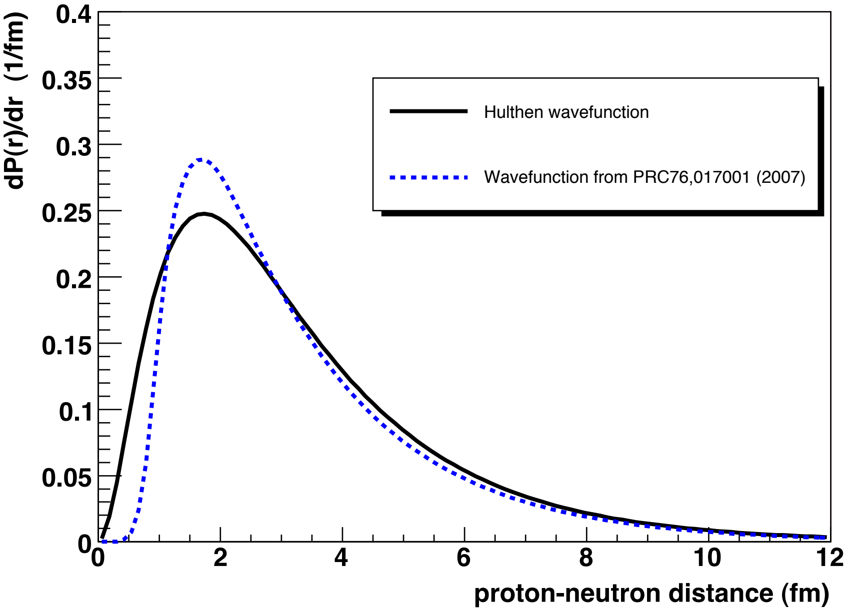

Figure 5.2: Probability distribution for the proton – neutron distance in the deuteron from the Hulthén and the dispersion approach from [84]. The figure is taken from Figure 1 in [85].

The Glauber Monte Carlo calculations were performed for the Run 8 d+Au data set using the Run 8 BBC South spectrum and a slightly modified approach

---

[1] Coefficients C_j and parameters α and m_0 are in [84]

Centrality	$\langle N_{coll}\rangle^{Run3}$	$\langle N_{coll}\rangle^{Run8}$	C_{BBC}^{Run3}	C_{BBC}^{Run8}
00-20%	15.37 ± 1.0	15.1 ± 1.0	0.95 ± 0.029	0.941 ± 0.010
20-40%	10.63 ± 0.7	10.3 ± 0.7	0.99 ± 0.007	1.000 ± 0.006
40-60%	6.95 ± 0.6	6.6 ± 0.4	1.03 ± 0.009	1.034 ± 0.017
60-88%	3.07 ± 0.3	3.2 ± 0.2	1.04 ± 0.027	1.031 ± 0.055

Table 5.1: Comparison of the Run3 and Run 8 Glauber Monte Carlo derived quantities.

to modeling this spectrum was used. Table 5.1 summarizes the differences between the Run 3 and Run 8 values.

5.2.2 *p*+*p*

As discussed above in section 3.2.4 the minimum bias BBC trigger is not perfectly unbiased. This is true also in *p*+*p* collisions, and must be accounted for when measuring particle spectra and correlations. This correction is analogous to C_{BBC} in *d*+Au and is calculated as the ratio of the fraction of the total cross section that the BBC triggering condition is sensitive to divided by the BBC triggering efficiency when there is a charged particle detected by the central arm detectors. This correction factor is 0.545/0.784 with an associated uncertainty on the overall cross section of 9.7% based on the most recent measurements as of this writing [86]. This correction is needed when considering quantities normalized per event in the *p*+*p* data.

5.3 Central Arm Analysis

5.3.1 Central Arm Charged Tracks

The measurement of charged tracks used in this analysis follows but is simpler than that discussed above in section 3.3. Here we do not measure charged tracks with p_{T} >4 GeV/c so background particle contamination is much less at these lower momenta and we do not need to perform the subtractions as in section 3.3. As above we define a track as one in which both X1 and X2 sections were used with a unique U and V wire hit in the DC, as well as at least a favored PC1 hit (see section 2.4). We also make a fiducial cut at 40 cm in the z direction. To ensure good track matching to the outer detectors, we require that the displacement at the PC3 in both ϕ and z direction at the added in quadrature be less than 3 standard deviations. To eliminate electron contamination we require that there be no RICH signal associated with the track.

5.3.2 Run Grouping and Selection

Over the course of the 2008 RHIC run there was significant variability in the performance of the central arm detectors. This variability was not random but largely followed from degradation and occasional repair to the DC and PC1. To account for this we must correct the yields measured in the central arm detectors by the varying efficiencies as appropriate, especially when comparing d+Au to p+p measurements.

To track the efficiency of the DC and PC1 tracking over the course of the d+Au and p+p datasets, we measure the average charged particle multiplicity as a function of run number. To do so we consider charged tracks as a function of the azimuthal angle, ϕ. In ϕ space we can see holes open up in the detector acceptance while some regions remain consistent in their acceptance. A reference run from early in the d+Au running in which the acceptance was quite good was chosen. The number of tracks in a given subsequent run was normalized to the reference run in a consistently robust ϕ region. Figure 5.3 illustrates the procedure in a sample run. Once thus normalized the ratio of the integrals from the reference run and tested run over the entire range of ϕ is a scale factor representing the relative change in acceptance. This factor is shown as a function of run number for d+Au in Figure 5.4 and for p+p in Figure 5.5. Based on the changing acceptance the data is subdivided into run groups with fairly stable acceptance and each run group is divided by the mean acceptance factor for that group. The d+Au data is broken into six run groups and the p+p data into an additional three as shown in table 5.2.

In addition to the run groups, some runs were entirely rejected due to apparently poor detector performance. One run was rejected due to poor track matching, twenty runs were rejected due to an irregular spectral shape, thirty runs due to aberrant acceptance, and ninety four due to bad centrality distributions.

5.4 MPC Analysis

5.4.1 Run Selection

In addition to the runs rejected based on the central arm and global detector response, run quality assurance in the MPC was verified by checking for

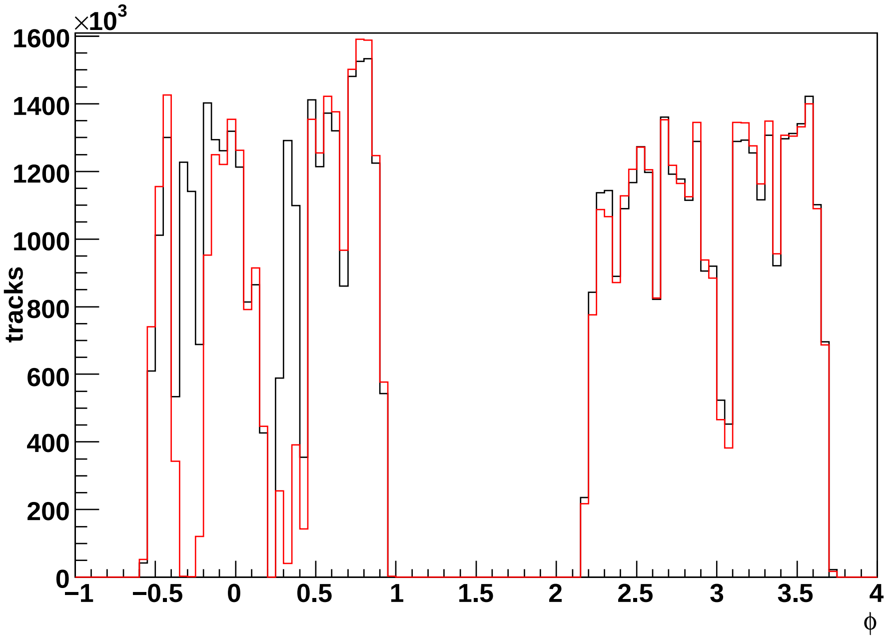

Figure 5.3: A low acceptance run group (red) normalized to the reference run group with better acceptance (black) in the region of $\phi > 2$. In practice for the run by run calculations multiple normalization regions in ϕ were used.

an aberrant number of clusters, energy deposition, or π^0 mass peak. Due to outliers in these metrics ten runs were rejected from the p+p running. In the d+Au running five runs were rejected for both MPCs. In addition to those fifty one outlier runs were rejected for the North MPC. In the South MPC there were only five outlying runs, however there were two streaks in which there was apparently a problem with an entire driver board. Figure 5.6 shows the average energy deposition per event in each tower in two sample runs divided by the average energy deposition per event of all runs. The map on the right is from one of the bad driver board excluded runs and one can clearly see the localized decrease in measured energy. These two groups, the first composed of eight runs but the second a more substantial 209 runs, were excluded from the analysis. Figure 5.7 shows the mean number of clusters per event in the South MPC with the rejected runs demarcated.

Figure 5.4: The relative acceptance factor as a function of run number in d+Au.

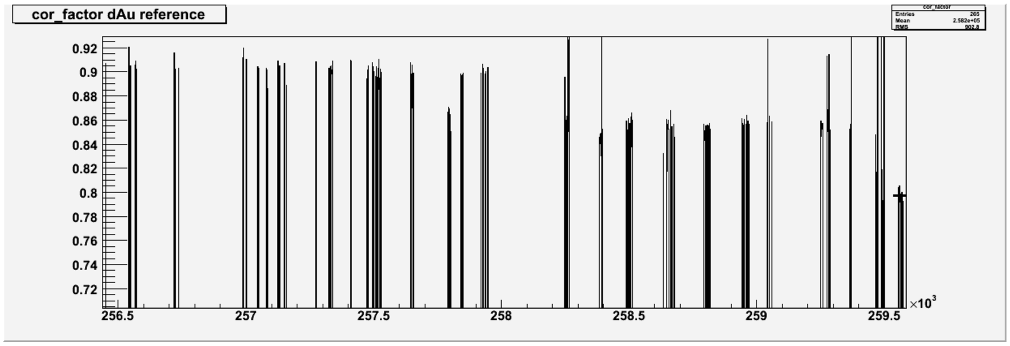

Figure 5.5: The relative acceptance factor as a function of run number in p+p.

5.4.2 π^0 Reconstruction

Prelminary Cuts

Fully reconstructed π^0s are reconstructed in both MPCs by pairing photon clusters. Before pairing we first make preliminary cuts on the electromagnetic calorimeter cluster to ensure that it is indeed a photon track. We cut on the dispersion and χ^2 as defined above in section 2.5, requiring that they be less than 4 cm^2 and 2.5, respectively. Because the analysis compares the North and South MPC responses we impose the rejected tower map of each detector onto the other to ensure that they have as similar acceptances as possible in both η and ϕ.

Following these single cluster cuts, we make several pair cuts to purify the

Begin	End	Acceptance Factor
d+Au Start	249439	1
249440	250787	0.884
250788	251970	0.924
251971	253019	0.876
253020	253629	0.853
253630	d+Au End	0.819
p+p Start	258248	0.898
258249	259372	0.853
259373	p+p End	0.797

Table 5.2: Run groups in Run 8, and their associated central arm acceptance factor.

π^0 sample. For a pair to be considered it must have a minimum separation of 3.5 cm between the two cluster centers and they must be in non-adjacent towers to guard against overlap. To reduce the background we make a cut on the energy asymmetry, $|E_1 - E_2|/(E_1 + E_2)$. Although true π^0s will decay to photons with random energy asymmetry, background pairs will be largely those in which one cluster is at low energy and just happens to pair in the "right place" and so will tend to have a higher energy asymmetry. Therefore, we cut all pairs with asymmetry greater than 0.6. In addition to this cut we also require that all pairs have parent energy between 12 and 20 GeV. At energy less than 12 GeV we are overwhelmed by background in the high multiplicity cases and at energy greater than 20 GeV the photon separation is smaller than the detector resolution with the separation cut in effect. Note that the energy asymmetry cut and the pair energy cut taken together amount to a minimum single cluster energy of 2.4 GeV.

π^0 Identifcation

With these cuts in place we can form invariant mass spectra and identify the π^0 peak. Figures 5.8 and 5.9 show the invariant mass spectra for the North (d going side) and South (Au going side) MPCs in most central d+Au collisions. Shown with the invariant mass spectra are combinatorial backgrounds approximated based on mixed events. If a photon cluster chosen from one event is paired with a photon cluster chosen from an entirely separate interaction the pair, of course, can not be reconstructed to a true π^0, however making these pairs produces a good (albeit imperfect) approximation

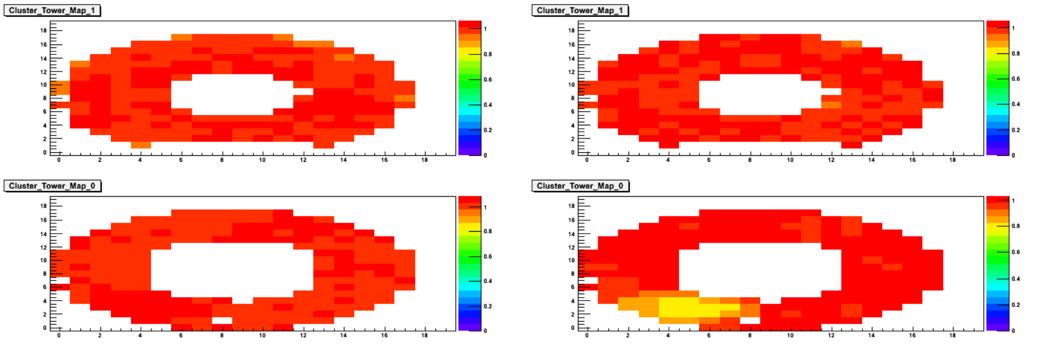

Figure 5.6: On the left is the relative energy deposition tower map for a normal run, and on the right the same for a run plagued with driver board problems. The top map is for the North MPC and the bottom one for the South.

of the random combinatorial background shape. To accurately recreate the background photon clusters are paired only from events that are similar to each other in their centrality and z vertex position. Clearly this method of approximating the background can not capture any correlated background. It can be seen in Figure 5.9 that in the high multiplicity case of the Au going side MPC in central events the π^0 peak is significantly shifted from the true mass of 135 MeV/c^2 and that this shift is more pronounced at higher energy. The location of the π^0 peak is shown as a function of energy for most central and most peripheral d+Au collisions in Figure 5.10. The mass window used to define a photon pair as a reconstructed π^0 is necessarily different in different centrality classes, in the two MPCS, and as a function of parent energy.

Energy Background

It is clear that while stable in the lower multiplicity settings in the higher multiplicity cases at higher energy the mass of the π^0 is significantly distorted. The dependence of the distortion on the multiplicity and energy implies that there is some energy background present in the cluster reconstruction that is distorting the true energy and consequently momentum of the reconstructed π^0s.

Along with the π^0 mass peak from the data, Figure 5.10 shows the mass peaks extracted from simulation. The simulation consists of generated π^0s which are allowed to decay and then embedded into real events. The simulated particles are generated uniformly in p_{T} and η and are weighted appropriately based on a PYTHIA [87] made spectrum. At the embedding stage, one π^0 is

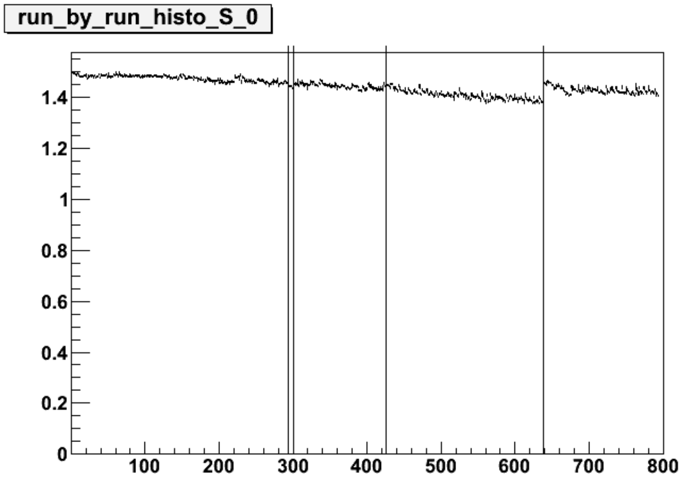

Figure 5.7: Clusters per event as a function of run number (numbered sequentially beginning with one). The two line pairs bracket the excluded runs.

put into one event so we must also weight each particle as appropriate based on the measured π^0 centrality distribution. The simulation and embedding framework were made by B. Meredith. Figures 5.11 and 5.12 show the mixed event background subtracted mass spectrum with the embedded simulation mass spectrum for the low and high multiplicity cases, respectively. The simulation slightly undershoots the data at the 'tail' of the peak; this is likely due to a correlated background due to jets that is unaccounted for in the mixed event approximation of the background which is subtracted (see discussion below in the next subsection). Nevertheless, from Figures 5.10, 5.11, and 5.12 we see that the embedded simulation does a good job of recreating the data, thus providing us a valuable tool with which to attempt to correct the distortions due to the energy background.

The energy background is very difficult to parameterize and subtract statistically. To address it and correct the π^0 p_{T}, we exploit our knowledge of the true π^0 mass. On a pair by pair basis, each cluster of a pair whose mass is within the π^0 peak window has energy added to it such that it would have the true π^0 mass (in the vast majority of cases the energy added is negative). The energy added is the same for both clusters and is calculated using a simple "Newton's method" root finding algorithm.

The effectiveness of this procedure can be checked in simulation; this analysis uses two MPC π^0 p_{T} bins and we can check what fraction of reconstructed

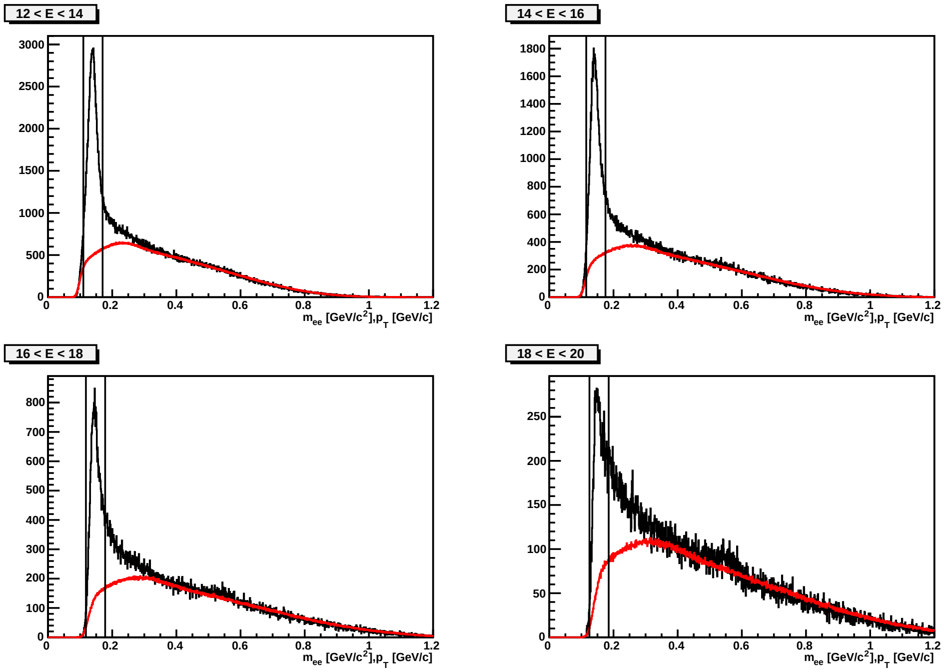

Figure 5.8: The mass spectrum of pairs in the North (d going side) MPC for central d+Au events (00-20%), shown in black, and from (scaled) mixed events in red. The vertical lines denote the π^0 window. The panels are 2 GeV bins of energy from 12 to 20.

embedded simulated π^0s have properly reconstructed $p_{\rm T}$. Table 5.3 shows the fraction of properly binned π^0s in the $0.75<p_{\rm T}<1.0$ GeV/c bin, and the $1.0<p_{\rm T}<2.0$ GeV/c bin in table 5.4, and the mean $p_{\rm T}$ in the bin. Note that with the $p_{\rm T}$ weighting and cuts used, with bins defined by true momentum the mean $p_{\rm T}$ would be 0.87 and 1.14 in the lower and higher bins.

For a more detailed view of where the raw $p_{\rm T}$ reconstruction fails, we can look at the difference between the reconstructed and true $p_{\rm T}$ in the embedded simulation. In the high multiplicity settings of the Au going side MPC for most central event a background is present as seen by the distribution becoming biased towards the positive, as shown in Figure 5.13. In contrast, by using the true mass based $p_{\rm T}$ adjustment procedure described above the difference between the adjusted reconstructed and true $p_{\rm T}$ is nicely centered about zero as shown in Figure 5.14.

One may consider that perhaps the $p_{\rm T}$ adjustment method described above, should not be anchored to the true π^0 mass of 135 MeV/c^2, but rather to the

Event Class	True %	From lower p_T%	From higher p_T%	$<p_T>$
North 00-20%	75.2	16.7	8.1	0.85
North 20-40%	76.6	14.9	8.4	0.85
North 40-60%	76.1	14.5	9.5	0.86
North 60-88%	78.3	12.2	9.4	0.87
North 00-20% (adjusted)	75.9	12.1	12.0	0.87
North 20-40% (adjusted)	77.7	10.6	11.7	0.88
North 40-60% (adjusted)	76.1	11.5	12.4	0.88
North 60-88% (adjusted)	78.5	9.7	11.8	0.88
South 00-20%	55	39.5	5.5	0.78
South 20-40%	64.0	30.3	5.7	0.81
South 40-60%	68.9	23.5	7.6	0.83
South 60-88%	76.7	14.3	9	0.86
South 00-20% (adjusted)	61.9	23.3	14.7	0.85
South 20-40% (adjusted)	68.6	17.8	13.6	0.87
South 40-60% (adjusted)	72.3	14.2	13.5	0.87
South 60-88% (adjusted)	76.8	10.9	12.4	0.88
p+p	80.2	10.8	9.0	0.87
p+p (adjusted)	79.3	9.8	11.0	0.87

Table 5.3: In the reconstructed embedded π^0 $0.75<p_T<1.0$ GeV/c bin the percentage of π^0s reconstructed that have true p_T in that bin, have true p_T lower than 0.75 GeV/c, and higher than 1.0 respectively. The last column shows the mean true p_T in the bin. Adjusted refers to the pair by pair algorithim described in the text.

Event Class	True %	From lower p_T%	From higher p_T%	$<p_T>$
North 00-20%	80.4	19.6	<0.1	1.11
North 20-40%	79.7	20.3	<0.1	1.11
North 40-60%	79.9	20.1	<0.1	1.11
North 60-88%	82.8	17.2	<0.1	1.12
North 00-20% (adjusted)	83.8	16.1	<0.1	1.13
North 20-40% (adjusted)	82.4	17.5	<0.1	1.13
North 40-60% (adjusted)	82.5	17.5	<0.1	1.13
North 60-88% (adjusted)	84.3	15.7	<0.1	1.13
South 00-20%	57.3	42.6	<0.1	1.04
South 20-40%	62.0	38.0	<0.1	1.06
South 40-60%	70.5	29.5	<0.1	1.08
South 60-88%	76.4	23.5	<0.1	1.10
South 00-20% (adjusted)	75.7	24.2	<0.1	1.12
South 20-40% (adjusted)	75.7	24.2	<0.1	1.12
South 40-60% (adjusted)	78.7	21.3	<0.1	1.11
South 60-88% (adjusted)	79.6	20.4	<0.1	1.12
p+p	85.9	14.1	<0.1	1.13
p+p (adjusted)	85.7	14.3	<0.1	1.13

Table 5.4: In the reconstructed embedded π^0 $1<p_T<2.0$ GeV/c bin the percentage of π^0s reconstructed that have true p_T in that bin, have true p_T lower than 1 GeV/c, and higher than 2.0 respectively. Adjusted refers to the pair by pair algorithim described in the text.

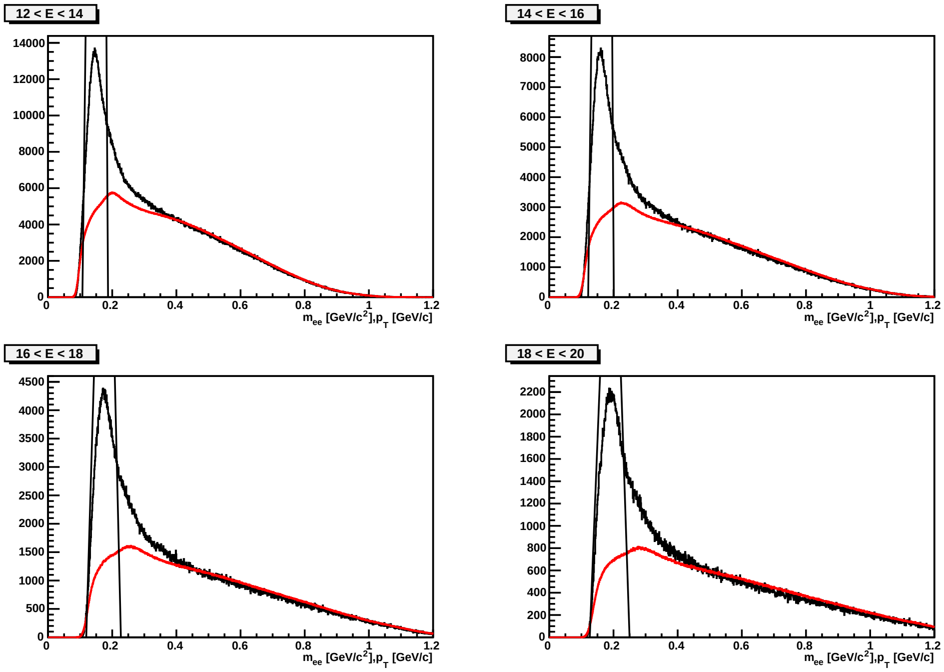

Figure 5.9: The mass spectrum of pairs in the South (Au going side) MPC for central d+Au events (00-20%), shown in black, and from (scaled) mixed events in red. The vertical lines denote the π^0 window. The panels are 2 GeV bins of energy from 12 to 20.

mass that the detector would reconstruct due to any distortion in reconstruction *other than* the energy background, e.g. position resolution. This method was checked by first using the embedded simulation to find the mass at which π^0s would be reconstructed if they were fixed to the truth energy but allowed to make any other reconstruction mistakes. Once this mass was found, it could be used as an anchor in place of 135 MeV/c^2 in the method described above. Using the fraction of π^0s belonging in the bin in which they are reconstructed as the metric of effectiveness, this procedure was consistently worse than anchoring to 135 MeV/c^2. This decline in effectiveness was on the order of several percent.

The success in simulation gives us confidence to use this method on the data. Further this method may have wider applicability in any calorimeter reconstruction procedure that contains significant background or is resolution limited. Even in the lower multiplicity cases, i.e. the d going side MPC in which the improvement is minimal for the present analysis, if one loosens the

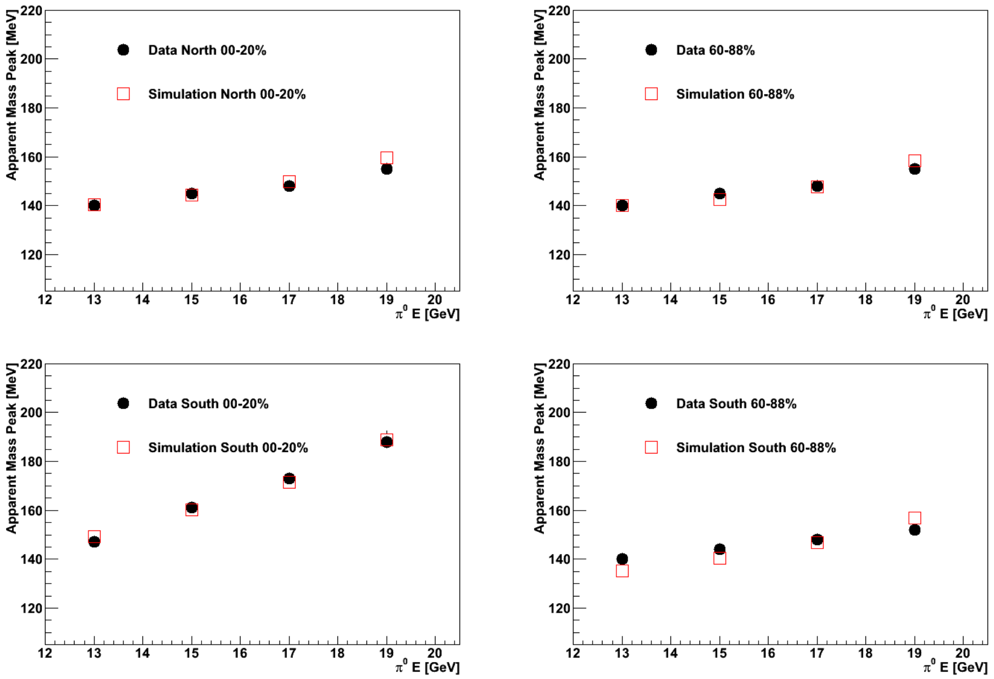

Figure 5.10: The location in mass of the π^0 peak as a function of the π^0 energy in data and embedded simulation for most central (left) and most peripheral (right) events in the d going side (top) and Au going side (bottom) MPCs in d+Au collisions.

mass window for π^0 selection to allow all π^0s in the simulation, the fraction of π^0s in the proper p_{T} bin is about 60% with only the raw reconstruction, whereas with the π^0 mass based adjustment it is consistently greater than 70%. We believe this method is based on robust assumptions and that using our knowledge of the true mass of the particle being measured to refine its kinematic characteristics may often be the correct approach for particle reconstruction in a calorimeter.

Signal to Background

Following the above cuts and reconstruction procedure the signal to combinatorial background is calculated based on using the mixed event derived mass spectra as background. Because the π^0 peak shifts with energy and with it the defined signal region, to calculate the signal to background ratio we use a weighted average of the mass spectra in 2 GeV energy bins within a given

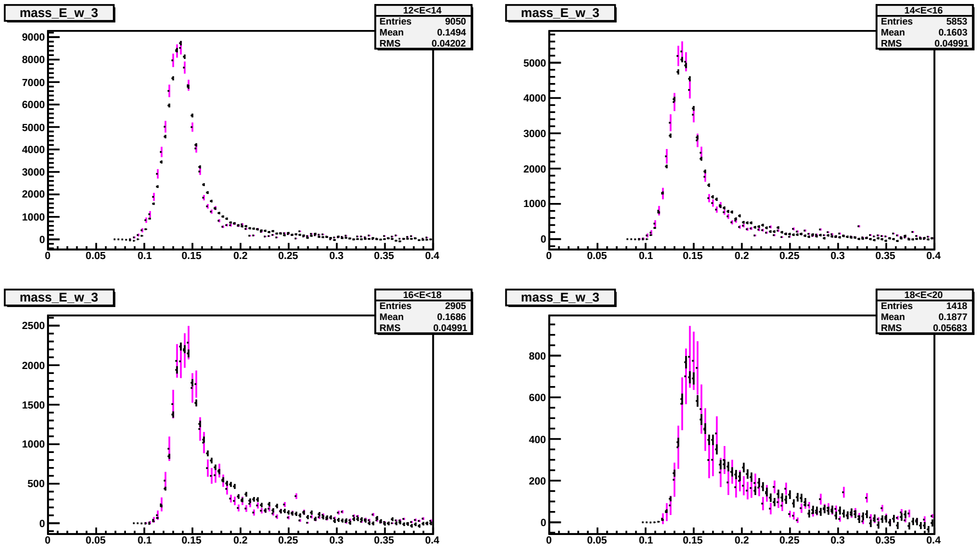

Figure 5.11: The mass spectrum of pairs in the d going side MPC for most peripheral events (60-88%) after subtraction of the scaled mixed event distribution in black. In pink the reconstructed embedded simulated π^0s scaled to match at the peak. The panels from left to right and top to bottom are 2 GeV bins of energy from 12 to 20 GeV.

p_{T} bin.

To constrain any residual contamination in the signal peak due to a correlated background that is not accounted for by the mixed event spectra subtraction, a procedure based on the shape of the reconstructed embedded simulated π^0 mass spectrum is used. In other analyses, the same problem is tackled in the PHENIX central arm calorimeter by fitting a polynomial on either side of the signal peak to estimate the background and evaluating its contribution in the peak region[88]. However, because of the 3.5 cm photon separation cut we don't see the background at mass less than the signal peak, so we must take a different approach. To do so we start with the assumption that the reconstructed simulated π^0 mass spectrum has the true signal shape. We still can not definitively say that there is no remaining background so we add an additional background term, bg(m). We do not know *a priori* what the shape of bg(m) is, so we use three different functional forms, a constant, a gaussian, and a landau distribution to model it. We then define a new histogram of simulated π^0 + bg(m), composing all the event correlated yield. Although the agreement shown in Figures 5.11 and 5.12 is good, the simulated spectra

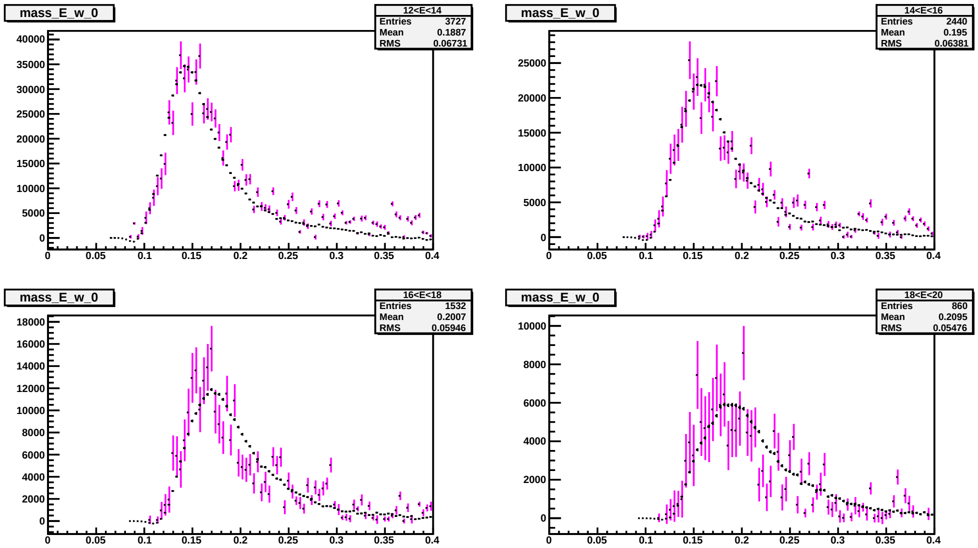

Figure 5.12: The mass spectrum of pairs in the Au going side MPC for most central events (00-20%) after subtraction of the scaled mixed event distribution in black. In pink the reconstructed embedded simulated π^0s scaled to match at the peak. The panels from left to right and top to bottom are 2 GeV bins of energy from 12 to 20 GeV.

is scaled to match the mixed event derived background subtracted data peak and we in principle do not know whether the simulated shape is "sitting on" a background and should be scaled somewhat less. Therefore we don't know the relative contributions of the signal and background remaining in the event by event correlated data. To determine the appropriate background level we let the normalization of the bg(m) term float as a parameter, and compare to the data with a Kolmogorov-Smirnov test. This test checks for the compatibility of the shapes being compared irrespective of their absolute normalization. We iterate over the parameters of bg(m) to find the form of simulated π^0 + bg(m) that is most compatible with the data as judged by the Kolmogorov-Smirnov test. The resultant bg(m) is then taken as the background component remaining even after subtraction of the mixed event derived background mass spectrum. The ratio of the bg term to the simulated π^0 spectrum inside the π^0 definition mass window used in the data is taken as the signal to "residual background" ratio.

This procedure is performed independently for each centrality class and in 2 GeV π^0 energy slices. The landau form of bg(m) produces the shape

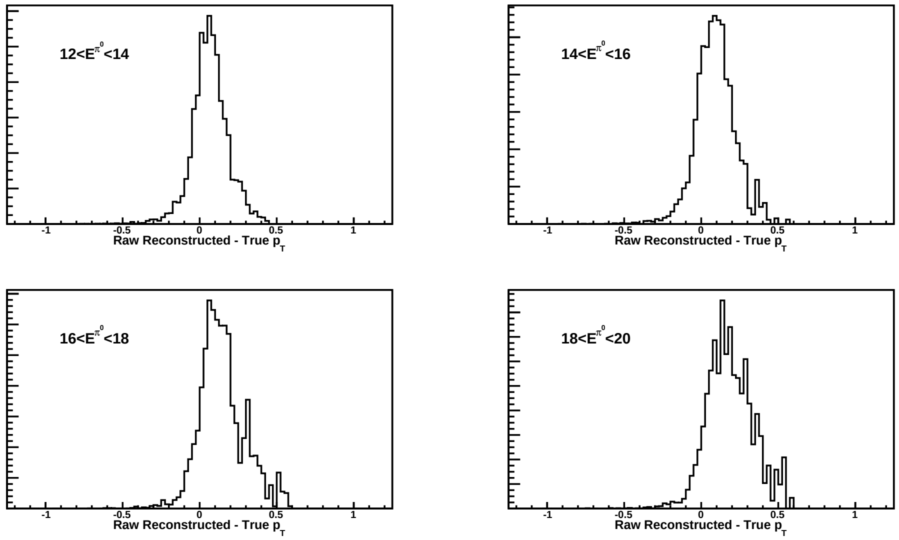

Figure 5.13: Raw reconstructed - True p_T for most central events in the Au going side MPC in four energy bins.

most compatible with the data. The gaussian shaped background produces a lower level of compatibility but still a reasonable description of the data, and so is used to estimate an uncertainty on the values. A constant is not a good description of the remaining correlated background. Figures 5.15 and 5.16 are similar to Figures 5.11 and 5.12 but have the embedded signal shape supplemented by a best calculated landau background term.

Tables 5.5 and 5.6 show the estimated signal to background ratio calculated from the mixed event mass spectra as well as the percentage of the remaining correlated pairs which are estimated to be signal as discussed above. The uncertainty on the mixed event derived signal to background ratio is estimated by varying the normalization of the mixed event spectra. We do not know the true background shape and the landau function used is only a plausible description not a necessary conclusion regarding the underlying processes. Based on the maximal discrepancy with a comparison to a gaussian description of the background, we set the uncertainty on the correction to be 33%.

Efficiency

Using the embedded simulation described above we may calculate the efficiency for π^0 detection in the MPCs as the ratio of generated π^0s that survive

Event Class	p_{T} [GeV/c]	S/B (uncorrelated)	S/Total (residual)	Cumulative S/Total
p+p	0.5-0.75	3.42 ± 0.07	0.86	0.64 ± 0.06
	0.75-1.00	5.13 ± 0.05	0.86	0.67 ± 0.08
	1.00-1.25	7.52 ± 0.26	0.85	0.69 ± 0.09
	1.25-1.50	7.56 ± 0.53	0.85	0.70 ± 0.09
	1.00-2.00	7.60 ± 0.29	0.85	0.70 ± 0.09
North 00-20%	0.5-0.75	2.30 ± 0.05	0.78	0.54 ± 0.06
	0.75-1.00	3.16 ± 0.01	0.81	0.59 ± 0.05
	1.00-1.25	3.29 ± 0.20	0.84	0.64 ± 0.05
	1.25-1.50	3.30 ± 0.29	0.85	0.64 ± 0.05
	1.00-2.00	3.30 ± 0.22	0.85	0.64 ± 0.05
North 20-40%	0.5-0.75	2.21 ± 0.05	0.87	0.60 ± 0.04
	0.75-1.00	3.07 ± 0.01	0.87	0.63 ± 0.04
	1.00-1.25	3.35 ± 0.21	0.88	0.66 ± 0.05
	1.25-1.50	3.36 ± 0.34	0.88	0.66 ± 0.05
	1.00-2.00	3.36 ± 0.23	0.88	0.66 ± 0.05
North 40-60%	0.5-0.75	2.29 ± 0.05	0.77	0.53 ± 0.06
	0.75-1.00	3.20 ± 0.01	0.80	0.59 ± 0.06
	1.00-1.25	3.13 ± 0.20	0.84	0.64 ± 0.05
	1.25-1.50	3.14 ± 0.28	0.84	0.64 ± 0.05
	1.00-2.00	3.16 ± 0.22	0.84	0.64 ± 0.05
North 60-88%	0.5-0.75	2.47 ± 0.05	0.81	0.58 ± 0.05
	0.75-1.00	3.72 ± 0.01	0.85	0.64 ± 0.05
	1.00-1.25	3.56 ± 0.23	0.88	0.69 ± 0.05
	1.25-1.50	3.58 ± 0.27	0.88	0.69 ± 0.05
	1.00-2.00	3.60 ± 0.25	0.88	0.69 ± 0.05

Table 5.5: The signal to background ratios for the North MPC. (The correction due to the residual background is taken with a 33% uncertainty.)

Event Class	p_{T} [GeV/c]	S/B (uncorrelated)	S/Total (residual)	Cumulative S/Total
South 00-20%	0.5-0.75	1.23 ± 0.09	0.77	0.44 ± 0.05
	0.75-1.00	1.50 ± 0.03	0.77	0.44 ± 0.05
	1.00-1.25	1.46 ± 0.20	0.77	0.46 ± 0.05
	1.25-1.50	1.45 ± 0.24	0.77	0.46 ± 0.05
	1.00-2.00	1.43 ± 0.23	0.75	0.46 ± 0.05
South 20-40%	0.5-0.75	1.12 ± 0.05	0.86	0.46 ± 0.03
	0.75-1.00	1.44 ± 0.01	0.80	0.45 ± 0.04
	1.00-1.25	1.41 ± 0.16	0.75	0.45 ± 0.06
	1.25-1.50	1.41 ± 0.26	0.74	0.46 ± 0.06
	1.00-2.00	1.41 ± 0.17	0.74	0.44 ± 0.06
South 40-60%	0.5-0.75	1.19 ± 0.03	0.89	0.49 ± 0.03
	0.75-1.00	1.68 ± 0.01	0.86	0.52 ± 0.04
	1.00-1.25	2.35 ± 0.16	0.83	0.54 ± 0.05
	1.25-1.50	2.36 ± 0.37	0.83	0.56 ± 0.09
	1.00-2.00	2.36 ± 0.18	0.83	0.54 ± 0.06
South 60-88%	0.5-0.75	1.70 ± 0.03	0.85	0.56 ± 0.04
	0.75-1.00	2.75 ± 0.01	0.86	0.61 ± 0.04
	1.00-1.25	3.66 ± 0.21	0.89	0.67 ± 0.04
	1.25-1.50	3.69 ± 0.51	0.89	0.68 ± 0.04
	1.00-2.00	3.72 ± 0.23	0.89	0.67 ± 0.04

Table 5.6: The signal to background ratios for the South MPC. (The correction due to the residual background is taken with a 33% uncertainty.)

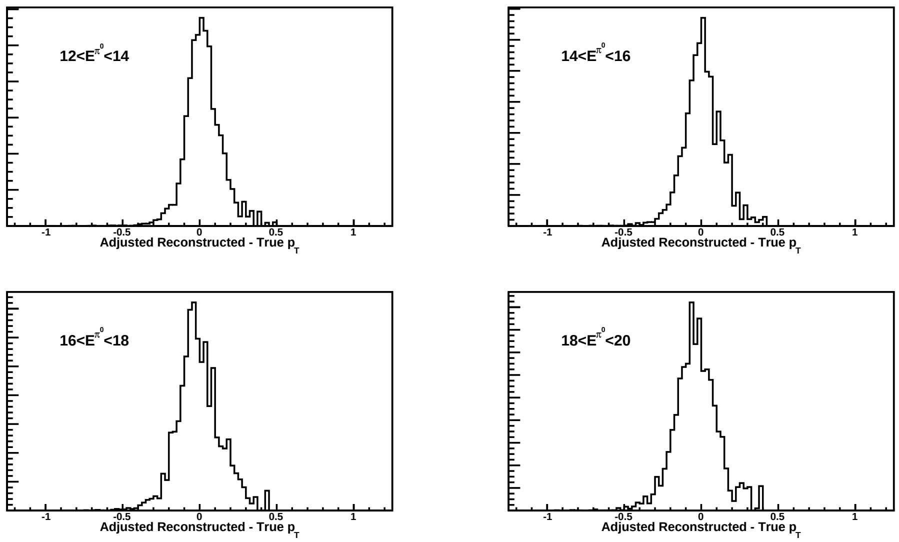

Figure 5.14: Adjusted reconstructed - True $\mathrm{p_T}$ for most central events in the Au going side MPC in four energy bins.

the analysis cuts to the input π^0s. To ensure that the efficiency as a function of p_T is as accurate as possible we weight the input spectra with the measured π^0 spectrum, calculate the efficiency, recalculate the π^0 spectrum, and iterate. To use the measured spectrum as a weighting function we fit the data to a function:

$$f(p_\mathrm{T}) = p_\mathrm{T} A e^{-b p_\mathrm{T}} \tag{5.3}$$

(It is worth noting that in generating the π^0 p_T spectrum the yield is plotted in the center of the bin, whereas the yield is actually *counted* as in the entire bin. As mentioned in section 3.3.3 we correct for this discrepancy by employing a bin width correction that shifts the yield value based on the local spectral shape.) For the first iteration we use the weight as naturally generated by PYTHIA. The iterative procedure is performed with the π^0 spectrum in transverse momentum, however in η we rely on the PYTHIA weights. These steps are performed independently for each MPC and in each centrality class, as well as in p+p.

As a systematic check the same procedure is performed using (modified)

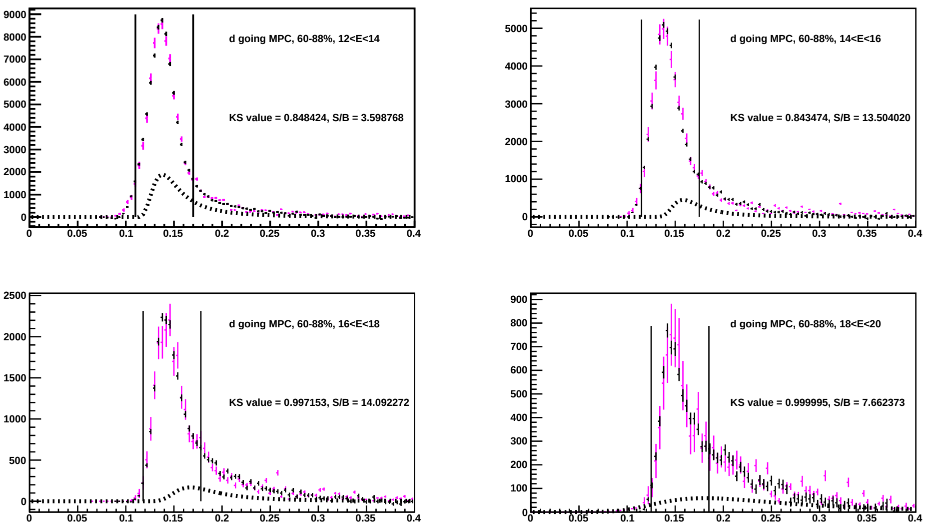

Figure 5.15: The reconstructed embedded simulated π^0s (as in Figure 5.11) plus a landau background term in pink. The black histogram is the data, and the dashed line shows the landau description of the background, and the vertical lines show the mass window used. Shown for peripheral events in the d-going side MPC.

Hagedorn functions:

$$
\begin{aligned}
g(p_{\mathrm{T}}) &= \frac{a p_{\mathrm{T}}}{(e^{-b p_{\mathrm{T}} - c p_{\mathrm{T}}^2})^n} \\
h(p_{\mathrm{T}}) &= \frac{a}{(e^{-b p_{\mathrm{T}} - c p_{\mathrm{T}}^2 - p_{\mathrm{T}}/d})^n}
\end{aligned}
\tag{5.4}
$$

In addition, with the best fit $f(p$T we "by hand" change the slopes in p_{T} and η by 5% in either direction, and calculate the efficiency resulting from such a weighting. The largest deviation in the efficiency from these variations is used for an estimate of the uncertainty.

Typically, the parameters of both functions converged to within 1% after about 5 iterations and were stable to .01 % or better after a dozen iterations; in practice we take the efficiency values after 15 iterations. The overall efficiencies for different event classes are shown in Table 5.7.

For the higher efficiency cases, e.g. North MPC with $0.75<p_{\mathrm{T}}<1.0$, the cumulative efficiency is broken down in different cuts approximately as (they are listed independently not sequentially and are largely orthogonal):

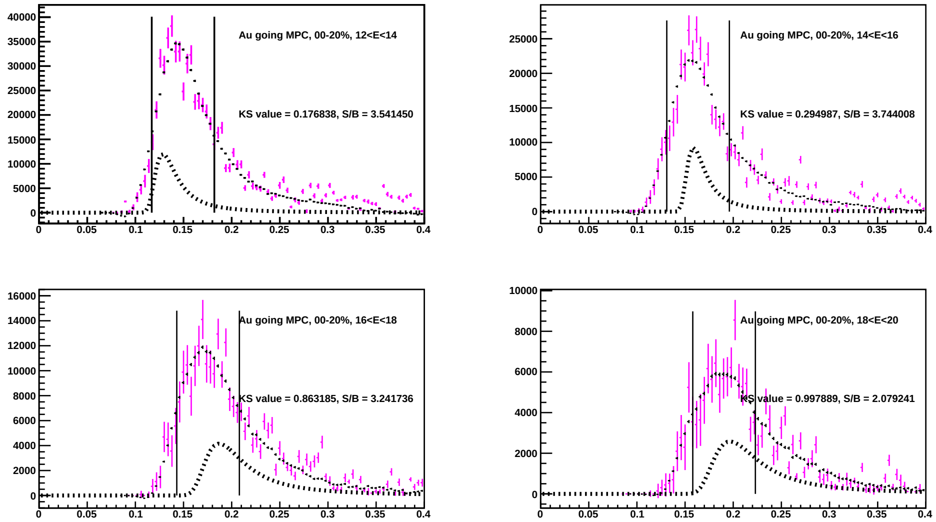

Figure 5.16: The reconstructed embedded simulated π^0s (as in Figure 5.12) plus a landau background term in pink. The black histogram is the data, and the dashed line shows the landau description of the background, and the vertical lines show the mass window used. Shown for central events in the Au-going side MPC.

- Cluster Cuts - 60%
- Excluded Towers - 90%
- Pair Cuts - 50%
- Kinematic Pair Cuts (mass and energy) - 40%

In the higher multiplicity cases where the efficiency is significantly lower, the decrease is due to a lower efficiency of the cluster cuts (dispersion and χ^2).

5.5 Correlation Analysis

5.5.1 Forming the Correlation Function

With midrapidity charged hadrons and forward (backward) rapidity π^0s defined as above, we may form azimuthal angle, ϕ, correlations between them. To do so we count the number of pairs N^{ab} differentially in $\Delta\phi$, this produces

	$0.5<p_{\mathrm{T}}<0.75$	$0.75<p_{\mathrm{T}}<1.0$	$1<p_{\mathrm{T}}<1.25$	$1.25<p_{\mathrm{T}}<1.5$	$1.0<p_{\mathrm{T}}<2.0$
North 00-20%	2.7±1.7	11.6±0.3	13.9±0.4	6.2±0.7	11.9±0.6
North 20-40%	2.6±1.4	11.3±0.3	13.7±0.4	7.1±0.9	12.0±0.7
North 40-60%	2.4±2.1	11.2±0.5	14.8±0.4	6.7±0.4	13.0±0.5
North 60-88%	2.3±1.6	11.6±0.3	15.5±0.4	7.2±0.5	13.7±0.6
South 00-20%	1.9±0.1	6.9±2.3	6.9±1.2	3.2±0.5	6.5±1.2
South 20-40%	2.6±0.6	8.7±1.4	10.1±1.3	4.2±2.0	9.2±1.4
South 40-60%	2.8±0.6	11.0±0.9	11.7±0.7	5.3±1.1	10.5±0.7
South 60-88%	2.7±1.2	12.8±0.7	15.2±0.8	6.8±0.6	13.5±0.7
p+p	2.5 ± 0.5	11.7 ± 0.6	14.6±0.6	7.2±0.8	13.5±0.9

Table 5.7: The overall π^0 efficiency [in percent] calculated in different MPC scenarios.

the raw correlation function a sample of which is shown in Figure 5.17 (top). The raw correlation function is somewhat misleading as it is heavily influenced by the acceptance of the PHENIX detector; even for perfectly isotropic particle production the raw correlation function would display distinct features reflecting the limited acceptance of the detectors (in particular the two arm central detectors). To determine the acceptance of the detectors in $\Delta\phi$ we use mixed event pairs. There is no true correlation between an MPC π^0 and a midrapidity charged hadron from different events, i.e. their relative angular distribution is isotropic, so the features present in the mixed event pair $\Delta\phi$ distribution are only acceptance effects. As in the mixed event photon pairing for the determination of the π^0 background, the correlations are only drawn from mixed events with similar centrality and z vertex position. Figure 5.17 (middle) shows a sample mixed event pair derived acceptance function.

To correct the raw correlation function we divide by the acceptance function normalized to 2π. The acceptance corrected correlation function, C($\Delta\phi$), is thus:

$$C(\Delta\phi) = \frac{dN^{ab}}{d\Delta\phi} \frac{\int_0^{2\pi} \frac{dN^{ab}_{mix}}{d\Delta\phi} d\Delta\phi}{2\pi \frac{dN^{ab}_{mix}}{d\Delta\phi}} \tag{5.5}$$

A sample acceptance corrected correlation is shown in Figure 5.17 (bottom).

Correlation functions are calculated in this way for forward (and backward) π^0s with midrapidity unidentified charged hadrons. To simplify handling of the correlation function we renormalize it by dividing by the number of π^0s. The correlations are made separately in each centrality bin of d+Au and in p+p. They are further divided into two π^0 p_{T} bins: $0.75 < {p_{\mathrm{T}}}^{\pi^0} < 1.0$ GeV/c

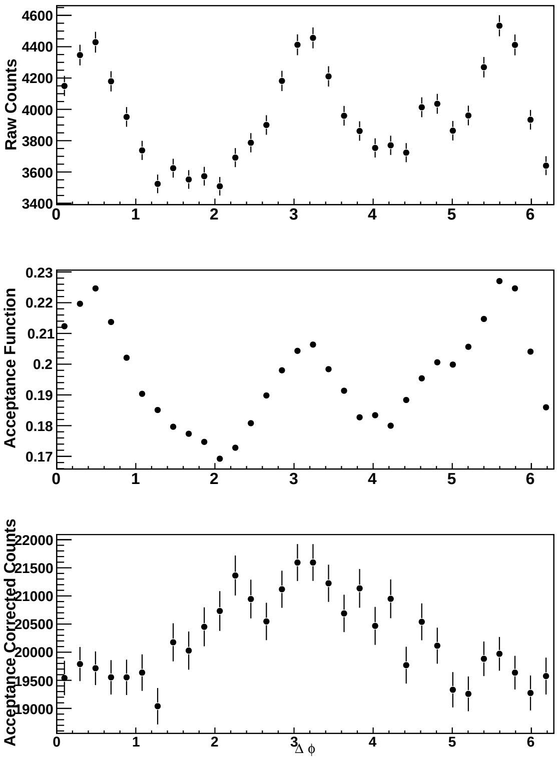

Figure 5.17: A sample raw correlation function (top), acceptance function (middle), and acceptance corrected correlation function (bottom).

and 1.0 $<{p_{\mathrm{T}}}^{\pi^0}<$2.0 GeV/$c$, by three charged hadron p_{T} bins: 0.5 $<{p_{\mathrm{T}}}^{h^{\pm}}<$1.0 GeV/$c$, 1.0 $<{p_{\mathrm{T}}}^{h^{\pm}}<$2.0 GeV/$c$, and 2.0 $<{p_{\mathrm{T}}}^{h^{\pm}}<$4.0 GeV/$c$, for a total of six correlation functions in each event class.

5.5.2 Comparing North and South in p+p

We expect that in the symmetric p+p collision the correlation function should be the same regardless of whether the π^0 used in the correlation function was detected in the forward or backward direction. Confirmation of this is an important step in giving us confidence that we are properly measuring the correlation functions in both detectors (at least in the p+p environment), as well as validating comparison between the Au-going and d-going side MPC correlations. Figure 5.18 shows a direct ratio of the correlation function with a π^0 in the North MPC divided by that with a π^0 in the South MPC. The ratios agree well with unity as expected. We therefore treat North and South MPC triggered correlations together as one dataset.

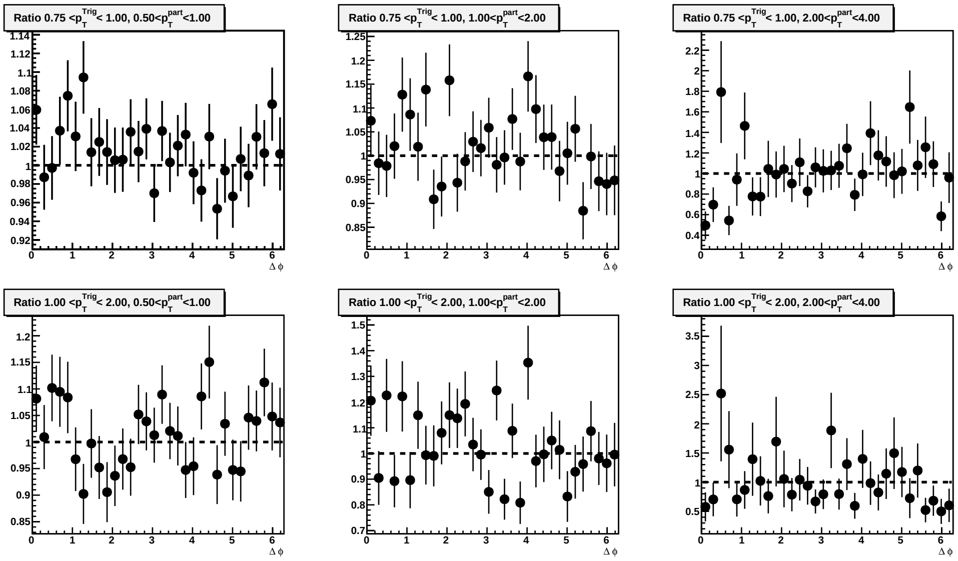

Figure 5.18: The ratio of the correlation functions with a forward rapidity π^0 to those with a backward rapidity π^0 in 2 $\mathrm{p}_{\mathrm{T}}^{\pi^0}$ bins by 3 $\mathrm{p}_{\mathrm{T}}^{h^\pm}$ bins from p+p collisions. The dotted line is drawn at unity.

5.5.3 Decomposing the Correlation Function

There are three essential quantities that we wish to extract from the correlation function: the correlated component of the two-particle yield, it's 'shape', and the uncorrelated component of the two-particle yield. We assume that the correlated part of the yield can be fit as a gaussian, and by it's 'shape' we refer to the width of the gaussian. This correlated production is taken to be (at least!) jet-like, i.e. correlated production is centered as back-to-back in the azimuthal angle. Uncorrelated production is taken to be isotropic, i.e. flat in $\Delta\phi$. The above quantities are clearly not independent in the correlation function, and so the general strategy for extracting them is to use a simultaneous fit to both the gaussian and flat component in the correlation function. The correlated yield per π^0, Y, is then taken as the integral of the gaussian component of the fit.

Because the level of the uncorrelated production is high compared to the correlated component, and a wide enough gaussian approaches a flat line, it is important to make the fitting as robust as possible. To that end the actual fit used is not a single gaussian plus a constant but rather utilizes a gaussian centered at π 'winged' by two more identical gaussians at -π and 3π, respectively, which take into account potential 'wraparound' correlated production in the periodic $\Delta\phi$ domain. The width and yield of the gaussian are very sensitive to the level of the uncorrelated production so to further refine the fitting, correlation functions with different π^0 $\mathrm{p_T}$ but the same hadron $\mathrm{p_T}$ are fit simultaneously with a common parameter for the level of the uncorrelated component, $\mathrm{b_0}$. Once we have divided by the number of π^0s, which we may think of as the the 'triggers' in the two two particle correlation, this parameter should be constant regardless of different π^0 kinematic selections as it reflects the production *uncorrelated* to the 'triggering' π^0 (this is the first order premise of the 'mean seeds mean partners' or 'absolute normalization' method [89]). Fitting $\mathrm{b_0}$ simultaneously in different π^0 selections let's us determine the uncorrelated yield level with twice the data and prevents fits from falling into unrealistic parameter traps. Figure 5.19 shows a sample of the simultaneously fit correlation functions from most central d+Au collisions with π^0s from the North MPC.

It is possible that there may be some correlation in the level of the azimuthally uncorrelated component of the $\Delta\phi$ distribution, breaking the common $\mathrm{b_0}$ parameter. This could be due to triple jet events or similar phenomena that would not appear to be correlated in $\Delta\phi$ but nevertheless change with the π^0 p_{T}. Figures 5.20 and 5.21 show the difference between the $\mathrm{b_0}$ measured with a common fit and the $\mathrm{b_0}$ measured independently in each correlation function.

Although it is likely that the differences are reflections of the different quality of the fits, nevertheless there does seem to be some systematic difference between the two approaches to measuring $\mathrm{b_0}$. This difference is propagated into the extracted yields and widths and taken as a systematic uncertainty on the fitting procedure. As the deviation from zero in figures 5.20 and 5.21 is independent of anything but the π^0 $\mathrm{p_T}$ bin this uncertainty is taken as a common uncertainty, i.e. even if there is a bias imposed by using a common fit across π^0 $\mathrm{p_T}$ bins that bias itself is common across the midrapidity charged hadrons bins.

5.5.4 Contamination in the MPC π^0s

As discussed above there are two main types of background in the π^0s: random combinatorial contamination of the π^0 sample and mis-reconstruction of true π^0 momentum. Both types of contamination are addressed in a similar fashion.

π^0 Combinatorial Contamination

The measured correlated yield of pairs per π^0, Y^{measured}, can be written as:

$$Y^{measured} = \frac{N_{\pi^0}^{signal}}{N_{\pi^0}^{signal} + N_{\pi^0}^{bkg}} Y^{signal} + \frac{N_{\pi^0}^{bkg}}{N_{\pi^0}^{signal} + N_{\pi^0}^{bkg}} Y^{bkg} \tag{5.6}$$

where N$_{\pi^0}$ is the number of π^0s.

Despite the cuts mentioned above there still may be combinatorial background present in π^0 reconstruction so the second term in the above equation is non-zero. To account for the background component of the π^0 selection a 'sideband' selection window is chosen with mass *off* the π^0 peak. Of course, it is impossible to correct the p$_{\mathrm{T}}$, of a sideband pair in the same way as that of a π^0 pair - there is no relevant true mass to anchor it to - but its clusters are still subject to whatever energy background existed in the π^0 pair case. To overcome this, the energy added to each cluster in the π^0 pair case is recorded and then parameterized. This parameterization is then used to adjust the energy of each cluster in a sideband pair before calculating the p$_{\mathrm{T}}$. It is important to remember that the combinatorial background photons also stem mostly from actual π^0s, and so to the sideband correlations are not very different from the π^0 correlations. We use as correction factor on the measured correlated yield:

$$\frac{Y^{signal}}{Y^{measured}} = \frac{N_{\pi^0}^{bkg} + N_{\pi^0}^{signal}}{N_{\pi^0}^{signal}} \left(1 - \frac{N_{\pi^0}^{bkg}}{N_{\pi^0}^{bkg} + N_{\pi^0}^{signal}} \frac{Y^{sideband}}{Y^{measured}}\right) \tag{5.7}$$

where we have substituted $Y^{sideband}$ for Y^{bkg}.

The correction factors are taken with a 100% systematic uncertainty (i.e. the correction factor applied is half equation 5.7 with a symmetric uncertainty associated with it). If there is no measurable yield in the sideband correlation no correction factor is applied to the data associated data point, however, there is still an uncertainty associated with any background contamination of the π^0s. To estimate the uncertainty in that case we conservatively set Yield$^{\mathrm{sideband}}$/Yield$^{\mathrm{measured}}$ = 0.5, and Width$^{\mathrm{sideband}}$/Width$^{\mathrm{measured}}$= 1.50 in equation 5.7, and assign an uncertainty of half the would be correction. This is the case in five bins: for the South MPC in 40-60% centrality for 1<p$_{\mathrm{T}}^{\pi^0}$ <2 GeV/c and 2<p$_{\mathrm{T}}^{h^\pm}$ <4 GeV/c, 60-88% centrality for π^0 p_{T} bins with 1<p$_{\mathrm{T}}^{h^\pm}$ <4.

π^0 Momentum Reconstruction

The method described above for reconstructing the p_T of π^0s in the MPCs is designed to address the energy background in high multiplicity settings. It is a small correction at lower multiplicity (i.e. more peripheral and p+p collisions, and even in more central events in the d going side MPC), but is still there. This is because even without the high multiplicity background there are still detector effects that may shift the π^0 mass peak. In all cases there remain π^0s with misidentified p_T as shown in tables 5.3 and 5.4. Their presence is corrected for with a method similar in spirit to that of the sideband based correction for combinatorial background, but rather than a sideband correlation the true π^0 correlation from the neighboring bin is used. To correct for π^0s in the $0.75<p_T^{\pi^0}<1.0$ GeV/c bin with true p_T less than 0.75 GeV/c, correlations are measured in a bin with $0.5<p_T^{\pi^0}<0.75$ GeV/c. This bin is not used in the main analysis, but is still used for an estimate of the correlation function stemming from π^0s with p_T less than 0.75 GeV/c. Because of the kinematic restrictions there are essentially no π^0s with p_T greater than 2 GeV/c that can leak into the $1<p_T^{\pi^0}<2$ GeV/c bin. To account for π^0s from both higher and lower true momentum in a given bin we can write:

$$
\begin{aligned}
Y^{measured} = & \frac{N_{\pi^0}^{signal}}{N_{\pi^0}^{signal}+N_{\pi^0}^{high}+N_{\pi^0}^{low}} Y^{signal} \\
& + \frac{N_{\pi^0}^{high}}{N_{\pi^0}^{signal}+N_{\pi^0}^{high}+N_{\pi^0}^{low}} Y^{high} \\
& + \frac{N_{\pi^0}^{low}}{N_{\pi^0}^{signal}+N_{\pi^0}^{high}+N_{\pi^0}^{low}} Y^{low}
\end{aligned}
\tag{5.8}
$$

where the *high* and *low* superscripts on Y and N_{π^0} refer to the correlated yield and number of π^0s from the higher and lower π^0 momentum bins, respectively. We then use as a correction factor:

$$
\begin{aligned}
\frac{Y^{signal}}{Y^{measured}} = & \frac{N_{\pi^0}^{high}+N_{\pi^0}^{low}+N_{\pi^0}^{signal}}{N_{\pi^0}^{signal}} \times \\
& \left(1 - \frac{N_{\pi^0}^{high}}{N_{\pi^0}^{high}+N_{\pi^0}^{low}+N_{\pi^0}^{signal}} \frac{Y^{high}}{Y^{measured}} \right. \\
& \left. - \frac{N_{\pi^0}^{low}}{N_{\pi^0}^{high}+N_{\pi^0}^{low}+N_{\pi^0}^{signal}} \frac{Y^{low}}{Y^{measured}} \right)
\end{aligned}
\tag{5.9}
$$

This correction factor is also taken with a full systematic uncertainty.

The two corrections, equations 5.7 and 5.9, are treated as independent and factorizable, as the signal to total ratio remains close across the two π^0 $\mathrm{p_T}$ bins.

5.5.5 Uncorrelated Conditional Yield

In addition to the correlated yield the extraction of which is described in the previous section, we also may study the underlying event. To do so we measure the inclusive central arm charged hadron yield conditioned on a forward (backward) π^0. We define the π^0s as above and then measure the p_T of the midrapdity charged hadrons without regard for the azimuthal angle between them and the MPC π^0. As with the correlated yield this is measured in p+p and four centrality bins in d+Au and two π^0 p_T bins for each MPC.

5.6 Triggering Bias due to MPC π^0s

Requiring a π^0 in the MPC constitutes a bias that may affect the assumptions about triggering discussed above in section 5.2.2 as well as the centrality distribution.

5.6.1 BBC Trigger in p+p

To investigate whether the 0.784 cited above as the BBC triggering efficiency when there is a central arm charged particle is changed by requiring a π^0 in the MPC we use PYTHIA to calculate the probability that the BBC will trigger under the two conditions. Using PYTHIA we ask only whether the relevant particle entered the acceptance of each detector. The left panel of Figure 5.22 shows the PYTHIA calculated BBC efficiency for a pion in the central arms as a function of the pion's p_T. The right panel of Figure 5.22 shows the same quantity but with the additional requirement that there be a π^0 or photon with energy greater than 12 GeV in the MPC. Even in the case without the additional requirement of the MPC π^0 we do not recreate the value of 0.784. However, the additional requirement of the MPC π^0 does not further bias the calculated BBC efficiency, so it appears that the MPC π^0 requirement does not introduce a further bias into the data. We therefore use $\mathrm{C}_{BBC}^{pp} = 0.545/0.784$ as above.

Centrality	$\langle N_{coll} \rangle$	$\langle N_{coll} \rangle^{North\ bias}$	$\langle N_{coll} \rangle^{South\ bias}$
00-20%	15.1	15.1	15.4
20-40%	10.3	10.3	10.5
40-60%	6.6	6.7	6.8
60-88%	3.2	3.3	3.6

Table 5.8: Adjusted $\langle N_{coll} \rangle$ values.

5.6.2 Centrality Bias in d+Au

As may be expected, requiring a high p_{T} particle biases the centrality distribution towards higher multiplicity more central events. Figure 5.23 shows the unbiased centrality distribution along with the centrality distributions of events which contain detected π^0s in the North and South MPCs, respectively. Figure 5.23 shows the biases due to a π^0 with $0.75<\mathrm{p}_{\mathrm{T}}^{\pi^0}<1.0$ GeV/c and there is insignificant dependence on the p_{T} of the π^0. The effect is far more pronounced in the (Au going side) South MPC as it is the South BBC that determines centrality.

By mapping centrality to the mean number of collisions using the values in Table 5.1 we can use these distributions to calculate an adjusted mean number of binary collisions within a given centrality window. These values are shown in Table 5.8. In addition to the native uncertainty on the $\langle N_{coll} \rangle$ values, we assign a 30% uncertainty to the adjustments due to the imprecision of the centrality to $\langle N_{coll} \rangle$ mapping. It is necessary to consider the biased $\langle N_{coll} \rangle$ values when studying the underlying event in the central arm detectors. For measurements such as those described in section 5.5.5 in which we wish to examine the underlying event with the additional requirement of a forward or backward π^0, the biased $\langle N_{coll} \rangle$ are the appropriate values to scale the yield by.

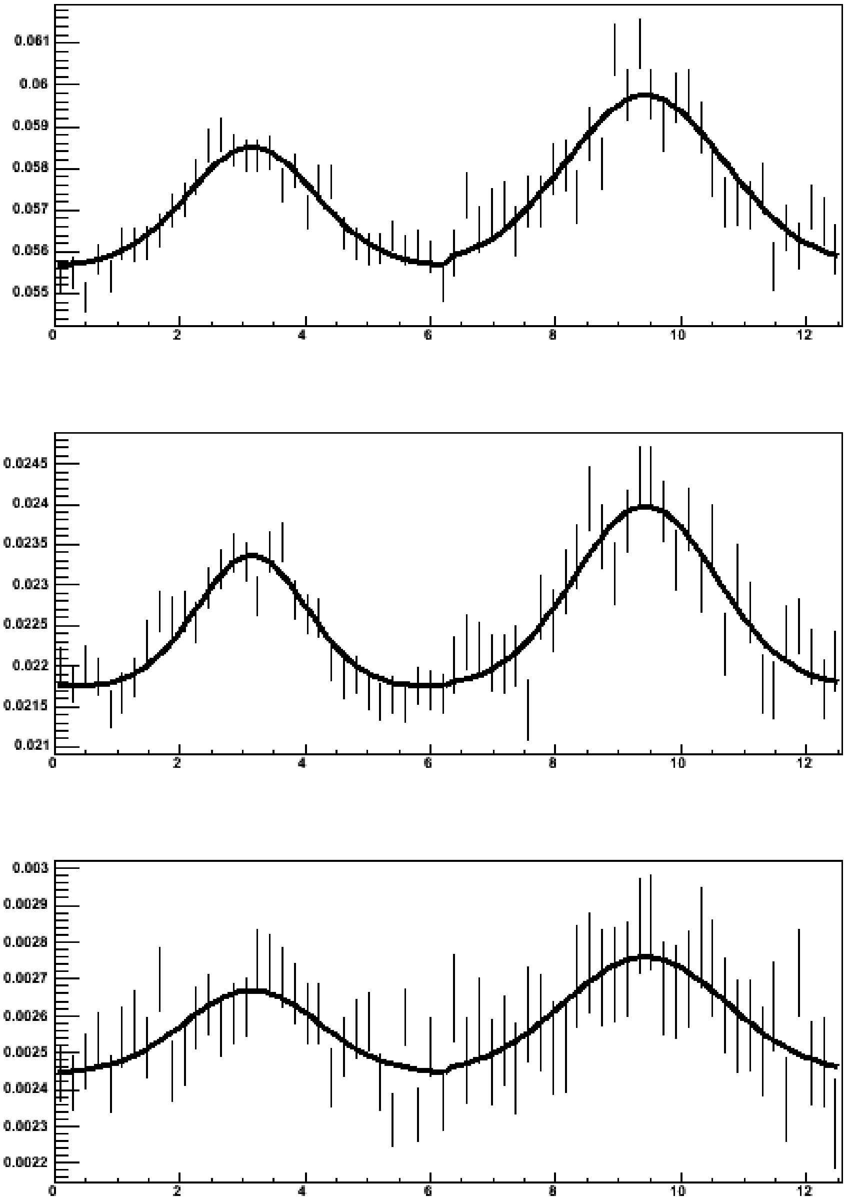

Figure 5.19: The fit North MPC to midrapidity correlation functions normalized by the number of forward π^0s for 00-20% centrality. From top to bottom the rows are $0.5<\mathrm{p}_\mathrm{T}^{h^\pm}<1.0$, $1.0<\mathrm{p}_\mathrm{T}^{h^\pm}<2.0$, and $2.0<\mathrm{p}_\mathrm{T}^{h^\pm}<4.0$. In each row on the left plotted from 0 to 2π is $0.75<\mathrm{p}_\mathrm{T}^{\pi^0}<1.0$ and plotted from 2π to 4π is $1.0<\mathrm{p}_\mathrm{T}^{\pi^0}<2.0$. The two π^0 bins are plotted on the same (artificial) axis as their fits share a common b_0 parameter, however, they are two separate fits and there should be some discontinuity at 2π.

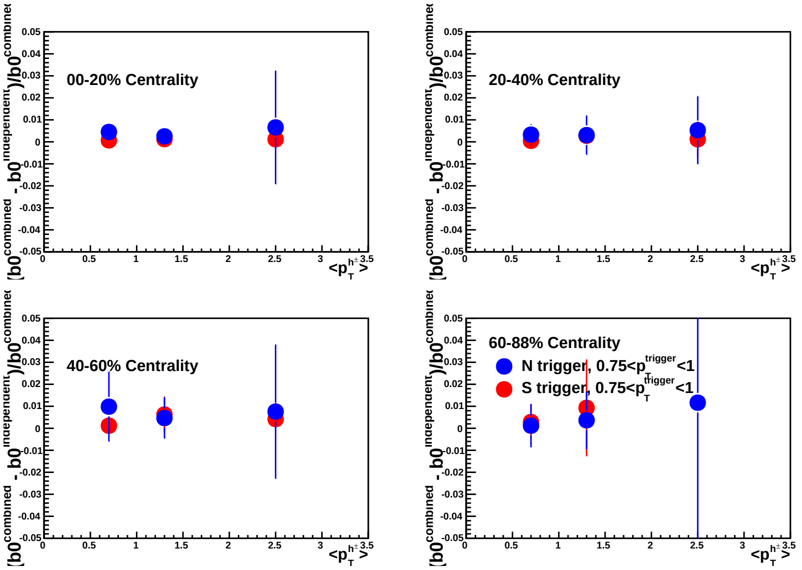

Figure 5.20: The quantity ($b_0^{combinedfit}$ - $b_0^{independentfit}$)/$b_0^{combinedfit}$ for 0.75<$p_T^{\pi^0}$ <1.0 GeV/c as a function of mean charged hadron p_T. Missing points indicate that the independent fit failed to converge. From left to right and top to bottom the plots are for most central and most peripheral.

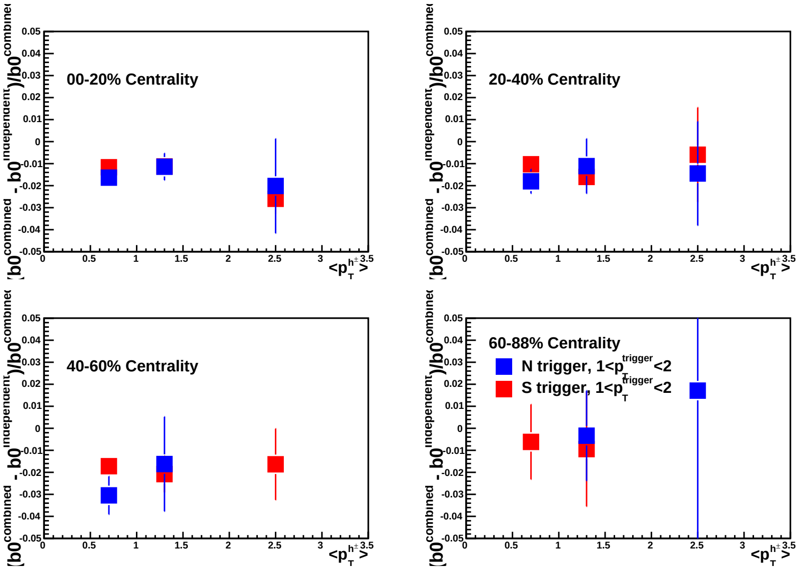

Figure 5.21: Like figure 5.20 for 1<$p_T^{\pi^0}$ <2 GeV/c.

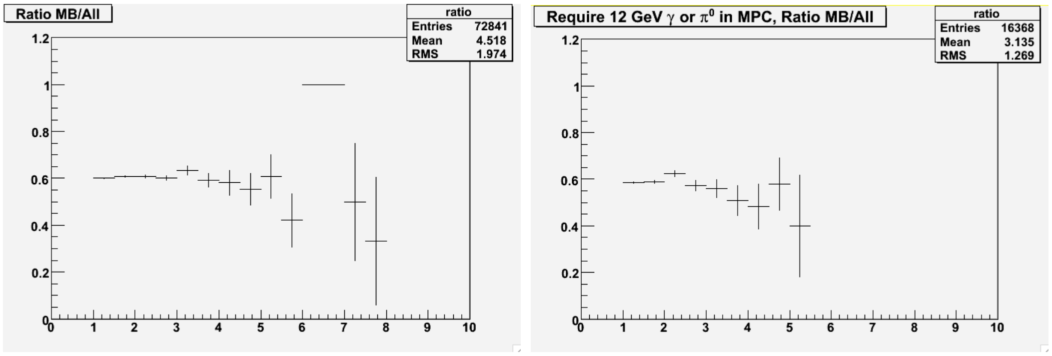

Figure 5.22: The PYTHIA calculated BBC triggering efficiency with a pion in the central arms as a function of the pion's momentum. The left panel has no additional requirement and the right panel also requires a π^0 or photon with energy greater than 12 GeV in the MPC.

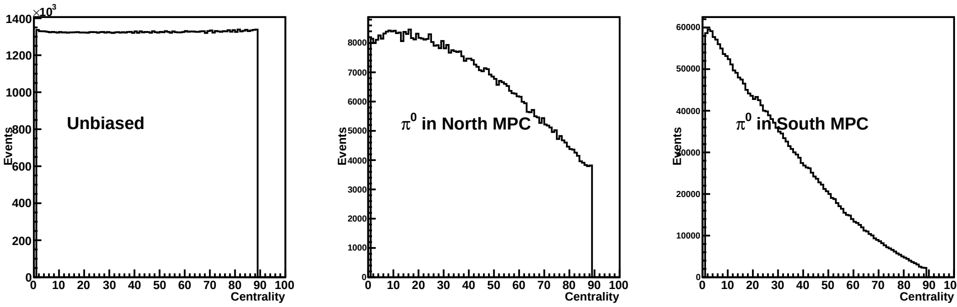

Figure 5.23: The left panel shows the unbiased centrality distribution, the middle panel the centrality distribution of events containing a π^0 with p_{T} between 0.75 and $1\mathrm{GeV}/c$ in the North MPC, and the right panel the distribution from events with a π^0 in the South MPC.

Chapter 6

Run 8 Results

6.1 Comparing d+Au and p+p

To quantify the modification of the single particle spectra from d+Au compared to binary collision scaled p+p we used the nuclear modification factor R_{dAu} (see section 4.2), in a similar vein we here introduce the pair nuclear modification factor J_{dAu}:

$$J_{dAu}(a,b) = \frac{N_{dAu}^{ab,\Delta\phi=\pi} / N_{dAu}^{events}}{< N_{coll} >_{dAu} \, N_{pp}^{ab,\Delta\phi=\pi} / N_{pp}^{events}} \tag{6.1}$$

where a and b are the two particles from which the correlation is made, and the superscript $\Delta\phi = \pi$ indicates that the pair ab stems back to back from the same interaction (although in practice they do not have $\Delta\phi$ identically π and the correlated yield is measured using the process described in section 5.5). This quantity can be calculated independently for each momentum bin and event class in which correlated yields are measured.

In addition to J_{dAu}, we may consider the ratio of the correlated yield in d+Au *per trigger* divided by the same quantitiy in p+p, I_{dAu}:

$$I_{dAu}(a,b) = \frac{N_{dAu}^{ab,\Delta\phi=\pi} / N_{dAu}^{a}}{N_{pp}^{ab,\Delta\phi=\pi} / N_{pp}^{a}} \tag{6.2}$$

where we call particle a the trigger particle and b the associate or partner particle. The choice of which particle to call the trigger and which the partner is somewhat arbitrary and will depend on the particulars of the measurement and the physics being sought. J_{dAu} and I_{dAu} are related to each other by the single particle nuclear modification factor of the trigger particle:

$$J_{dAu}(a,b) = I_{dAu}(a,b) R_{dAu}(a) = I_{dAu}(b,a) R_{dAu}(b) \tag{6.3}$$

It is important to notice that I_{dAu} is not necessarily invariant across the choice of the trigger; whereas for a given correlation function there is only one definition of J_{dAu} there are two different ways to define I_{dAu}, i.e. I_{dAu}(a,b) does not equal I_{dAu}(b,a) but rather:

$$I_{dAu}(a,b) = I_{dAu}(b,a)\frac{R_{dAu}(b)}{R_{dAu}(a)} \tag{6.4}$$

The simplest interpretation of I_{dAu} is that the number of triggers measured is a good proxy for the number of jets measured, however as equation 6.4 shows we must be careful of how we consider a measured jet in the case where R_{dAu}(a) $\neq$ R_{dAu}(b).

6.2 J_{dAu}

In equation 6.1 we defined J_{dAu} for an ideal detector, taking into account the necessary corrections we have:

$$J_{dAu}(a,b) = \frac{N_{dAu}^{ab,\Delta\phi=\pi}/N_{dAu}^{events}}{< N_{coll} >_{dAu} N_{pp}^{ab,\Delta\phi=\pi}/N_{pp}^{events}} \frac{C_{BBC}^{dAu}}{C_{BBC}^{pp}} \frac{R_{dAu}^{signal}\epsilon_{pp}^{a}\epsilon_{pp}^{b}}{R_{pp}^{signal}\epsilon_{dAu}^{a}\epsilon_{dAu}^{b}} \tag{6.5}$$

where C_{BBC}^{dAu} and C_{BBC}^{pp} are as defined above in sections 5.2.1 and 5.2.2, $\epsilon^{a,b}$ refer to the efficiencies of the two particle types as discussed in sections 5.3.2 and 5.4.2, and R^{signal} is the fraction of measured π^0s that are signal as in Tables 5.5 and 5.6. This quantity is calculated in the four centrality bins, two π^0 p_{T} bins, and three charged hadron p_{T} bins mentioned above. Figure 6.1 shows J_{dAu} as a function of the p_{T} of the midrapidity charged hadron in four centrality bins, for both d-going side and Au-going side π^0s with p_{T} between 0.75 and 1 GeV/c, and Figure 6.2 is the same for $1.0<\mathrm{p}_{\mathrm{T}}^{\pi^0}<2.0$. There is an additional 12% overall scale uncertainty that is not plotted in the figures. In figure 6.3 we average over the midrapidity charged hadron momentum and plot J_{dAu} as a function of $\langle N_{coll}\rangle$.

We observe that $J_{dAu}(\pi^0_{d-going},\mathrm{h}^{\pm}_{midrapidity})$ is consistently less than one and perhaps approaching unity in the most peripheral centrality bin, indicative of a suppression in correlated pairs in d+Au compared to binary collision scaled p+p. On the other hand, $J_{dAu}(\pi^0_{Au-going},\mathrm{h}^{\pm}_{midrapidity})$ seems to be consistent with unity.

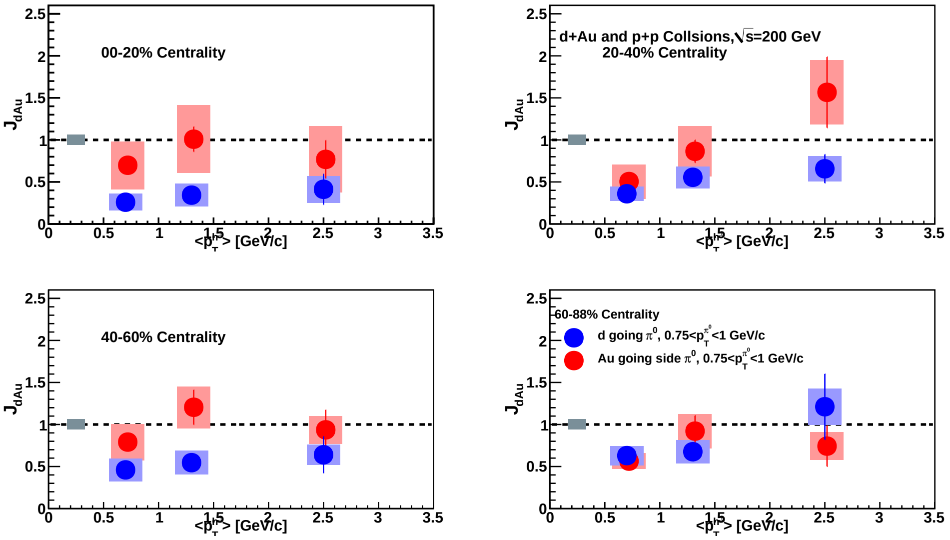

Figure 6.1: J_{dAu} for d-going side π^0 – midrapidity hadron correlations (blue) and Au-going side π^0 – midrapidity hadron correlations (red) in four centrality bins as a function of $\mathrm{p}_\mathrm{T}^{h^\pm}$ for $0.75<\mathrm{p}_\mathrm{T}^{\pi^0}<1.0$.

6.3 I_{dAu}

Bearing in mind the necessary detector efficiency corrections we measure I_{dAu} as:

$$I_{dAu}(a,b) = \frac{N_{dAu}^{ab,\Delta\phi=\pi}/N_{dAu}^{a}}{N_{pp}^{ab,\Delta\phi=\pi}/N_{pp}^{a}} \frac{\epsilon_{pp}^{b}}{\epsilon_{dAu}^{b}} \tag{6.6}$$

We assign the forward or backward π^0 to be the trigger particle (‘a’ in equation 6.6 above) and the midrapidity hadron the partner particle (b). I_{dAu} in four centrality bins as a function of the partner hadron p_T is plotted for the lower trigger momentum in Figure 6.4 and in Figure 6.5 the higher trigger momentum.

Normalizing the correlated yields by the number of forward or backward π^0s, reverses the trend observed in J_{dAu}; $I_{dAu}(\pi^0_{d-going},\mathrm{h}^\pm_{midrapidity})$ is greater than one and greater than $I_{dAu}(\pi^0_{Au-going},\mathrm{h}^\pm_{midrapidity})$. Figure 6.6 summarizes the trends in centrality by plotting I_{dAu} as a function of $\langle N_{coll}\rangle$ where we have averaged over the midrapidity charged hadron momentum bins.

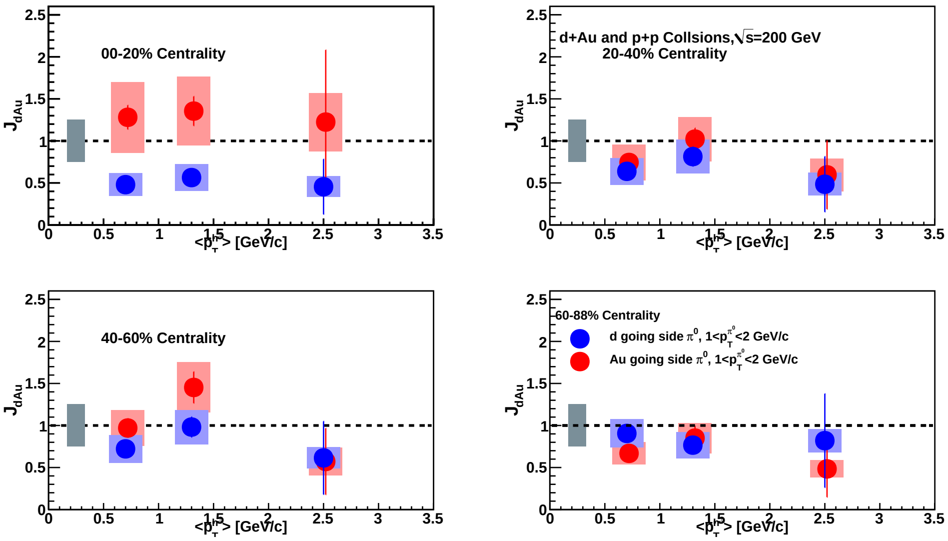

Figure 6.2: J_{dAu} for d-going side π^0 – midrapidity hadron correlations (blue) and Au-going side π^0 – midrapidity hadron correlations (red) in four centrality bins as a function of $\mathrm{p}_{\mathrm{T}}^{h^\pm}$ for $1.0 < \mathrm{p}_{\mathrm{T}}^{\pi^0} < 2.0$.

6.4 Width of Correlated Signal

Along with the correlated yield which is the integral of the gaussian component of the correlation function fit, we consider the width of the gaussian component. Figure 6.7 shows the widths averaged over the midrapidty hadron p_{T} bins as a function of $\langle N_{coll} \rangle$ for each π^0 p_{T} bin. In the lower π^0 p_{T} bin there is significant separation of the d-going side and Au-going side correlation widths; somewhat surprisingly the width in p+p is even larger although the uncertainties are large. In the higher π^0 p_{T} bin it is difficult to see any significant trends.

6.5 R_{dAu}

From equation 6.3 it is clear that we can calculate R_{dAu} from J_{dAu} and I_{dAu}, i.e. R_{dAu} is identically the ratio of normalizing per event and scaling by the number of binary collisions and normalizing by the number of measured π^0 triggers. R_{dAu} of d-going and Au-going side π^0s are presented as function of the mean number of binary collisions in Figure 6.8. R_{dAu}(d-going side)

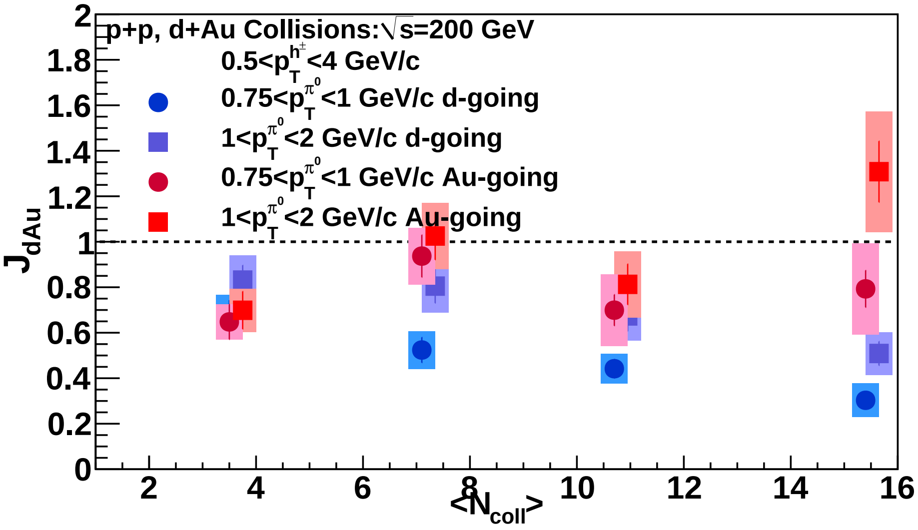

Figure 6.3: J_{dAu} for d-going side π^0 – midrapidity hadron correlations (blue) and Au-going side π^0 – midrapidity hadron correlations (red) in two π^0 p_{T} bins, averaged over the hadron p_{T} as a function of $\langle N_{coll} \rangle$.

is clearly suppressed and increasingly so in more central collisions, whereas R_{dAu}(Au-going side) shows the opposite trend and is enhanced in more central collisions and at lower p_{T}.

6.6 Uncorrelated Yield

6.6.1 Reduction Factor

To study the underlying event we may define the "reduction factor" of the midrapidity yield, due to a forward (backward) π^0 as midrapidity yield per event in minimally biased events divided by the yield per event for events in which there was a forward (backward) π^0 measured (this quantity is suggested by [90]).

$$R = \frac{N^{mid}/N^{min\ bias}_{events}}{N^{mid}/N^{\pi^0_{fwd}}_{events}} \tag{6.7}$$

One should note that in this definition the number of events in which there is a forward π^0 is approximately the same as the number of π^0s measured. To isolate the uncorrelated component, the correlated component of the midrapidity

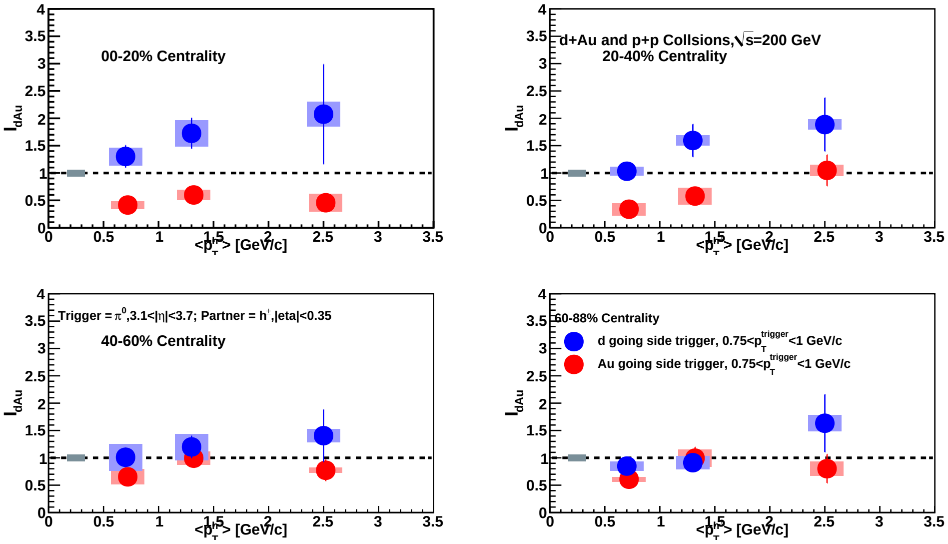

Figure 6.4: I_{dAu} for d-going side π^0 triggers – midrapidity hadron partners (blue) and Au-going side π^0 triggers – midrapidity hadron partners (red) in four centrality bins as a function of $\mathrm{p}_{\mathrm{T}}^{h^{\pm}}$ for $0.75<\mathrm{p}_{\mathrm{T}}^{\pi^0}<1.0$.

yield is subtracted in the denominator. The reduction factor is calculated in each centrality class independently as a function of the forward (backward) π^0 p_{T} and the midrapidity hadron p_{T}. It is pretty constant as a function of the midrapidity hadron p_{T}, and so is fit to a flat line for p_{T} <3.5 GeV/c. The reduction factors are plotted for forward and backward π^0 events in Figure 6.9. The reduction factors are, just slightly under unity indicating that there is not significant modification in the soft particle production at midrapidity under a forward (backward) π^0 condition compared with no such requirement. This is in disagreement with the qualitative predicitons in [90].

6.6.2 Comparing Correlated and Uncorrelated Yield

It is important to distinguish the trends observed in the azimuthally correlated yields from the uncorrelated production. Especially considering the fairly low p_{T} of the forward (backward) π^0s measured, we would like to distinguish the soft particle production from the observations in the correlated yield . Whereas we defined I_{dAu} in equation 6.2 using the *correlated* pairs per trigger, $N^{ab,\Delta\phi=\pi}/N^a$, we may define an analogous quantity for uncorrelated pairs N^{ab}/N^a that measures the forward (backward) – midrapidity pair yield

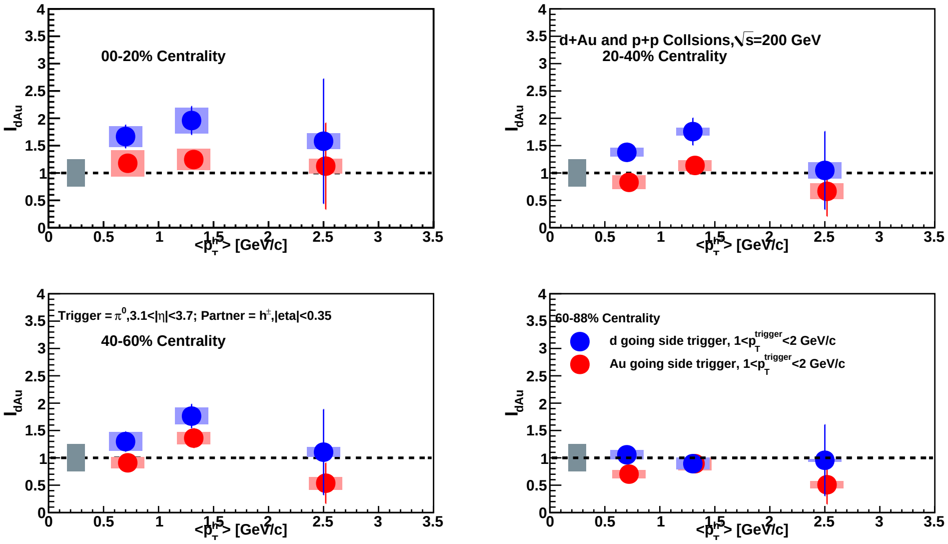

Figure 6.5: I_{dAu} for d-going side π^0 triggers – midrapidity hadron partners (blue) and Au-going side π^0 triggers – midrapidity hadron partners (red) in four centrality bins as a function of $\mathrm{p}_\mathrm{T}^{h^\pm}$ for 1.0<$\mathrm{p}_\mathrm{T}^{\pi^0}$ <2.0 .

without the requirement of azimuthal correlation. For this quantity to truly be *un*correlated, as in the reduction factor above, we subtract from N^{ab} the contribution of the azimuthally correlated pairs, $N^{ab,\Delta\phi=\pi}$.

To spot these differences we examine the ratio of both the correlated and uncorrelated yields in the d-going side triggered case divided by the same in the Au-going side case. By analogy to I_{dAu}, we may define I_{FB}:

$$I_{FB}(a,b) = \frac{N^{ab,\Delta\phi=\pi}_{d-going}/N^{a}_{d-going}}{N^{ab,\Delta\phi=\pi}_{Au-going}/N^{a}_{Au-going}} \tag{6.8}$$

and its uncorrelated corollary:

$$I'_{FB}(a,b) = \frac{N^{ab}_{d-going}/N^{a}_{d-going}}{N^{ab}_{Au-going}/N^{a}_{Au-going}} \tag{6.9}$$

where particles a and b are again π^0s in the MPCs and charged hadrons at midrapidity, respectively. These are plotted together integrated over the midrapdity hadron p_T as a function of the mean number of binary collisions in Figure 6.10.

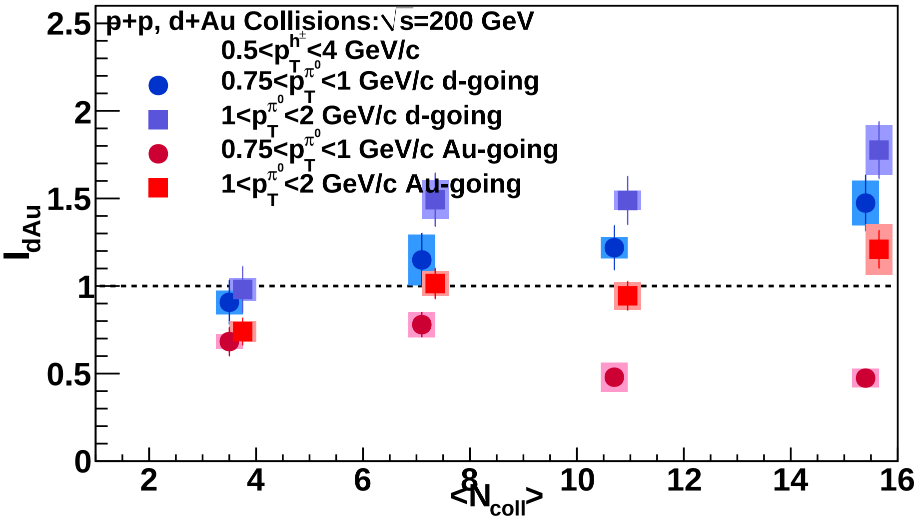

Figure 6.6: I_{dAu}(d-going side π^0,midrapidity hadron) in blue and I_{dAu}(Au-going side π^0,midrapidity hadron) in red in two π^0 p_{T} bins, averaged over the hadron p_{T} as a function of $\langle N_{coll} \rangle$.

In the fairly low p_{T} range of the forward (backward) π^0s, hadron production is sensitive to soft physics processes. Soft hadron production is decreased (increased) at forward (backwards) rapidities, and may explain some of the measured R_{dAu} shown in Figure 6.8. However, in the two particle measurements for which we select pairs based on the $\Delta\phi$ between the forward (backward) π^0 and midrapidity hadron we are selecting predominantly from hard physics hadron production. Figure 6.10 clearly shows that the very different trends observed in the d-going and Au-going side triggered I_{dAu} in Figures 6.4 and 6.5 are indeed due to modification of hard physics processes and not consequences of soft physics processes in the underlying event.

6.7 Systematic Uncertainty Summary

The analysis described in Chapter 5 includes many steps in which it was necessary to rely on measurements, simulations, and assumptions which we are unable to claim full certainty on. The nature of the uncertainty in the analysis determines how it propagates into the measurements presented in this chapter. Broadly, there are three relevant categories of uncertainty: inde-

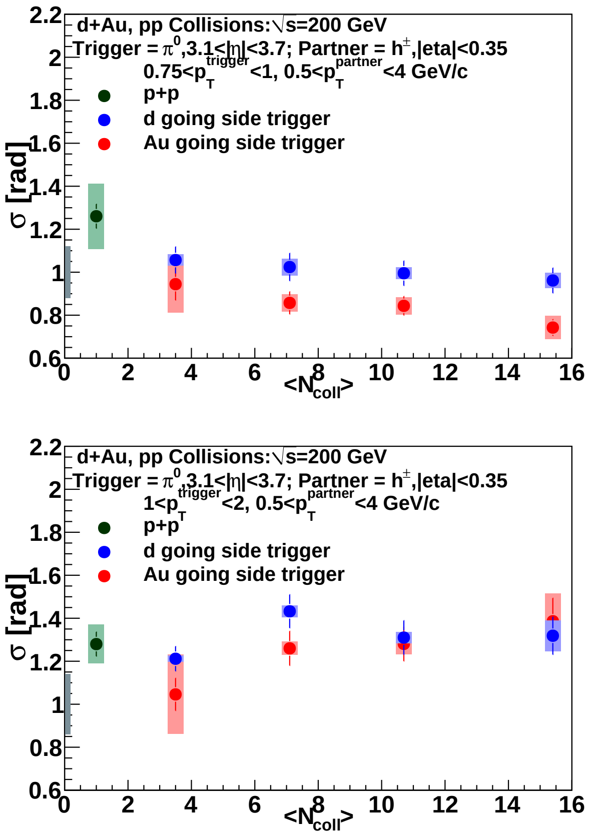

Figure 6.7: The width of the correlated signal in $\Delta\phi$ for $0.75<\mathrm{p}_{\mathrm{T}}^{\pi^0}<1.0$ and $1.0<\mathrm{p}_{\mathrm{T}}^{\pi^0}<2.0$ on the top and bottom, respectively.

pendent, correlated, and constant. By "independent of x" we mean that the uncertainty is completely uncorrelated point by point on considered on the axis of x, similar to statistical uncertainties. Correlated uncertainties refer to those which may be different point by point on a given axis, but are correlated (or anti-correlated), i.e. when looking for a trend in the data or comparing it to other data or a prediction it is only meaningful to allow variation within the uncertainty of all the points considered simultaneously. A constant uncertainty is one which is the same point by point along the axis on which it is constant.

The main sources of uncertainty are:

- p+p Cross Section, Event Trigger Efficiency, and Centrality

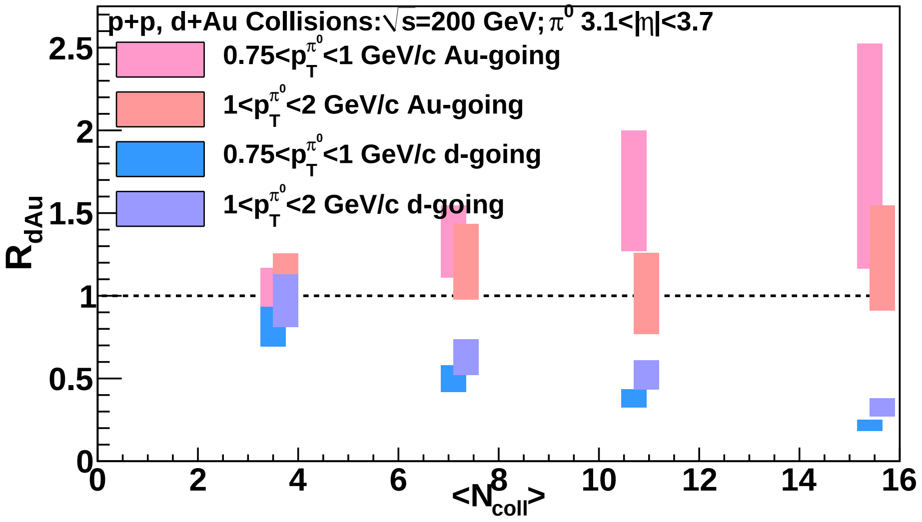

Figure 6.8: R_{dAu} for d-going and Au-going side π^0s in two p_T bins as a function of $\langle N_{coll}\rangle$. There is additionally an unplotted overall scale uncertainty of 12%. The higher p_T points are shifted on the x-axis for visual clarity.

- MPC π^0 Efficiency , and Background
- Correlation Function Fitting

6.7.1 p+p Cross Section, Event Trigger Efficiency, and Centrality

As discussed in section 5.2.2 the correction to the yield per event from p+p collisions is based on measurement of the total cross section, the fraction of the cross section detected by the BBC, and the BBC bias due to the requirement of measuring a particle in the detectors other than the BBC. The uncertainty on this correction is 9.7%, and is applicable to yield per event quantities, namely J_{dAu} and R_{dAu}. As it stems from p+p collisions It is constant across all d+Au axes, and is also constant in p_T. The d+Au analogue of this correction, C$_{BBC}$ as in Table 5.1, has associated uncertainty which is the same across momentum axes but is independently calculated in each centrality bin.

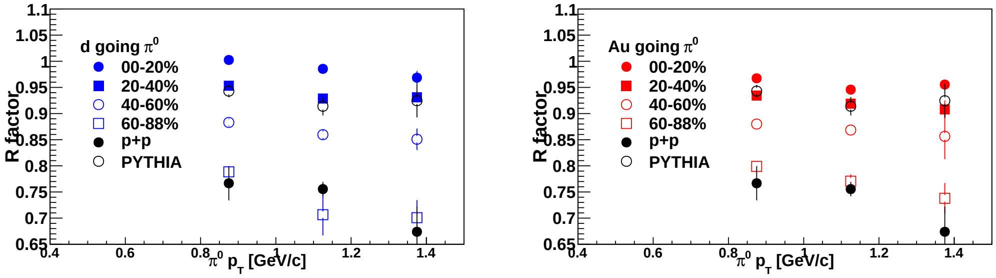

Figure 6.9: The reduction factors as a function of the d-going side π^0 p_T on the left and of the Au-going side π^0 p_T on the right. For reference the same quantity from p+p collisions and a PYTHIA calculation is plotted.

6.7.2 MPC π^0 Efficiency , and Background

π^0 Efficiency

The π^0 efficiencies shown with their associated uncertainties in Table 5.7 are relevant for J_{dAu} and R_{dAu}. The uncertainties listed are based chiefly on varying the input spectrum of the π^0s embedded into real events for reconstruction - this variation is the same regardless of which event class they are embedded into. However, because the uncertainties also address the other limitations of the efficiency calculation as well (statistical and any inherent differences between simulated and real particles) and further it is not clear that the real background they are embedded into is unaffected by the input spectrum. We therefore consider them uncorrelated in π^0 p_T and not canceling in the J_{dAu} and R_{dAu} ratios.

π^0 Background

The backgrounds inside the π^0 sample due to either random combinatorics or correlated background and the associated uncertainties are shown in Tables 5.5 and 5.6. The dominant source of the background are random combinatorics that are well accounted for using mixed events. The residual background is modeled without knowledge of its true shape but is constrained by the procedure described in section 5.4.2. These uncertainties propagate into the J_{dAu}, and R_{dAu} ratios.

The correction for the effect of contamination in the π^0 sample on the measured correlated yield is taken with a full uncertainty as discussed in section 5.5.4 and is applicable to J_{dAu}, I_{dAu}, and the measured widths. This is taken

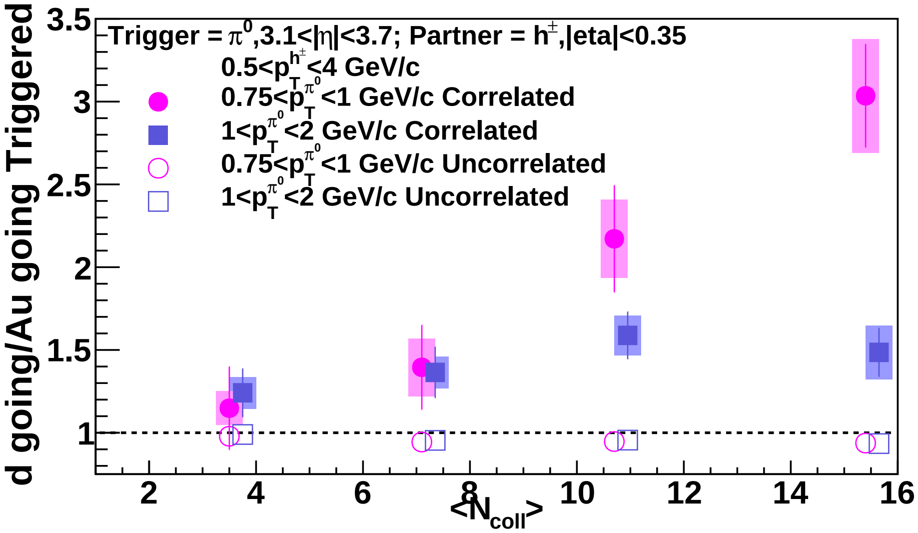

Figure 6.10: I_{FB} and I'_{FB} (see text) integrated over the midrapidity hadron $p_{\rm T}$ for two π^0 $p_{\rm T}$ bins as a function of $< N_{coll} >$. The higher π^0 $p_{\rm T}$ points are shifted on the x-axis for visual clarity.

as uncorrelated across event classes because the correction itself is taken from data measured independently in different event classes. For the same reason it is at least partially uncorrelated as a function of $p_{\rm T}$. In the ratios we make the assumption that deviation of the true values from the central values as approximated using the sidebands is correlated between p+p and d+Au, so the uncertainty partially cancels. To account for this we propagate only the d+Au uncertainty into J_{dAu} and I_{dAu}. Simlarly, for the I_{FB} ratio we propagate only the larger of the uncertainties from the numerator and denominator.

6.7.3 Correlation Function Fitting

In section 5.5.3 we discussed the uncertainty associated with the extraction of the fit parameters in the correlation functions. This uncertainty propagates into J_{dAu}, I_{dAu}, and the widths. As mentioned there, this uncertainty is common across event classes and the midrapidity hadron $p_{\rm T}$. Because the simultaneous fit is across different π^0 $p_{\rm T}$ bins, if there is a systematic bias the common background level used must be between the true levels of the lower and higher π^0 $p_{\rm T}$ bins, i.e. if the value used for $\rm b_0$ is too high for the lower $p_{\rm T}$ bin it is too low for the higher $p_{\rm T}$ bin. Therefore, the uncertainty is anti-correlated across different π^0 p_{T} bins within the same event class. The uncertainties propagated into J_{dAu} and I_{dAu} are 6% for the 0.75<$\mathrm{p}_{\mathrm{T}}^{\pi^0}$ <1.0 GeV/c and 25% for the 1.0<$\mathrm{p}_{\mathrm{T}}^{\pi^0}$ <2.0 GeV/c bin. Propagated into the widths the uncertainties are 12% and 14% for the lower and higher $\mathrm{p}_{\mathrm{T}}^{\pi^0}$ bins, respectively.

Chapter 7

Run 8 Discussion

To glean insight into the relevant physics we may consider, in different physics scenarios, the implications of the three quantities that compare the yield measured in d+Au to p+p: R_{dAu}, J_{dAu}, and I_{dAu}. In particular we compare the measured d-going side data to some relevant models.

7.1 Color Glass Condensate

Following from DIS results at a small enough x, gluons should begin to overlap. The overlapping gluons will fuse, reducing their density at lower x and increasing it at higher x corresponding to an suppression of the d+Au hadron yield at forward rapidity and enhancement at backward rapidity(see section 1.2.4). This is consistent with the R_{dAu} measured here as well as previously (see Figure 1.11). However, as discussed above in section 6.6.2, it may be difficult to distinguish the suppression (enhancement) of forward (backward) R_{dAu} due to a modification at the parton level from soft physics phenomena.

In forward (backward)−midrapidity two particle correlation measurements a CGC picture also predicts suppression in d+Au compared to p+p for the forward (but not backward)−midrapidity pair yield [51]. This is due to a decorrelation of the back to back jets in which one of them scatters off the dense color medium rather than fragmenting normally. In this case we expect a smaller wider correlated signal in forward−midrapidity correlations compared to backward−midrapidity in d+Au and forward or backward−midrapidity correlations in p+p.The suppression of the d-going−midrapidity correlated pair yield is observed in J_{dAu} as shown in Figures 6.1-6.3.

Just as the decorrelation due to scattering on the dense medium reduces the total pair yield it should also somewhat widen the observed correlated signal. The widths measured in this analysis do not support this prediction, as shown in Figure 6.7. For forward and backward π^0s with p_T between 0.75 and 1 GeV/c the d-going side−midrapidity correlations do seem to be significantly wider than the Au-going side−midrapidity correlations. This is consistent with CGC model predictions, however, the p+p correlated signals are wider still. The discrepancy to the p+p case may be an experimental outlier; the difference between the p+p point and the Au-going side−midrapidity correlation case is approximately 2σ (using only the correlated uncertainty of the d+Au correlations, i.e. moving along this uncertainty does not impeach the significance of the difference between the d-going side−midrapidity correlation and Au-going side−midrapidity correlation widths). For π^0s with p_T between 1 and 2 GeV/c the widths are all roughly constant within the experimental uncertainty. The systematic uncertainties are large due to the sensitivity of the width to the uncorrelated background level so it is difficult to draw any conclusions in the higher momentum case.

To further examine the data in the CGC picture we turn to the I_{dAu}. Although the forward π^0 single particle spectra are strongly suppressed in I_{dAu}(d-going,midrapidity) we are triggering on the rare case where there *was* a d-going side π^0. Conversely, I_{dAu}(Au-going,midrapidity) uses a trigger from the enhanced backward side π^0 yield. Even in an event in which the forward π^0 is detected there is still a dense color medium present. When we do measure the forward π^0 it has already lost some momentum, relative to the original jet, to the CGC. The momentum of the midrapidity jet must therefore balance not only the measured π^0, but rather the full forward jet momentum. This is essentially a shift in the π^0's fraction of the total jet p_T (z_T), relative to the similar correlations with a Au-going side trigger π^0 or in p+p collisions. In the case without a CGC to scatter off, the measured π^0 will typically have higher z_T than the case where the CGC balances some of the momentum of the jet. So for a trigger particle of the same momentum, the *total* jet momentum is on average higher for the measured d-going side π^0 at a given p_T compared to the same p_T π^0 measured in p+p collisions. Therefore, I_{dAu} will be enhanced as more midrapidity recoil particles are needed to balance the forward jet whose momentum is contained in the CGC as well as the measured π^0 in the forward triggered d+Au case than the p+p case. For the same reason we'd expect that the midrapidity recoil hadron correlated yield would be higher with a d-going side trigger compared to a Au-going side trigger. These trends are observed as shown in Figures 6.4−6.6 and 6.10. It is worth noting that the presence of a CGC formed in the high gluon density region of the Au nucleus does not offer any predictions for the I_{dAu}(Au-going side,midrapidity) which is sensitive to high x from the Au nucleus, and the suppression observed there.

7.2 Parton Multiple Scattering

In [52] the authors present a model of coherent multiple scattering of several nucleons. They predict the single and two particle nuclear modification factors, R_{dAu} and J_{dAu} (in [52] J_{dAu}(a,b) is referred to as $R^{a,b}_{dAu}$) of forward and forward−midrapidity particles. One should note that although they are similar the model predictions are not for particles with identical kinematic characteristics. In the model the most central collisions are calculated at b = 3 fm, and the most peripheral at b = 6.8 fm. In Figure 7.1 the J_{dAu} model predictions are shown alongside the data. Within the uncertainties the agreement between model and data is pretty good in J_{dAu}. However, if we consider the single particle suppression shown in the forward π^0 R_{dAu} the agreement is substantially worse as shown in Figure 7.2. The data indicate that the d-going side single particle spectra is suppressed more strongly than the two particle forward−midrapidity correlated yield, but in the model the single particle spectra is suppressed at approximately the same level as the two

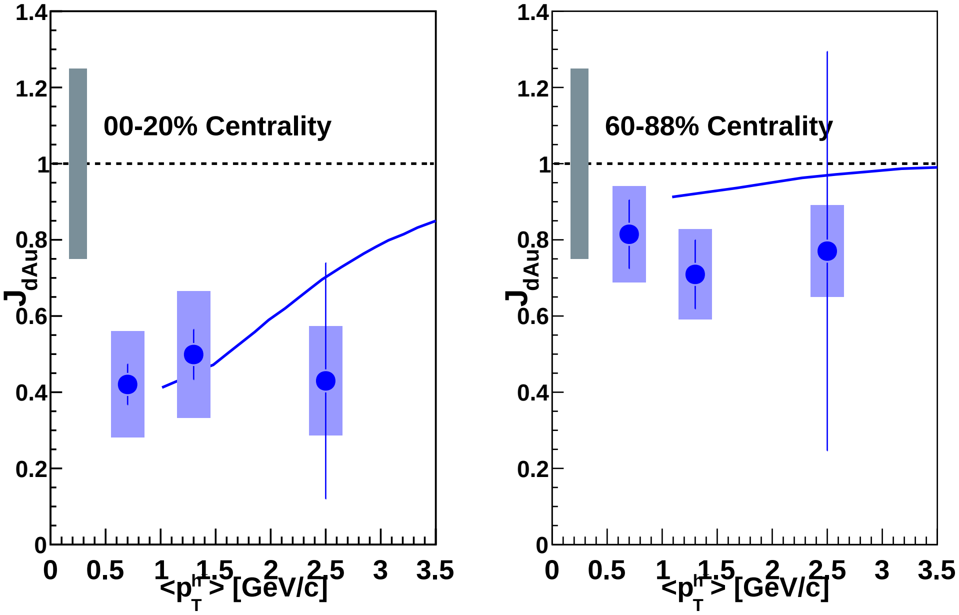

Figure 7.1: J_{dAu} for d-going side π^0 – midrapidity hadron correlations shown with the predictions from [52]. The forward particle in the model predictions has y=3.0 and p_{T}=1.5, whereas in the data 3.1< η <3.7 and $< p_{\mathrm{T}} >$≈1.1.

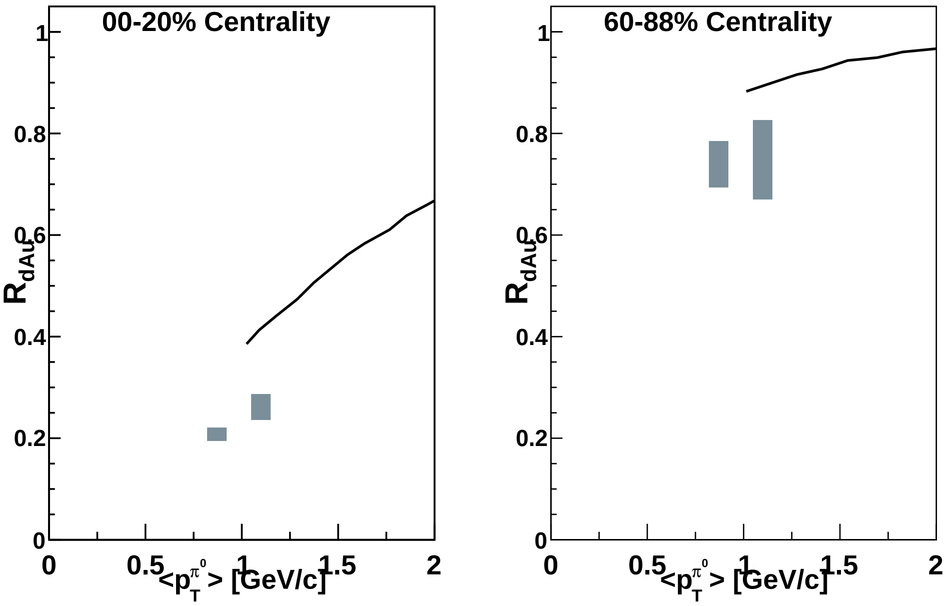

Figure 7.2: R_{dAu} for d-going side π^0s shown with the predictions from [52]. The forward particle in the model predictions has y=3.0, whereas in the data 3.1< η <3.7.

particle correlated yield. In other words the I_{dAu}(d-going side,midrapidity) is underestimated. To see this explicitly we may calculate I_{dAu} from the model predictions of $J_{dAu}$and R_{dAu} and compare with the data as shown in Figure 7.3. Although the agreement in the peripheral case is quite good (of course this is essentially due to the model overprediciting both J_{dAu} andR_{dAu}, as shown in Figures 7.2 and 7.1, by the same amount), we see significant disagreement in the central case where the experimental uncertainties allow us to discriminate. This suggests that perhaps coherent multiple parton scattering is an insufficient mechanism to explain the data.

7.3 Forward vs Backward

The two directions in which the MPC π^0s are measured probe very different x regions of the Au nucleus. As starkly demonstrated in Figure 6.8, they have very different single particle production rates - the strong suppression

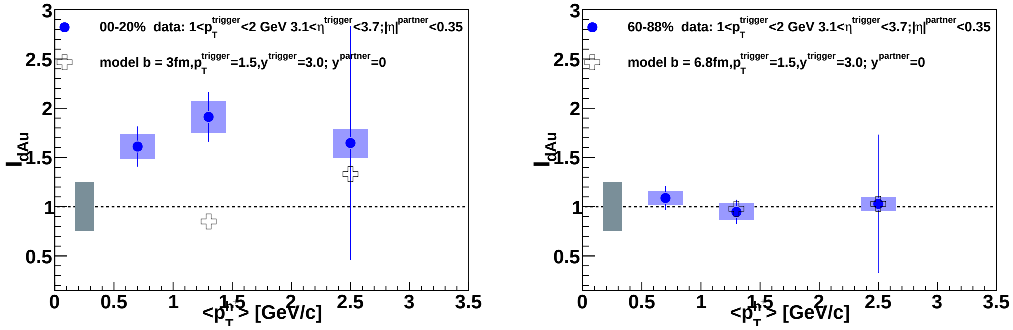

Figure 7.3: I_{dAu} for d-going side π^0 – midrapidity hadron correlations shown with the predictions from [52]. The forward particle in the model predictions has y=3.0 and p_T=1.5, whereas in the data 3.1< η <3.7 and $< p_\mathrm{T} >\approx$1.1.

at forward rapidity, is replaced by some enhancement at backward rapidity. The two particle correlations give us a more complete look at the physics processes in the two regions. Using equation 5.1 and taking the measured particle kinematics as though they were the parton's, we may estimate the backward-midrapidity correlations to probe approximately 0.15< x <0.19, and the forward-midrapidity to cover 0.04< x <0.012 (note that where we integrate across multiple p_T bins the statistics heavily favor the lower p_T and consequently lower x). The difference in the two particle production rates where the second particle is at midrapidity is less dramatic across centrality as seen in Figure 6.3, and it is perhaps more instructive to consider the *conditional* production rates as shown in Figures 6.6 and 6.10. Although there are more of them, when a backward π^0 is measured there are fewer midrapidity particles azimuthally correlated with it. This is not the case if we consider the bulk production of uncorrelated particles as shown in the open I'_{FB} points of Figure 6.10. The underlying event is at most very slightly modified once a forward *or* backward π^0 is required.

7.4 Conclusions

In this analysis we have mapped a significant portion of the x distribution of Au nucleus. This may be seen in the larger context of attempting to understand the full phase space of nuclear and partonic physics processes. We have here presented results at lower and higher x regions of the Au nucleus, and further x regions are available for study in the RHIC data.

In this vein, concurrent to this analysis, a parallel analysis measured two particle correlations in which both particles are in the forward d-going side MPC probing the lowest x available to PHENIX [91] shown in Figure 7.4, as well as a similar analysis from the STAR collaboration[92] shown in Figure 7.5. The measurements probe $x \approx 5 \times 10^{-4}$ (using the collinear approximation as above in equation 5.1). At this lower x we expect any decorrelation due to a CGC or coherent interactions to be still stronger than in the forward - midrapidity case. Both the PHENIX and STAR data show a dramatic qualitative broadening of the away side peak in central d+Au compared to peripheral d+Au and p+p. CGC models predicted and describe this qualitative change well [93, 94]. We must note that the description of the uncorrelated level may not be trivial, and is of sufficient experimental technical difficulty that it is not presented in the above analyses. Despite this caveat, the significant modification of the away side peak seems to imply decorrelation which is a strong indicator of some level of collective parton behavior in the scattering interaction.

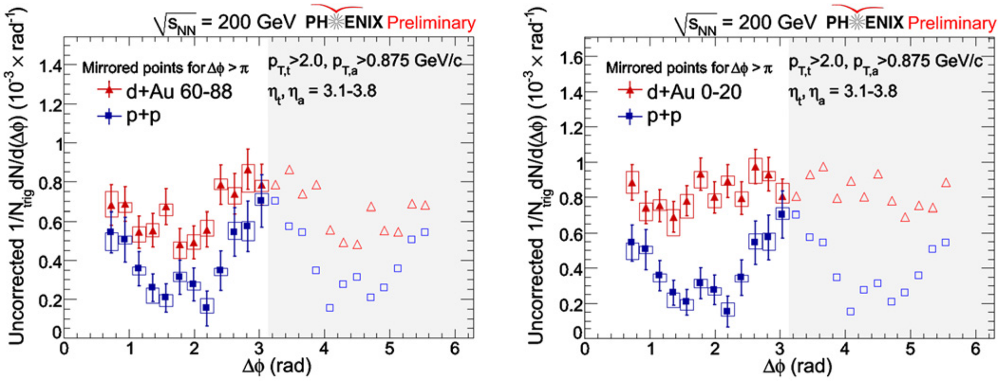

Figure 7.4: Azimuthal angle correlations for two forward particles in the d-going side MPC. One particle is a reconstructed π^0,0.875<p_T <2.0 GeV/c, and the other is a single electromagnetic cluster dominated by π^0s with p_T>2.0 GeV/c. On the left the correlation per cluster from most peripheral d+Au collisions is shown and on the right from most central, both overlaid with p+p. From [91].

These measurements taken together suggest a significant trend in x of the Au nucleus. In this thesis we have presented clear differences in particle production at moderate x as measured in backward Au-going side rapidity and lower x particle production measured in forward d-going side rapidity. The two

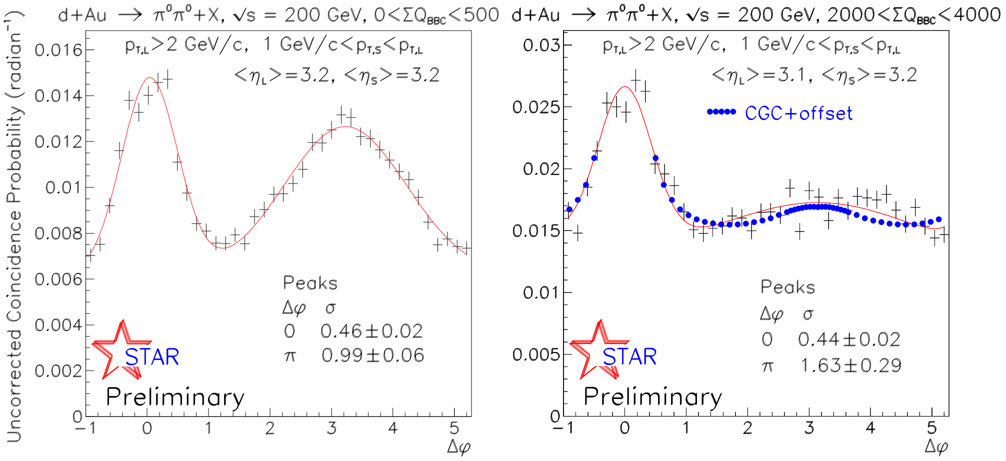

Figure 7.5: Coincidence probability in $\Delta\phi$ for two forward (d-going side) π^0s measured by the STAR experiment from peripheral d+Au collisions on the left and central collisions on the right. For the central case a CGC prediction is shown from [93].

particle correlations allow us to state with confidence that we are observing more than just soft bulk phenomena. There is very little modification observed in the soft uncorrelated particle production when comparing the backward-midrapidity and forward-midrapidity cases. Further the forward (backward) π^0 requirement doesn't appear to strongly affect the uncorrelated production. By contrast, the suppression of the correlated production at forward rapidity compared to the backward rapidity and p+p, suggests that CGC or other multi-parton effects may be relevant at the lower x. This is also suggested by the apparent broadening of the widths in the low x backward-midrapidity correlations compared to the high x forward-midrapidity correlations. As we probe even lower in x using correlations of two particles both in the d-going side rapidity, we observe still stronger signs of CGC or other coherent parton characteristics in the qualitative decorrelation of the away-side jet peak.

Looking forward, the planned Electron-Ion Collider [95] promises to be a powerful investigative tool into the nucleus, in which the range of x and Q^2 available will be unprecedented. The longitudinal nuclear structure function at small x as well as the gluon distribution will be accessible with greater precision than ever before. The planned Electron-Ion Collider facility will be a major step forward in understanding QCD and its evolution in extreme conditions.

One of the most exciting frontiers in our study of cold nuclear matter is the prospect to observe gluon saturation. At sufficiently low x, an eventual saturation of the gluons is difficult to escape given the theory and experiment to date. The data presented here, in the context of the entire body of cold nuclear matter studies at RHIC, are more consistent with a gluon saturation state in the Au nucleus than with the more mundane nuclear process calculations. Although the field can not yet declare a discovery of this new state of matter, these data hint that we are indeed at or close to the threshold for color saturation. This scenario compels experimental studies to continue the search both with higher luminosity and lower x at RHIC as well as the future Electron-Ion Collider.

We have here offered the first look at forward *and* backward rapidity separated correlations, beginning to fill in the gaps of our understanding of the nucleus and its QCD underpinnings; we hope that the investigations continue productively.

Part IV

Appendices

Appendix A

Run 3 Data Tables

p_T (GeV/c)	R_{dAu}	Statistical Uncertainty	Systematic Uncertainty
0.65	0.650262	0.00170411	0.0208239
0.75	0.673801	0.00206754	0.0215758
0.85	0.722339	0.00259466	0.0231286
0.95	0.747055	0.00313973	0.02392
1.05	0.779902	0.00380401	0.0249712
1.15	0.83354	0.00473263	0.0266879
1.25	0.879426	0.0057559	0.0281582
1.35	0.921612	0.00694741	0.029508
1.45	0.927713	0.00796327	0.0297036
1.55	0.942112	0.00932838	0.030166
1.65	1.01833	0.0115307	0.0326056
1.75	1.01948	0.0130644	0.0326445
1.85	1.07781	0.0157305	0.0345111
1.95	1.0896	0.017969	0.0348911
2.05	1.08411	0.0201171	0.0347143
2.15	1.07625	0.0222511	0.034462
2.25	1.18303	0.0280844	0.0378917
2.35	1.16836	0.0308991	0.0374239
2.45	1.16512	0.0346391	0.0373154
2.55	1.26779	0.0430438	0.0406116
2.65	1.19161	0.0436794	0.0381651
2.75	1.17345	0.0476516	0.0375864
2.85	1.24616	0.0568533	0.0399281
2.95	1.33613	0.0705714	0.0428089
3.0969	1.16697	0.0468513	0.037404
3.30172	1.35778	0.0699776	0.0435429
3.50069	1.31261	0.0807919	0.0421282
3.68198	1.31589	0.0970317	0.0422594
3.90549	1.22188	0.101631	0.0392624
4.13245	1.20775	0.106404	0.0390378
4.43979	1.15495	0.127418	0.037551
4.69036	1.51277	0.258451	0.0511606
5.11318	1.07257	0.168918	0.0391998
6.47622	0.852054	0.192132	0.0397448

Table A.1: Data points for centrality class A R_{dAu}. There is an additional systematic uncertainty of 12.8% common to all points.

p_T (GeV/c)	R_{dAu}	Statistical Uncertainty	Systematic Uncertainty
0.65	0.696453	0.00190172	0.0223104
0.75	0.715558	0.00228462	0.0229198
0.85	0.762342	0.00284486	0.0244174
0.95	0.780512	0.00340501	0.0249984
1.05	0.809657	0.00409495	0.0259305
1.15	0.862639	0.00507083	0.0276279
1.25	0.899058	0.00609115	0.028794
1.35	0.940238	0.00732901	0.0301123
1.45	0.944656	0.00838169	0.0302537
1.55	0.956549	0.00977901	0.0306316
1.65	1.01936	0.0119173	0.0326474
1.75	1.03431	0.0136698	0.0331297
1.85	1.06941	0.0161045	0.0342563
1.95	1.06576	0.0181514	0.0341397
2.05	1.08858	0.0208069	0.034868
2.15	1.05569	0.022532	0.0338171
2.25	1.18573	0.0289691	0.0379817
2.35	1.14876	0.0313056	0.0368068
2.45	1.14733	0.035121	0.0367679
2.55	1.26057	0.0439884	0.0403998
2.65	1.18449	0.0446668	0.0379585
2.75	1.20635	0.0502991	0.0386644
2.85	1.22712	0.0576004	0.0393515
2.95	1.36247	0.0737254	0.0436714
3.09611	1.20458	0.0496658	0.0386218
3.30182	1.2944	0.0687066	0.0415514
3.49466	1.29622	0.0819324	0.0416482
3.67337	1.22407	0.0942704	0.0393156
3.91024	1.25897	0.107873	0.040487
4.12935	1.33511	0.120079	0.0431577
4.4336	1.24318	0.140153	0.0406785
4.69212	1.54188	0.268292	0.0524638
5.16393	1.16467	0.182695	0.0446393
6.50447	1.03671	0.238688	0.0455284

Table A.2: Data points for centrality class B R_{dAu}. There is an additional systematic uncertainty of 12.5% common to all points.

p_T (GeV/c)	R_{dAu}	Statistical Uncertainty	Systematic Uncertainty
0.65	0.757865	0.00218717	0.0242921
0.75	0.775314	0.00261165	0.0248444
0.85	0.813313	0.00320158	0.0260593
0.95	0.827507	0.00380358	0.0265137
1.05	0.846289	0.0045094	0.0271174
1.15	0.891798	0.00551859	0.0285763
1.25	0.92148	0.00657016	0.0295244
1.35	0.957832	0.00785222	0.0306869
1.45	0.953331	0.00889997	0.0305559
1.55	0.954326	0.0102582	0.0305821
1.65	1.01784	0.0124988	0.032619
1.75	1.01711	0.0141389	0.0325975
1.85	1.0475	0.0165829	0.033569
1.95	1.05862	0.0189227	0.0339215
2.05	1.05739	0.021238	0.0338842
2.15	1.05343	0.0235809	0.0337528
2.25	1.14073	0.0292598	0.0365665
2.35	1.10928	0.0317337	0.0355623
2.45	1.13094	0.0362587	0.0362605
2.55	1.25901	0.0458352	0.0403522
2.65	1.11398	0.0441954	0.0357447
2.75	1.1418	0.0500071	0.0366344
2.85	1.19736	0.0588099	0.0383934
2.95	1.35446	0.0762049	0.043527
3.09554	1.09386	0.0476103	0.0351668
3.30154	1.26293	0.0700265	0.0406127
3.49405	1.19498	0.079478	0.0384715
3.67584	1.22485	0.0979362	0.0396455
3.91136	1.15569	0.104542	0.0374444
4.12402	1.14964	0.109413	0.037508
4.4463	1.18371	0.139696	0.0397329
4.72446	1.44563	0.258544	0.051487
5.14382	1.31366	0.209471	0.0485129
6.51665	0.801604	0.192488	0.0490224

Table A.3: Data points for centrality class C R_{dAu}. There is an additional systematic uncertainty of 13.7% common to all points.

p_T (GeV/c)	R_{dAu}	Statistical Uncertainty	Systematic Uncertainty
0.65	0.90652	0.0027465	0.0290472
0.75	0.899076	0.00319242	0.0288031
0.85	0.921403	0.00383402	0.0295134
0.95	0.918282	0.00447057	0.0294155
1.05	0.916958	0.00519141	0.0293723
1.15	0.943234	0.00621678	0.0302156
1.25	0.960901	0.00730602	0.0307826
1.35	0.98535	0.00862158	0.0315637
1.45	0.961047	0.009611	0.0307853
1.55	0.952693	0.0109662	0.0305244
1.65	1.00002	0.0131659	0.0320409
1.75	1.00834	0.0150127	0.0322995
1.85	1.03156	0.0174886	0.0330474
1.95	1.01786	0.0195367	0.0326127
2.05	0.99239	0.021485	0.0318073
2.15	0.987748	0.023844	0.0316517
2.25	1.07205	0.0295483	0.0343778
2.35	1.02891	0.0317332	0.0330078
2.45	1.06829	0.0367468	0.0342519
2.55	1.13183	0.0443732	0.0363299
2.65	1.08928	0.0461531	0.0349484
2.75	1.04238	0.0493055	0.033412
2.85	1.09025	0.0577531	0.0349856
2.95	1.20335	0.0726779	0.0386424
3.09681	0.991565	0.0469027	0.0318771
3.29889	1.26953	0.0744284	0.0408816
3.49475	1.15237	0.0817839	0.0371422
3.67507	1.1289	0.0970964	0.0364347
3.91265	1.09356	0.10657	0.0353978
4.13676	1.04526	0.107758	0.0352454
4.44777	0.900632	0.120369	0.0312485
4.70719	1.64728	0.305501	0.0567277
5.12393	1.32757	0.226164	0.0485361
6.51716	0.998463	0.247838	0.0600149

Table A.4: Data points for centrality class D R_{dAu}. There is an additional systematic uncertainty of 14.6% common to all points.

p_T (GeV/c)	R_{NAu}	Statistical Uncertainty	Systematic Uncertainty
0.65	0.690077	0.0062744	0.0223509
0.75	0.70366	0.00733775	0.0227232
0.85	0.739555	0.00884515	0.0239142
0.95	0.795036	0.010661	0.0256236
1.05	0.82775	0.0125984	0.0267918
1.15	0.878097	0.0152639	0.0282952
1.25	0.912915	0.0180157	0.0296391
1.35	0.977474	0.0216614	0.0316037
1.45	0.973495	0.024478	0.0314392
1.55	0.982233	0.0280114	0.0317161
1.65	1.06433	0.0341369	0.0342374
1.75	1.09496	0.0392091	0.0356245
1.85	1.19045	0.0470944	0.0383261
1.95	1.13673	0.0515978	0.037008
2.05	1.18154	0.0590109	0.0385882
2.15	1.15036	0.0646357	0.0378404
2.25	1.26961	0.0803855	0.0409678
2.35	1.34408	0.0915188	0.0436554
2.45	1.25851	0.0991259	0.0403648
2.55	1.23693	0.113774	0.0399638
2.65	1.1996	0.11828	0.0405794
2.75	1.31967	0.139954	0.0429056
2.85	1.28159	0.156335	0.041523
2.95	1.46915	0.195643	0.0478216
3.11325	1.08139	0.12701	0.0369069
3.30313	1.39721	0.190992	0.0497627
3.49577	1.28712	0.212343	0.0411878
3.68912	1.14843	0.238776	0.0367499
3.88287	1.37501	0.295115	0.0948847
4.12819	1.55848	0.335489	0.0498714

Table A.5: Data points for centrality class A R_{NAu}. There is an additional systematic uncertainty of 13.2% common to all points.

p_T (GeV/c)	R_{NAu}	Statistical Uncertainty	Systematic Uncertainty
0.65	0.711235	0.00396386	0.0253002
0.75	0.717098	0.00459004	0.025495
0.85	0.785053	0.00581208	0.0273604
0.95	0.806451	0.00684636	0.0281962
1.05	0.818686	0.00796431	0.0285968
1.15	0.879786	0.00987447	0.0307616
1.25	0.900725	0.0114367	0.0314362
1.35	0.95919	0.0139786	0.0335319
1.45	0.98275	0.0164079	0.0344796
1.55	1.00405	0.0190178	0.0342215
1.65	1.02855	0.0220976	0.03518
1.75	1.08522	0.0260888	0.0377201
1.85	1.10029	0.0297987	0.0396431
1.95	1.0818	0.03323	0.0392443
2.05	1.18363	0.0411628	0.0423697
2.15	1.05591	0.0404867	0.0359855
2.25	1.24086	0.0537137	0.0472281
2.35	1.13885	0.0560875	0.0437081
2.45	1.23225	0.0671485	0.0441229
2.55	1.22871	0.0766786	0.0442526
2.65	1.1585	0.0789417	0.0405932
2.75	1.27042	0.0944811	0.0548323
2.85	1.28918	0.107453	0.0488687
2.95	1.5275	0.143946	0.0600095
3.1134	1.10029	0.0857292	0.0480984
3.29214	1.34015	0.127356	0.0811089
3.52794	1.15221	0.144367	0.0420236
3.68223	1.06614	0.165277	0.071911
3.89686	1.3133	0.222983	0.0877569
4.13846	1.524	0.259716	0.0697258
4.46032	1.413	0.329939	0.0560953
4.67991	0.932817	0.656844	0.545354
5.29733	0.638146	0.35875	0.302734

Table A.6: Data points for centrality class B R_{NAu}. There is an additional systematic uncertainty of 13.8% common to all points.

p_T (GeV/c)	R_{NAu}	Statistical Uncertainty	Systematic Uncertainty
0.65	0.789258	0.00509132	0.0254604
0.75	0.808637	0.00602416	0.0260523
0.85	0.841868	0.0070968	0.0270995
0.95	0.867761	0.00838764	0.0279323
1.05	0.890861	0.00990076	0.0287154
1.15	0.925131	0.0116925	0.0298043
1.25	0.980847	0.0141994	0.031591
1.35	0.999575	0.01633	0.0322057
1.45	0.972649	0.0178372	0.0315742
1.55	0.986224	0.020458	0.0318143
1.65	1.05211	0.0251232	0.0339306
1.75	1.08776	0.028779	0.0350218
1.85	1.13362	0.0340671	0.0365287
1.95	1.12334	0.0382628	0.0361073
2.05	1.07939	0.0398	0.0352358
2.15	1.1222	0.0483717	0.0361317
2.25	1.22412	0.0574636	0.0393754
2.35	1.12575	0.0604368	0.0366477
2.45	1.17391	0.0684608	0.0377861
2.55	1.20983	0.0822225	0.0390275
2.65	1.15288	0.0858642	0.037513
2.75	1.18701	0.0936187	0.0387685
2.85	1.24505	0.111097	0.0402015
2.95	1.32869	0.128636	0.0431128
3.08675	1.13337	0.0929837	0.0370695
3.29761	1.34279	0.133024	0.0433854
3.48371	1.1811	0.14162	0.0398204
3.67313	1.20799	0.195412	0.040742
3.91639	1.06637	0.179409	0.0391943
4.1449	1.1307	0.183295	0.0374807
4.42664	0.992124	0.264435	0.059821
4.73211	1.28073	0.615085	0.100026
5.13226	0.822125	0.254843	0.0674211
6.48676	0.901841	0.572468	0.266529

Table A.7: Data points for centrality class C R_{NAu}. There is an additional systematic uncertainty of 12.6% common to all points.

p_T (GeV/c)	R_{NAu}	Statistical Uncertainty	Systematic Uncertainty
0.65	0.993096	0.00474917	0.0319289
0.75	0.978725	0.00546248	0.0314561
0.85	1.00051	0.00651338	0.0321327
0.95	1.00121	0.00757297	0.0321559
1.05	0.987088	0.00870146	0.0316996
1.15	1.01288	0.0103469	0.032556
1.25	1.01937	0.012033	0.0327357
1.35	1.05945	0.014254	0.0340469
1.45	1.02558	0.0158703	0.0329384
1.55	1.01827	0.0179921	0.0327252
1.65	1.09211	0.0218384	0.0351275
1.75	1.06432	0.0243412	0.0341731
1.85	1.08768	0.0282715	0.0348975
1.95	1.08951	0.0318868	0.0349922
2.05	1.07779	0.0355128	0.0346353
2.15	1.04625	0.0387974	0.0335923
2.25	1.15999	0.0482268	0.037488
2.35	1.12949	0.0525495	0.0365928
2.45	1.14161	0.0594294	0.0366808
2.55	1.14219	0.0687711	0.0368207
2.65	1.23469	0.0770006	0.0399944
2.75	1.1421	0.081398	0.0368498
2.85	1.12363	0.0913091	0.0362613
2.95	1.27469	0.113985	0.0417487
3.10456	0.961507	0.0731075	0.0315778
3.30347	1.4554	0.122977	0.0493938
3.50047	1.11287	0.12417	0.0366236
3.69285	1.33119	0.165392	0.0450666
3.90724	1.19356	0.180931	0.0406663
4.15145	0.992056	0.162976	0.0438778
4.43869	1.00279	0.22399	0.0382028
4.73043	1.45538	0.427658	0.0969678
5.19893	1.64731	0.399221	0.070623
6.62694	0.622093	0.326998	0.194354

Table A.8: Data points for centrality class D R_{NAu}. There is an additional systematic uncertainty of 14.7% common to all points.

ν	$R_{dAU(NAu)}$	Statistical Uncertainty	Systematic Uncertainty
		$0.6 < p_T\,(GeV/c) < 1.0$	
1.1 ± 0.2	(0.991704)	0.00290058	0.10099
1.2 ± 0.2	0.909016	0.00169333	0.0911105
3.0 ± 0.3	0.782335	0.00138365	0.0674398
3.6 ± 0.3	(0.816148)	0.00315908	0.0548297
4.6 ± 0.4	0.724557	0.00121455	0.0481108
6.0 ± 0.6	(0.738973)	0.00248416	0.065042
6.5 ± 0.5	0.681691	0.00109879	0.0490676
8.6 ± 0.7	(0.717659)	0.00390571	0.0569029
		$1.5 < p_T\,(GeV/c) < 2.7$	
1.1 ± 0.2	(1.07268)	0.00912075	0.109236
1.2 ± 0.2	1.00082	0.00557343	0.100312
3.0 ± 0.3	1.02495	0.00532543	0.0883537
3.6 ± 0.3	(1.07321)	0.0106251	0.0720997
4.6 ± 0.4	1.03591	0.00512579	0.0687847
6.0 ± 0.6	(1.07156)	0.00965344	0.0943148
6.5 ± 0.5	1.0327	0.004956	0.0743332
8.6 ± 0.7	(1.09899)	0.0146478	0.0871382
		$2.8 < p_T\,(GeV/c) < 6.0$	
1.1 ± 0.2	(1.13897)	0.0391805	0.115987
1.2 ± 0.2	1.10007	0.024594	0.11026
3.0 ± 0.3	1.19437	0.024746	0.102959
3.6 ± 0.3	(1.19227)	0.0455088	0.0800978
4.6 ± 0.4	1.26027	0.0248901	0.0836824
6.0 ± 0.6	(1.23281)	0.0460587	0.108508
6.5 ± 0.5	1.25132	0.0240694	0.0900693
8.6 ± 0.7	(1.27176)	0.0664988	0.100837

Table A.9: Data points for integrated $R_{dAu(NAu)}$. There is an additional systematic uncertainty of 14.6% common to each point.

p_T (GeV/c)	$(h^+ + h^-)/2\pi^0$	Statistical Uncertainty	Systematic Uncertainty
1.25	1.45322	0.0976831	0.16279
1.75	1.64067	0.0616297	0.179157
2.25	1.75699	0.0413156	0.193129
2.75	1.80799	0.0435521	0.200938
3.25	1.80266	0.0580116	0.202911
3.75	1.67161	0.0788047	0.190632
4.25	1.79364	0.119271	0.207408
4.75	1.73311	0.138628	0.20742
5.25	2.07934	0.101555	0.253502
5.75	1.55255	0.109502	0.193319
6.25	1.68938	0.145216	0.217109
6.75	2.35973	0.229768	0.306141
7.25	1.77949	0.222055	0.26465

Table A.10: Data points for $(h^+ + h^-)/2\pi^0$ in centrality class A.

p_T (GeV/c)	$(h^+ + h^-)/2\pi^0$	Statistical Uncertainty	Systematic Uncertainty
1.25	1.49892	0.0950589	0.168151
1.75	1.67999	0.0586074	0.183671
2.25	1.77192	0.0442798	0.195019
2.75	1.83024	0.0496416	0.203707
3.25	1.72831	0.0680347	0.194789
3.75	1.8098	0.101957	0.206607
4.25	1.86891	0.150207	0.216271
4.75	1.58644	0.158304	0.189871
5.25	1.88043	0.113126	0.229367
5.75	1.28844	0.113476	0.163571
6.25	1.95997	0.192921	0.250643
6.75	2.42223	0.293823	0.311582
7.25	1.74917	0.262398	0.257553

Table A.11: Data points for $(h^+ + h^-)/2\pi^0$ in centrality class B.

p_T (GeV/c)	$(h^+ + h^-)/2\pi^0$	Statistical Uncertainty	Systematic Uncertainty
1.25	1.47774	0.0840766	0.165673
1.75	1.63555	0.0564026	0.178754
2.25	1.70005	0.0429918	0.187029
2.75	1.78299	0.056437	0.198385
3.25	1.6983	0.077905	0.191296
3.75	1.70386	0.113537	0.194491
4.25	1.69165	0.16835	0.195768
4.75	1.41885	0.171676	0.172272
5.25	1.87851	0.141064	0.229605
5.75	1.82016	0.179272	0.227912
6.25	1.52541	0.20042	0.204123
6.75	1.75867	0.279548	0.239757
7.25	2.05016	0.416361	0.4378

Table A.12: Data points for $(h^+ + h^-)/2\pi^0$ in centrality class C.

p_T (GeV/c)	$(h^+ + h^-)/2\pi^0$	Statistical Uncertainty	Systematic Uncertainty
1.25	1.40481	0.0826886	0.15748
1.75	1.52346	0.0499559	0.16646
2.25	1.54515	0.0402371	0.170032
2.75	1.58059	0.0604469	0.175834
3.25	1.63914	0.0933405	0.184682
3.75	1.7479	0.136658	0.201385
4.25	1.23219	0.152686	0.144969
4.75	1.47071	0.245851	0.177009
5.25	2.16488	0.188918	0.263862
5.75	1.8278	0.213695	0.22946
6.25	1.843	0.284782	0.242002
6.75	2.21163	0.426547	0.30441
7.25	1.51947	0.457471	0.242549

Table A.13: Data points for $(h^+ + h^-)/2\pi^0$ in centrality class D.

Appendix B

Run 8 Data Tables

Event Class	p_{T} [GeV/c]	R_{dAu}	Δstat.	Δsys.
South 00-20%	0.75-1.00	1.69	<0.01	0.62
	1.00-2.00	1.09	<0.01	0.28
South 20-40%	0.75-1.00	1.49	<0.01	0.33
	1.00-2.00	0.90	<0.01	0.22
South 40-60%	0.75-1.00	1.21	<0.01	0.20
	1.00-2.00	1.07	<0.01	0.20
South 60-88%	0.75-1.00	0.93	<0.01	0.14
	1.00-2.00	0.95	<0.01	0.16
North 00-20%	0.75-1.00	0.20	<0.01	0.03
	1.00-2.00	0.29	<0.01	0.05
North 20-40%	0.75-1.00	0.35	<0.01	0.05
	1.00-2.00	0.46	<0.01	0.08
North 40-60%	0.75-1.00	0.46	<0.01	0.07
	1.00-2.00	0.56	<0.01	0.09
North 60-88%	0.75-1.00	0.74	<0.01	0.07
	1.00-2.00	0.86	<0.01	0.14

Table B.1: R_{dAu} for π^0s in the forward and backward MPCs. There is an additional global scale uncertainty of 12%.

Event Class	$h^{\pm}$ p_{T} [GeV/c]	J_{dAu}	Δstat.	$\Delta\pi^0$ yield	ΔCF	Δ b_0	Δ sys. total
South 00-20%	0.5-1.0	0.70	0.10	0.26	0.12	0.04	0.29
	1.0-2.0	1.01	0.15	0.37	0.16	0.06	0.41
	2.0-4.0	0.77	0.23	0.28	0.27	0.05	0.40
South 20-40%	0.5-1.0	0.50	0.06	0.11	0.17	0.03	0.21
	1.0-2.0	0.86	0.13	0.19	0.23	0.05	0.30
	2.0-4.0	1.57	0.42	0.35	0.15	0.09	0.39
South 40-60%	0.5-1.0	0.79	0.10	0.13	0.17	0.05	0.22
	1.0-2.0	1.20	0.21	0.20	0.15	0.07	0.26
	2.0-4.0	0.94	0.24	0.15	0.06	0.06	0.17
South 60-88%	0.5-1.0	0.56	0.09	0.09	0.04	0.03	0.10
	1.0-2.0	0.92	0.18	0.14	0.15	0.06	0.21
	2.0-4.0	0.74	0.24	0.11	0.12	0.04	0.17
North 00-20%	0.5-1.0	0.26	0.04	0.04	0.09	0.02	0.10
	1.0-2.0	0.34	0.06	0.05	0.12	0.02	0.14
	2.0-4.0	0.41	0.18	0.06	0.14	0.02	0.16
North 20-40%	0.5-1.0	0.36	0.05	0.05	0.07	0.02	0.09
	1.0-2.0	0.56	0.10	0.08	0.10	0.03	0.13
	2.0-4.0	0.66	0.17	0.10	0.12	0.04	0.16
North 40-60%	0.5-1.0	0.46	0.08	0.07	0.11	0.03	0.14
	1.0-2.0	0.55	0.09	0.09	0.11	0.03	0.15
	2.0-4.0	0.64	0.22	0.10	0.06	0.04	0.13
North 60-88%	0.5-1.0	0.63	0.09	0.09	0.07	0.04	0.12
	1.0-2.0	0.68	0.11	0.10	0.09	0.04	0.14
	2.0-4.0	1.21	0.39	0.18	0.12	0.07	0.23

Table B.2: J_{dAu} for π^0s with $0.75<p_{\mathrm{T}}<1.0$ GeV/c in the forward and backward MPCs and charged hadrons in the central arms. $\Delta\pi^0$ yield refers to uncertainty from the π^0 yield needed to normalize J_{dAu}, i.e. R_{dAu} uncertainty. Δ b_0 refers to the uncertainty on the uncorrelated background level in the correlation function; it is the same (6%) for all J_{dAu} with π^0s with $0.75<p_{\mathrm{T}}<1.0$ GeV/c. ΔCF refers to uncertainty in extracting the correlated yield other than the b_0 uncertainty. There is an additional global scale uncertainty of 12%.

Event Class	$h^{\pm}$ p_{T} [GeV/c]	J_{dAu}	Δstat.	$\Delta\pi^0$ yield	ΔCF	Δ b_0	Δ sys. total
South 00-20%	0.5-1.0	1.28	0.14	0.33	0.26	0.32	0.53
	1.0-2.0	1.35	0.17	0.35	0.21	0.34	0.53
	2.0-4.0	1.22	0.86	0.32	0.15	0.31	0.46
South 20-40%	0.5-1.0	0.74	0.08	0.18	0.11	0.19	0.28
	1.0-2.0	1.02	0.13	0.25	0.09	0.26	0.37
	2.0-4.0	0.60	0.41	0.14	0.13	0.15	0.25
South 40-60%	0.5-1.0	0.97	0.11	0.18	0.11	0.24	0.32
	1.0-2.0	1.45	0.19	0.27	0.12	0.36	0.47
	2.0-4.0	0.57	0.39	0.11	0.12	0.14	0.22
South 60-88%	0.5-1.0	0.67	0.09	0.11	0.07	0.17	0.21
	1.0-2.0	0.85	0.14	0.14	0.11	0.21	0.28
	2.0-4.0	0.48	0.34	0.08	0.06	0.12	0.16
North 00-20%	0.5-1.0	0.48	0.06	0.08	0.11	0.12	0.18
	1.0-2.0	0.56	0.07	0.10	0.13	0.14	0.21
	2.0-4.0	0.45	0.33	0.08	0.10	0.11	0.17
North 20-40%	0.5-1.0	0.64	0.08	0.11	0.12	0.16	0.23
	1.0-2.0	0.81	0.11	0.14	0.15	0.20	0.29
	2.0-4.0	0.48	0.33	0.08	0.11	0.12	0.18
North 40-60%	0.5-1.0	0.72	0.10	0.12	0.11	0.18	0.25
	1.0-2.0	0.98	0.12	0.17	0.12	0.25	0.32
	2.0-4.0	0.61	0.43	0.10	0.07	0.15	0.20
North 60-88%	0.5-1.0	0.91	0.10	0.15	0.08	0.23	0.28
	1.0-2.0	0.77	0.10	0.13	0.09	0.19	0.25
	2.0-4.0	0.82	0.56	0.13	0.03	0.20	0.25

Table B.3: J_{dAu} for π^0s with $1.0<p_{\mathrm{T}}<2.0$ GeV/c in the forward and backward MPCs and charged hadrons in the central arms. $\Delta\pi^0$ yield refers to uncertainty from the π^0 yield needed to normalize J_{dAu}, i.e. R_{dAu} uncertainty. Δ b_0 refers to the uncertainty on the uncorrelated background level in the correlation function; it is the same (25%) for all J_{dAu} with π^0s with $1.0<p_{\mathrm{T}}<2.0$ GeV/c. ΔCF refers to uncertainty in extracting the correlated yield other than the b_0 uncertainty. There is an additional global scale uncertainty of 12%.

Event Class	h$^{\pm}$ p_{T} [GeV/c]	I_{dAu}	Δstat.	ΔCF	Δ b$_0$	Δ sys. total
South 00-20%	0.5-1.0	0.41	0.06	0.07	0.02	0.08
	1.0-2.0	0.60	0.09	0.09	0.04	0.10
	2.0-4.0	0.46	0.13	0.16	0.03	0.16
South 20-40%	0.5-1.0	0.34	0.04	0.11	0.02	0.12
	1.0-2.0	0.58	0.09	0.15	0.03	0.16
	2.0-4.0	1.05	0.28	0.10	0.06	0.12
South 40-60%	0.5-1.0	0.65	0.08	0.14	0.04	0.15
	1.0-2.0	0.99	0.17	0.12	0.06	0.14
	2.0-4.0	0.77	0.20	0.05	0.05	0.07
South 60-88%	0.5-1.0	0.61	0.10	0.04	0.04	0.06
	1.0-2.0	0.99	0.20	0.16	0.06	0.17
	2.0-4.0	0.80	0.26	0.13	0.05	0.14
North 00-20%	0.5-1.0	1.30	0.20	0.16	0.08	0.18
	1.0-2.0	1.73	0.28	0.24	0.10	0.26
	2.0-4.0	2.08	0.91	0.23	0.12	0.26
North 20-40%	0.5-1.0	1.03	0.15	0.08	0.06	0.10
	1.0-2.0	1.59	0.30	0.09	0.10	0.13
	2.0-4.0	1.89	0.49	0.10	0.11	0.15
North 40-60%	0.5-1.0	1.01	0.17	0.24	0.06	0.25
	1.0-2.0	1.20	0.20	0.24	0.07	0.25
	2.0-4.0	1.41	0.48	0.12	0.08	0.15
North 60-88%	0.5-1.0	0.85	0.12	0.09	0.05	0.10
	1.0-2.0	0.91	0.15	0.12	0.05	0.13
	2.0-4.0	1.63	0.52	0.15	0.10	0.18

Table B.4: I_{dAu} for π^0s with $0.75<p_{\mathrm{T}}<1.0$ GeV/c in the forward and backward MPCs and charged hadrons in the central arms. Δ b$_0$ refers to the uncertainty on the uncorrelated background level in the correlation function; it is the same (6%)for all I_{dAu} with π^0s with $0.75<p_{\mathrm{T}}<1.0$ GeV/c. ΔCF refers to uncertainty in extracting the correlated yield other than the b$_0$ uncertainty.

Event Class	$h^{\pm}$ p_T [GeV/c]	I_{dAu}	Δstat.	ΔCF	Δ b_0	Δ sys. total
South 00-20%	0.5-1.0	1.18	0.13	0.24	0.29	0.38
	1.0-2.0	1.25	0.16	0.20	0.31	0.37
	2.0-4.0	1.13	0.79	0.13	0.28	0.31
South 20-40%	0.5-1.0	0.83	0.09	0.13	0.21	0.24
	1.0-2.0	1.14	0.15	0.10	0.28	0.30
	2.0-4.0	0.66	0.45	0.15	0.17	0.22
South 40-60%	0.5-1.0	0.91	0.10	0.10	0.23	0.25
	1.0-2.0	1.36	0.17	0.11	0.34	0.36
	2.0-4.0	0.54	0.37	0.12	0.13	0.18
South 60-88%	0.5-1.0	0.70	0.09	0.08	0.18	0.19
	1.0-2.0	0.89	0.15	0.12	0.22	0.25
	2.0-4.0	0.51	0.35	0.07	0.13	0.14
North 00-20%	0.5-1.0	1.67	0.21	0.19	0.42	0.46
	1.0-2.0	1.96	0.26	0.23	0.49	0.54
	2.0-4.0	1.58	1.14	0.14	0.40	0.42
North 20-40%	0.5-1.0	1.38	0.17	0.08	0.34	0.35
	1.0-2.0	1.76	0.25	0.07	0.44	0.45
	2.0-4.0	1.05	0.71	0.15	0.26	0.30
North 40-60%	0.5-1.0	1.30	0.18	0.17	0.32	0.37
	1.0-2.0	1.76	0.22	0.15	0.44	0.47
	2.0-4.0	1.10	0.78	0.09	0.28	0.29
North 60-88%	0.5-1.0	1.06	0.12	0.08	0.26	0.28
	1.0-2.0	0.89	0.11	0.11	0.22	0.25
	2.0-4.0	0.96	0.65	0.03	0.24	0.24

Table B.5: I_{dAu} for π^0s with $1.0<p_T<2.0$ GeV/c in the forward and backward MPCs and charged hadrons in the central arms. Δ b_0 refers to the uncertainty on the uncorrelated background level in the correlation function; it is the same (25%)for all I_{dAu} with π^0s with $1.0<p_T<2.0$ GeV/c. ΔCF refers to uncertainty in extracting the correlated yield other than the b_0 uncertainty.

Bibliography

[1] E. V. Shuryak. "Quantum chromodynamics and the theory of superdense matter." Physics Reports **61**, 71 (1980). ISSN 0370-1573.

[2] I. Arsene *et al.* "Quark-gluon plasma and color glass condensate at RHIC? The perspective from the BRAHMS experiment." Nuclear Physics A **757**, 1 (2005). ISSN 0375-9474. First Three Years of Operation of RHIC.

[3] B. Back *et al.* "The PHOBOS perspective on discoveries at RHIC." Nuclear Physics A **757**, 28 (2005). ISSN 0375-9474. First Three Years of Operation of RHIC.

[4] J. Adams *et al.* "Experimental and theoretical challenges in the search for the quark-gluon plasma: The STAR Collaboration's critical assessment of the evidence from RHIC collisions." Nuclear Physics A **757**, 102 (2005). ISSN 0375-9474. First Three Years of Operation of RHIC.

[5] K. Adcox *et al.* "Formation of dense partonic matter in relativistic nucleus-nucleus collisions at RHIC: Experimental evaluation by the PHENIX Collaboration." Nuclear Physics A **757**, 184 (2005). ISSN 0375-9474. First Three Years of Operation of RHIC.

[6] M. Gell-Mann. "The Eightfold Way: A Theory of strong interaction symmetry." CTSL-20.

[7] D. J. Gross and F. Wilczek. "Ultraviolet Behavior of Non-Abelian Gauge Theories." Phys. Rev. Lett. **30**, 1343 (1973).

[8] H. D. Politzer. "Reliable Perturbative Results for Strong Interactions?" Phys. Rev. Lett. **30**, 1346 (1973).

[9] M. E. Peskin and D. V. Schroeder. *An Introduction to quantum field theory.* Reading, USA: Addison-Wesley (1995) 842 p.

[10] S. Bethke. "Experimental tests of asymptotic freedom." Progress in Particle and Nuclear Physics **58**, 351 (2007). ISSN 0146-6410.

[11] K. G. Wilson. "Confinement of quarks." Phys. Rev. D **10**, 2445 (1974).

[12] J. C. Collins and M. J. Perry. "Superdense Matter: Neutrons or Asymptotically Free Quarks?" Phys. Rev. Lett. **34**, 1353 (1975).

[13] F. Karsch. "Lattice QCD at High Temperature and Density." In W. Plessas and L. Mathelitsch, editors, *Lectures on Quark Matter*, volume 583 of *Lecture Notes in Physics*, pages 209–249. Springer Berlin / Heidelberg (2002).

[14] S. S. Adler *et al.* "High- p_T charged hadron suppression in $Au + Au$ collisions at $\sqrt{s_{NN}} = 200GeV$." Phys. Rev. C **69**, 034910 (2004).

[15] E. D. Bloom *et al.* "High-Energy Inelastic $e-p$ Scattering at 6° and 10°." Phys. Rev. Lett. **23**, 930 (1969).

[16] M. Breidenbach *et al.* "Observed Behavior of Highly Inelastic Electron-Proton Scattering." Phys. Rev. Lett. **23**, 935 (1969).

[17] K. Nakamura *et al.* "Review of particle physics." J. Phys. **G37**, 075021 (2010).

[18] J. J. Aubert *et al.* "The ratio of the nucleon structure functions F2N for iron and deuterium." Physics Letters B **123**, 275 (1983). ISSN 0370-2693.

[19] D. GEESAMAN, K. SAITO, and A. THOMAS. "THE NUCLEAR EMC EFFECT." ANNUAL REVIEW OF NUCLEAR AND PARTICLE SCIENCE **45**, 337 (1995). ISSN 0163-8998.

[20] J. Seely *et al.* "New Measurements of the European Muon Collaboration Effect in Very Light Nuclei." Phys. Rev. Lett. **103**, 202301 (2009).

[21] L. B. Weinstein *et al.* "Short Range Correlations and the EMC Effect." Phys. Rev. Lett. **106**, 052301 (2011).

[22] N. Armesto. "Nuclear shadowing." J. Phys. **G32**, R367 (2006).

[23] J. W. Cronin *et al.* "Production of hadrons at large transverse momentum at 200, 300, and 400 GeV." Phys. Rev. D **11**, 3105 (1975).

[24] N. Nicolaev and V. Zakharov. "Parton model and deep inelastic scattering on nuclei." Physics Letters B **55**, 397 (1975). ISSN 0370-2693.

[25] B. Kopeliovich, A. Schäfer, and A. Tarasov. “Nonperturbative effects in gluon radiation and photoproduction of quark pairs.” Phys. Rev. D **62**, 054022 (2000).

[26] N. Armesto. “A simple model for nuclear structure functions at small x in the dipole picture.” The European Physical Journal C - Particles and Fields **26**, 35 (2002). ISSN 1434-6044. 10.1007/s10052-002-1021-z.

[27] Y. L. Dokshitzer. “Calculation of the Structure Functions for Deep Inelastic Scattering and e+ e- Annihilation by Perturbation Theory in Quantum Chromodynamics.” Sov. Phys. JETP **46**, 641 (1977).

[28] V. N. Gribov and L. N. Lipatov. “Deep inelastic e p scattering in perturbation theory.” Sov. J. Nucl. Phys. **15**, 438 (1972).

[29] G. Altarelli and G. Parisi. “Asymptotic freedom in parton language.” Nuclear Physics B **126**, 298 (1977). ISSN 0550-3213.

[30] I. I. Balitsky and L. N. Lipatov. “The Pomeranchuk Singularity in Quantum Chromodynamics.” Sov. J. Nucl. Phys. **28**, 822 (1978).

[31] E. A. Kuraev, L. N. Lipatov, and V. S. Fadin. “The Pomeranchuk Singularity in Nonabelian Gauge Theories.” Sov. Phys. JETP **45**, 199 (1977).

[32] R. K. Ellis and W. J. Stirling. *QCD and collider physics*. Based on lectures given at CERN School of Physics, Majorca, Spain, Sep 16-29, 1990 and CERN-JINR School of Physics, Egmond, Netherlands, Jun 25 - Jul 8, 1989.

[33] F. Gelis *et al.* “The Color Glass Condensate.” http://arxiv.org/abs/1002.0333v1 (2010).

[34] M. Ciafaloni. “Coherence effects in initial jets at small Q2/s.” Nuclear Physics B **296**, 49 (1988). ISSN 0550-3213.

[35] S. Catani, F. Fiorani, and G. Marchesini. “QCD Coherence in Initial State Radiation.” Phys. Lett. **B234**, 339 (1990).

[36] S. Catani, F. Fiorani, and G. Marchesini. “Small-x behaviour of initial state radiation in perturbative QCD.” Nuclear Physics B **336**, 18 (1990). ISSN 0550-3213.

[37] J. Kwieciński, A. D. Martin, and P. J. Sutton. "Gluon distribution at small x obtained from a unified evolution equation." Phys. Rev. D **52**, 1445 (1995).

[38] F. Aaron *et al.* "Combined measurement and QCD analysis of the inclusive $e^{\pm}p$ scattering cross sections at HERA." Journal of High Energy Physics **2010**, 1 (2010).

[39] L. D. McLerran. "The color glass condensate and small x physics: 4 lectures." Lect. Notes Phys. **583**, 291 (2002).

[40] L. McLerran and R. Venugopalan. "Computing quark and gluon distribution functions for very large nuclei." Phys. Rev. D **49**, 2233 (1994).

[41] L. McLerran and R. Venugopalan. "Gluon distribution functions for very large nuclei at small transverse momentum." Phys. Rev. D **49**, 3352 (1994).

[42] L. McLerran and R. Venugopalan. "Green's function in the color field of a large nucleus." Phys. Rev. D **50**, 2225 (1994).

[43] J. Jalilian-Marian *et al.* "The BFKL equation from the Wilson renormalization group." Nuclear Physics B **504**, 415 (1997). ISSN 0550-3213.

[44] J. Jalilian-Marian *et al.* "Wilson renormalization group for low x physics: Towards the high density regime." Phys. Rev. D **59**, 014014 (1998).

[45] J. Jalilian-Marian, A. Kovner, and H. Weigert. "Wilson renormalization group for low x physics: Gluon evolution at finite parton density." Phys. Rev. D **59**, 014015 (1998).

[46] E. Iancu, A. Leonidov, and L. McLerran. "Nonlinear gluon evolution in the color glass condensate: I." Nuclear Physics A **692**, 583 (2001). ISSN 0375-9474.

[47] E. Ferreiro *et al.* "Nonlinear gluon evolution in the color glass condensate: II." Nuclear Physics A **703**, 489 (2002). ISSN 0375-9474.

[48] S. S. Adler *et al.* "Nuclear Modification Factors for Hadrons at Forward and Backward Rapidities in Deuteron-Gold Collisions at $\sqrt{s_{NN}} = 200\ GeV$." Phys. Rev. Lett. **94**, 082302 (2005).

[49] I. Arsene *et al.* “Evolution of the Nuclear Modification Factors with Rapidity and Centrality in $d + Au$ Collisions at $\sqrt{N^SN} = 200\ GeV$.” Phys. Rev. Lett. **93**, 242303 (2004).

[50] J. Adams *et al.* “Forward Neutral Pion Production in $p + p$ and $d + Au$ Collisions at $\sqrt{s_{NN}} = 200\ GeV$.” Phys. Rev. Lett. **97**, 152302 (2006).

[51] D. Kharzeev, E. Levin, and L. McLerran. “Jet azimuthal correlations and parton saturation in the color glass condensate.” Nuclear Physics A **748**, 627 (2005). ISSN 0375-9474.

[52] J.-W. Qiu and I. Vitev. “Coherent QCD multiple scattering in proton-nucleus collisions.” Physics Letters B **632**, 507 (2006). ISSN 0370-2693.

[53] M. Allen *et al.* “PHENIX inner detectors.” Nuclear Instruments and Methods in Physics Research Section A: Accelerators, Spectrometers, Detectors and Associated Equipment **499**, 549 (2003). ISSN 0168-9002. The Relativistic Heavy Ion Collider Project: RHIC and its Detectors.

[54] C. Adler *et al.* “The RHIC zero-degree calorimeters.” Nuclear Instruments and Methods in Physics Research Section A: Accelerators, Spectrometers, Detectors and Associated Equipment **499**, 433 (2003). ISSN 0168-9002. The Relativistic Heavy Ion Collider Project: RHIC and its Detectors.

[55] T. A. Armstrong *et al.* “The E864 lead-scintillating fiber hadronic calorimeter.” Nuclear Instruments and Methods in Physics Research Section A: Accelerators, Spectrometers, Detectors and Associated Equipment **406**, 227 (1998). ISSN 0168-9002.

[56] K. Adcox *et al.* “PHENIX central arm tracking detectors.” Nuclear Instruments and Methods in Physics Research Section A: Accelerators, Spectrometers, Detectors and Associated Equipment **499**, 489 (2003). ISSN 0168-9002. The Relativistic Heavy Ion Collider Project: RHIC and its Detectors.

[57] S. Johnson *et al.* “Three-Dimensional Track Finding in the PHENIX Drift Chamber by a Combinatorial Hough Transform Method.” International Conference on Computing in High Energy Physics (CHEP ’98), Chicago, USA, 1998. (1998).

[58] M. Aizawa *et al.* “PHENIX central arm particle ID detectors.” Nuclear Instruments and Methods in Physics Research Section A: Accelerators, Spectrometers, Detectors and Associated Equipment **499**, 508 (2003).

ISSN 0168-9002. The Relativistic Heavy Ion Collider Project: RHIC and its Detectors.

[59] S. S. Adler *et al.* “Azimuthal Angle Correlations for Rapidity Separated Hadron Pairs in $d + Au$ Collisions at $\sqrt{s_{NN}} = 200\ GeV$.” Phys. Rev. Lett. **96**, 222301 (2006).

[60] M. Ippolitov *et al.* “Studies of lead tungstate crystals for the ALICE electromagnetic calorimeter PHOS.” Nuclear Instruments and Methods in Physics Research Section A: Accelerators, Spectrometers, Detectors and Associated Equipment **486**, 121 (2002). ISSN 0168-9002.

[61] G. David *et al.* “Pattern recognition in the PHENIX PbSc electromagnetic calorimeter.” Nuclear Science, IEEE Transactions on **47**, 1982 (2000). ISSN 0018-9499.

[62] B. Meredith *et al.* “MPC Clustering: Description, Performance, and Comparison of Run8 p+p Data and Simulation.” PHENIX Analysis Note **949**.

[63] S. S. Adler *et al.* “Centrality dependence of charged hadron production in deuteron+gold and nucleon+gold collisions at $\sqrt{s_{NN}} = 200$ GeV.” Phys. Rev. C **77**, 014905 (2008).

[64] K. Adcox *et al.* “Suppression of Hadrons with Large Transverse Momentum in Central $Au + Au$ Collisions at $\sqrt{s_{NN}} = 130 GeV$.” Phys. Rev. Lett. **88**, 022301 (2001).

[65] S. S. Adler *et al.* “Suppressed π^0 Production at Large Transverse Momentum in Central $Au+Au$ Collisions at $\sqrt{s_{NN}} = 200\ GeV$.” Phys. Rev. Lett. **91**, 072301 (2003).

[66] L. Hulthén and M. Sagawara. Handbuch der Physik **39** (1957).

[67] S. N. White. “Diffraction Dissociation — 50 Years later.” AIP Conference Proceedings **792**, 527 (2005).

[68] S.Belikov *et al.* “Determination of the Absolute Luminosity for the Proton-Proton Data at sqrts=200 GeV Recorded by PHENIX during RHIC Run-02.” PHENIX Analysis Note **184**.

[69] S. S. Adler *et al.* “Nuclear effects on hadron production in $d+Au$ collisions at $\sqrt{s_{NN}} = 200$ GeV revealed by comparison with $p+p$ data.” Phys. Rev. C **74**, 024904 (2006).

[70] J. Jia. *High-pT Charged Hadron Suppression in Au-Au Collisions at* $\sqrt{s_{NN}} = 200\ GeV$*.* Ph.D. thesis, Stony Brook University (2003).

[71] K. Okada. "Inclusive Charged Hadron cross section Measurement in Run2 pp." PHENIX Analysis Note **355**.

[72] J. Adams *et al.* "Identified hadron spectra at large transverse momentum in p+p and d+Au collisions at." Physics Letters B **637**, 161 (2006). ISSN 0370-2693.

[73] S. S. Adler *et al.* "Absence of Suppression in Particle Production at Large Transverse Momentum in $\sqrt{s_{NN}} = 200\ GeV\ \ d + Au$ Collisions." Phys. Rev. Lett. **91**, 072303 (2003).

[74] V.Riabov, Y. Riabov, and A.Milov. "Hadron decays of light mesons in Run3 p+p and d+Au." PHENIX Analysis Note **421**.

[75] S. S. Adler *et al.* "Identified charged particle spectra and yields in $Au{+}Au$ collisions at $\sqrt{s_{NN}} = 200GeV$." Phys. Rev. C **69**, 034909 (2004).

[76] S. S. Adler *et al.* "Measurement of Transverse Single-Spin Asymmetries for Midrapidity Production of Neutral Pions and Charged Hadrons in Polarized $p + p$ Collisions at $\sqrt{s} = 200\ GeV$." Phys. Rev. Lett. **95**, 202001 (2005).

[77] P. B. Straub *et al.* "Nuclear dependence of high-x_t hadron and high-τ hadron-pair production in p-A interactions at $\sqrt{s}$ =38.8 GeV." Phys. Rev. Lett. **68**, 452 (1992).

[78] Y. Zhang *et al.* "High-p_T pion and kaon production in relativistic nuclear collisions." Phys. Rev. C **65**, 034903 (2002).

[79] X.-N. Wang. "Systematic study of high p_T hadron spectra in pp, pA, and AA collisions at ultrarelativistic energies." Phys. Rev. C **61**, 064910 (2000).

[80] B. Z. Kopeliovich *et al.* "Cronin Effect in Hadron Production Off Nuclei." Phys. Rev. Lett. **88**, 232303 (2002).

[81] I. Vitev and M. Gyulassy. "High-p_T Tomography of $d + Au$ and $Au + Au$ at SPS, RHIC, and LHC." Phys. Rev. Lett. **89**, 252301 (2002).

[82] S. S. Adler *et al.* “Centrality Dependence of π^0 and η Production at Large Transverse Momentum in $\sqrt{s_{NN}} = 200\ GeV\ \ d + Au$ Collisions.” Phys. Rev. Lett. **98**, 172302 (2007).

[83] B. Alper *et al.* “Production spectra of [pi]±, K±, p± at large angles in proton-proton collisions in the CERN intersecting storage rings.” Nuclear Physics B **100**, 237 (1975). ISSN 0550-3213.

[84] A. F. Krutov and V. E. Troitsky. “Parametrization of the deuteron wave function obtained within a dispersion approach.” Phys. Rev. C **76**, 017001 (2007).

[85] K. Reygers. “A New Parameterization of the Deuteron Wavefunction for PHENIX Glauber calculations.” PHENIX Analysis Note **633**.

[86] K. Boyle *et al.* “Results on invariant cross section and double helicity asymmetry (A_{LL}) in π^0 production in polarized proton-proton collision at $\sqrt{s} = 200$ GeV from Run5.” PHENIX Analysis Note **567**.

[87] T. Sjostrand, S. Mrenna, and P. Z. Skands. “PYTHIA 6.4 Physics and Manual.” JHEP **05**, 026 (2006).

[88] S. S. Adler *et al.* “Detailed study of high-p_T neutral pion suppression and azimuthal anisotropy in $Au + Au$ collisions at $\sqrt{s_{NN}} = 200$ GeV.” Phys. Rev. C **76**, 034904 (2007).

[89] A. Sickles, M. P. McCumber, and A. Adare. “Extraction of Correlated Jet Pair Signals in Relativistic Heavy Ion Collisions.” Phys. Rev. **C81**, 014908 (2010).

[90] L. Frankfurt and M. Strikman. “Energy losses in the black disc regime and correlation effects in the STAR forward pion production in dAu collisions.” Physics Letters B **645**, 412 (2007). ISSN 0370-2693.

[91] B. Meredith. “Signatures of color glass condensate: Forward azimuthal angle di-hadron correlations in PHENIX.” Nuclear Physics A **854**, 175 (2011). ISSN 0375-9474. Saturation, the Color Glass Condensate and the Glasma: What Have We Learned from RHIC?

[92] E. Braidot. “Suppression of Forward Pion Correlations in d+Au Interactions at STAR.” (2010).

[93] C. Marquet. “Forward inclusive dijet production and azimuthal correlations in pA collisions.” Nuclear Physics A **796**, 41 (2007). ISSN 0375-9474.

[94] K. Tuchin. “Rapidity and centrality dependence of azimuthal correlations in Deuteron-Gold collisions at RHIC.” Nucl. Phys. **A846**, 83 (2010).

[95] A. Deshpande *et al.* “STUDY OF THE FUNDAMENTAL STRUCTURE OF MATTER WITH AN ELECTRON-ION COLLIDER.” Annual Review of Nuclear and Particle Science **55**, 165 (2005).